UC Santa Barbara
UC Santa Barbara Electronic Theses and Dissertations

Title
Geometric Simplification of Optimization Problems in Millimeter-Wave Sensing

Permalink
https://escholarship.org/uc/item/9x60r203

Author
Gupta, Anant

Publication Date
2020

Peer reviewed|Thesis/dissertation

University of California
Santa Barbara

Geometric Simplification of Optimization Problems in Millimeter-Wave Sensing

A dissertation submitted in partial satisfaction
of the requirements for the degree

Doctor of Philosophy
in
Electrical and Computer Engineering

by

Anant Gupta

Committee in charge:

Professor Upamanyu Madhow, Chair
Professor Kenneth Rose
Professor Ramtin Pedarsani
Professor Amin Arbabian

March 2020

The Dissertation of Anant Gupta is approved.

_____

Professor Kenneth Rose

_____

Professor Ramtin Pedarsani

_____

Professor Amin Arbabian

_____

Professor Upamanyu Madhow, Committee Chair

March 2020

Geometric Simplification of Optimization Problems in Millimeter-Wave Sensing

Acknowledgements

Curriculum Vitæ
Anant Gupta

Education

2020	Ph.D. in ECE (Expected), University of California, Santa Barbara.
2016	M.S. in ECE, University of California, Santa Barbara.
2013	BTech+MTech in ECE, IIT Kharagpur, India

Publications

(J2) **A. Gupta**, A. D. Sezer and U. Madhow, "Multi-sensor Spatial Association using Joint Range-Doppler Features", IEEE Transactions on Signal Processing (to be submitted shortly)

(J1) **A. Gupta**, U. Madhow, A. Arbabian and A. Sadri, "Design of Large Effective Apertures for Millimeter Wave Systems using a Sparse Array of Subarrays", IEEE Transactions on Signal Processing, 2019.

(C2) **A. Gupta**, U. Madhow, A. Arbabian and A. Sadri, "On beam design for sparse arrays of subarrays using multi-objective optimization and estimation-theoretic criteria", 51st Asilomar Conference on Signals, Systems and Computers, 2017, Pacifc Grove, USA.

(C1) **A. Gupta**, U. Madhow, and A. Arbabian, "Super-resolution in position and velocity estimation for short-range mm wave radar", 50th Asilomar Conference on Signals, Systems and Computers, 2016, Pacific Grove, USA.

Abstract

Geometric Simplification of Optimization Problems in Millimeter-Wave Sensing

by

Anant Gupta

Recent advances in low-cost design and fabrication enable the potential application of high-accuracy millimeter wave (mmWave) radar sensors to a variety of commercial sectors, including automotive, drones and robotics [1]. The large bandwidth available at mmWave band enable high range resolution, while the small wavelength enhances Doppler resolution. In addition, the small wavelength allows for reduced antenna size that can be used to synthesize large aperture antenna arrays which provide narrow beams for high angular resolution. However, such antennas are expensive in terms of both cost and power consumption. In addition, individual sensors are vulnerable to blockage by larger objects in vicinity of the sensor. Therefore, an array of widely separated radar sensors is used to improve localization accuracy while combating blockage at individual sensors. In this dissertation, we discuss efficient methods for solving the large aperture antenna design and multi-sensor localization problem by exploiting intrinsic geometric properties.

We first consider the problem of designing large effective aperture antenna in 2D for accurate Direction of Arrival estimation. Conventionally, a large effective aperture antenna is constructed by filling the aperture with patch elements spaced at half the carrier wavelength or less. However, such dense array designs do not scale well with increasing aperture area in terms of cost, complexity and power consumption. On the other hand, compact antenna arrays with a moderately large number of elements can be realized at relatively low cost, especially as the carrier frequency increases. We propose a

cost-effective synthesis of large apertures (and hence sharp beams) is via sparse placement of a number of such compact arrays, henceforth termed "subarrays", optimizing the placement (and controlling the phases) so as to reduce unwanted grating lobes. We assess the performance of our designs for the fundamental problem of bearing estimation for one or more sources which provides a useful tradeoff comparison of the beamwidth reduction and increase in sidelobe level.

Although mmWave sensors provide high accuracy measurements, individual sensors are vulnerable to blockage due to the mm-wave propagation characteristics. For safety critical applications a network of sensors is required to avoid detection issues in case some sensors suffer from blockage. We study the fundamental limits on localization accuracy using a network of mm-wave radar sensors. We show that super-resolution algorithms can be used to achieve good localization accuracy using low cost mmWave sensors.

Finally, we examine the spatial association of observations collected from multiple sensors in the single snapshot setting. Since the observations collected at each sensor are unordered, they need to be associated with a common target before they can be combined for location estimation. We consider the general data association problem where sensor observation contain range, Doppler information from a single snapshot only. Without any prior association information, this problem has exponential complexity. However, we show that inherent geometric relations between sensor measurements and their locations can be used to drastically reduce this association complexity. Our proposed association framework provides robustness to detection anomalies caused by blockage and achieves significant computational savings when large number of sensor are used.

Contents

List of Figures

List of Tables

Chapter 1

Introduction

Recent advances in low-cost design and fabrication of radar sensors have enabled the exploration of millimeter(mm)-wave band (wavelength between 1 mm and 10 mm). The FCC has allocated 7 GHz of unlicensed contiguous spectrum in the 60 GHz (V-band) for various emerging sensing and imaging applications [1]. The wide frequency bandwidth provides high resolution observations of the environment which make mm-wave radar sensors appealing for a variety of commercial sectors, including automotive, drones and robotics [2, 3]. In addition, the small wavelength allows for reduced antenna size that can be used to synthesize beamforming arrays of reasonable sizes for autonomous application. Such sensors can measure a variety of target signatures such as range, Doppler, bearing and micro-Doppler. The key goal in all sensing applications is to achieve good localization accuracy of targets in a scene by utilizing these measurements.

Many sensing and situational awareness applications (e.g., radar imaging for vehicles and drones) require highly directional, electronically steerable beams. Reducing beam width requires expansion of antenna aperture. This is typically accomplished by filling the aperture with antenna elements spaced at half the carrier wavelength or less, in order to avoid grating lobes. However, this approach does not scale well with aperture size since

the cost, power consumption and design complexity increases with number of antenna elements. On the other hand, reducing number of elements involves placement beyond half wavelength spacing generates unavoidable grating lobes. An intricate optimization to sparsely distribute array elements can be done to emulates the properties of a large aperture array while controlling grating lobes. We propose a coherent sparse array of subarray architecture motivated by recent progress in low-cost hardware realizations of moderately sized antenna arrays that mitigate these sidelobes arising from sparsity. We obtain sparse array designs using a multi-objective optimization which results in arrays that balance sidelobes for reduced bandwidth..

The mm-wave signals are vulnerable to blockage due to high penetration loss and weaker diffration [4]. Therefore, an extended size object situated close to the sensor can occlude farther objects in the environment. This creates frequent detection anomalies at the sensor which is one of the major concerns for safety critical sensing applications. An array of multiple spatially separated sensors is employed to mitigate the impact of such anomalies at individual sensors.

In the second part of this dissertation, we consider the problem of localizing multiple objects in the environment using a network of mm-wave radar sensors. We first analyze the fundamental limits on range and doppler estimation accuracy and resolution for low-cost monostatic radar sensors using estimation theoretic analysis. We show that super-resolution algorithms can be used to extract these range, doppler at individual sensor with accuracy approaching the estimation theoretic lower bounds. By combining these measurements over multiple widely separated sensors, we can achieve localization accuracy sufficient for short to medium range (less than 20 m) situational awareness applications. However, in multiple target scenario, the measurements obtained at each sensor are un-ordered i.e. the source of the observations is not known to the sensor. Therefore the observations from each sensor in the network need to be associated with a

unique target before fusion of measurements can be performed.

We consider the general spatial association problem where observations collected during a single snapshot of the scene need to be associated across multiple sensors. Each radar sensor is omni-directional and observes only range and doppler of the non-occluded targets. In this general scenario where no prior association information is available, complexity of the association problem grows quickly with increasing number of sensors, objects in the scene. We propose an association framework that exploits geometric relations between range, doppler observations and the sensor geometry to reduce association complexity. Our numerical results show this framework performs well in the presence of detection anomalies at sensors and achieves significant reduction in complexity compared to traditional methods.

We provide a brief overview of the problems considered in this thesis in Sections 1.1, 1.2 and 1.3 and state our contributions.

1.1 Large effective aperture design using array of subarray architecture

Chapter 2 of this thesis investigates the problem of synthesizing narrow beams using a tiled architecture, with a sparse set of subarrays spread over a large physical aperture. Each subarray is a relatively compact antenna array with a moderate number of elements at sub-wavelength spacing. This is a modular design, in which each subarray can be controlled by a radio frequency integrated circuit (RFIC) of moderate complexity, with multiple RFICs tiled to build up large aperture arrays with a much larger number of elements compared to that of a single subarray. The resulting array is "sparse" because, while the total number of antenna elements summed across subarrays is large, this number

is far smaller than that for a classical design with antennas at sub-wavelength spacing spanning the entire physical aperture. The sidelobes and grating lobes resulting from such spatial undersampling must therefore be controlled in order for our proposed "array of subarrays" to be useful. Our goal here is to determine the placement of a given number of subarrays over a physical aperture in order to optimize multiple beam attributes, including beam width, maximum sidelobe level, and directivity.

While our framework is general, the design of millimeter wave arrays is of particular interest to us, because the small carrier wavelength enables synthesis of narrow beams using relatively compact apertures. As a running example throughout chapter 2, we consider the design of a 60 GHz array of subarrays created by placing 8 subarrays over an aperture size of 10 cm by 10 cm ($20\lambda \times 20\lambda$ for wavelength $\lambda = 0.5$ cm), where each subarray has 4×4 elements arranged in uniform rectangular grid with 0.5λ horizontal spacing and 0.6λ vertical spacing. The total number of antenna elements in such designs is 128, which is an order of magnitude smaller than the 1600 elements required to cover the entire aperture at half-wavelength spacing. In addition to optimizing beam characteristics, our design framework also accounts for practical placement constraints consistent with existing prototype subarrays. For example, the subarrays need to be aligned along their axes, assuming that all elements have unidirectional linear polarization. Also, each subarray tile occupies extra physical area on the plane, which must be accounted for in the placement procedure. Figure 1.1 shows an example array of subarray configuration.

1.1.1   Contributions

Our contributions are summarized as follows:

1. We formulate the problem of subarray placement as multi-objective optimization of key performance measures such as beam width (`BW`), maximum sidelobe level
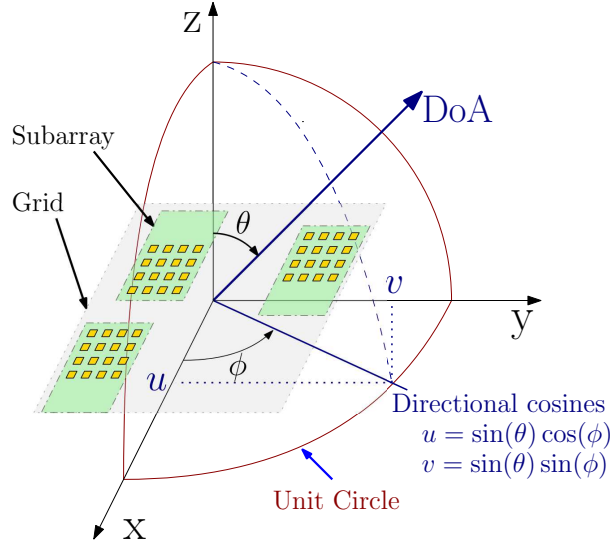
Figure 1.1: 2D Array Geometry and Spherical coordinate system for Direction of Arrival (DoA) estimation.

(MSLL), eccentricity (ecc) and directivity (G_D),

$$\begin{aligned} \text{Minimize} \quad & \text{BW}(\boldsymbol{C}, \boldsymbol{w}), \text{MSLL}(\boldsymbol{C}, \boldsymbol{w}), \text{ecc}(\boldsymbol{C}, \boldsymbol{w}) \\ \text{Maximize} \quad & G_D(\boldsymbol{C}, \boldsymbol{w}) \\ \text{subject to} \quad & \text{AoS}(\boldsymbol{C}) \end{aligned} \tag{1.1}$$

where $\boldsymbol{C}$ is $N_s \times 2$ Subarray center position matrix, $\boldsymbol{w}$ is $N \times 1$ beamsteering weight vector and $\text{AoS}(\boldsymbol{C})$ are physical constraints to avoid overlapping subarrays. Note that orientation of subarrays is not an optimization variable in this architecture, since the polarization of the elements has to be aligned for beamforming. We consider minimization of a weighted linear combination of the objectives, focusing mainly on beamwidth BW and maximum sidelobe level MSLL. The configuration $\boldsymbol{C}$ that we optimize over is characterized by a set of discrete-valued variables, and the number of possible values for these variables is combinatorially explosive. Furthermore, we do not have closed form expressions for the performance measures

5

as a function of $\boldsymbol{C}$, hence significant computation is required to evaluate the cost function for each configuration. In order to control the complexity, we use geometric heuristics to eliminate similar configurations in the first stage of our algorithm, and then employ a second stage of refinement using small perturbations around the first stage solution. We numerically explore the Pareto front for (1.1) by sweeping through the weights, and illustrate how the beam attributes depend on the weights.

2. We evaluate our designs using estimation-theoretic benchmarks for two-dimensional (2D) direction of arrival (DoA) estimation. At low signal-to-noise ratio (SNR), large sidelobes can lead to large errors in the DoA estimate. At high SNR, on the other hand, the DoA estimation error is governed by beam width. We derive a Ziv-Zakai bound (ZZB), which captures the effect of both large and small estimation errors, for DoA estimation for specular paths. The ZZB exhibits a distinct transition in its behavior from low to high SNR, tending at high SNR to the Cramer-Rao bound (CRB), which captures the effect of small errors around the true parameter value. Thus, we use the ZZB transition SNR as a measure of efficacy of sidelobe reduction, and the CRB as a measure of efficacy of beam width reduction.

3. We report in detail on two array designs, $A1$ with primary emphasis on reducing beamwidth and $A2$ based on joint optimization of beamwidth and maximum sidelobe level. These designs are compared against two benchmark arrays. The first is termed a "compact array," with subarrays packed closely together: this is expected to have worse beam width but smaller sidelobes than our sparse designs. The second is termed a "naive array," obtained by placing subarrays in diamond pattern to obtain beamwidth equivalent to that of sparse array $A2$. Some illustrative numerical results for our running example are as follows. The sparse design $A1$ is 11 dB better than the compact array in terms of CRB, while degrading less than 1 dB

in terms of ZZB threshold. The sparse design $A2$ is 4 dB better in terms of CRB than the "naive array," while also having a better ZZB threshold.

4. We investigate DoA estimation performance numerically using a state of the art algorithm for off-grid estimation. The impact of the higher sidelobes due to sparse placement, and hence that of our optimization procedure, is more evident when estimating DoA in the presence of multiple interfering targets. We show that, depending on the strength of interferers, our optimized arrays achieve better estimation accuracy than the "compact" and "naive" benchmark arrays at moderate to high SNR due to a combination of sharper beamwidth and lower sidelobes. We also show that the efficacy of DoA estimation using our sparse designs, and the associated benchmarks, is maintained when we employ compressive measurements.

1.2   Enhanced Estimation accuracy and resolution

While radar-based target localization (i.e., estimation and tracking of position and velocity) is a classical problem with a rich history, it remains an area of active investigation, including recent work on high-resolution joint estimation of range and Doppler [5], as well as multi-target tracking [6]. Chapter 3 of this thesis focuses on the range and doppler estimation using a single radar sensor. For concreteness, we consider Frequency Modulated Continuous Wave (FMCW) chirp waveforms, which are the most widely used modulation scheme for car radars because of the simplicity of hardware and signal processing relative to, say, pulsed radar, which requires separate delay and frequency estimation for range and Doppler, respectively. The FMCW beat signal contains both range and Doppler information embedded in the frequency domain, and is traditionally extracted using an efficiently implementable 2D Discrete Fourier Transform (DFT), with the "fast time" dimension along a chirp, and the "slow time" dimension across several chirps. However,

this technique is susceptible to "off-grid" effects[7]: the signal from a target leaks into several points in the DFT grid, unless it lies exactly on a DFT grid point. While the location estimate can be refined by using a larger number of chirp sequences and sensors, accurate one-shot estimation is especially important for automotive applications, given the importance of timely estimates (which limits the number of frames) and cost/form factor constraints (which limits the number of sensors) [8]. We establish fundamental limits on estimation accuracy and resolution and analyze the performance of recently developed super-resolution algorithms in this single snapshot scenario.

1.2.1   Contributions

Our contributions are listed as follows,

1. We first describe the FMCW signal model for a single sensor and describe the beat signal processing to extract range and doppler using 2D frequency estimation. We also describe super-resolution algorithms that can be used to achieve enhanced accuracy 2D frequency estimates with some additional computational overhead.

2. In order to asses the power requirement at each radar sensor, we calculate the link budget for our system. We then compute estimation theoretic lower bounds on the estimation accuracy to establish that we can indeed hope to obtain satisfactory performance using low cost radar sensors for the short range applications.

3. We show that the super-resolution algorithms approaches the estimation theoretic bound which allows for *cm*-scale accuracy in the operating regime. We also analyze the minimum resolvable distance between targets in proximity. When the range and doppler of two targets lie close to each other, the estimation algorithms are unable to detect them properly. We define a minimum separation criteria in the range doppler space to identify when such anomalies occur.

1.3   Spatial Association

In Chapter 4, we explore the utility of a network of millimeter (mm) wave radar sensors in providing timely situational awareness for highly dynamic environments, by considering estimation of the kinematic state of the scene (i.e., the positions and velocities of targets) via a single set of measurements obtained by a network of sensors. We do not rely on tracking targets across time, or on platform motion to synthesize larger apertures.
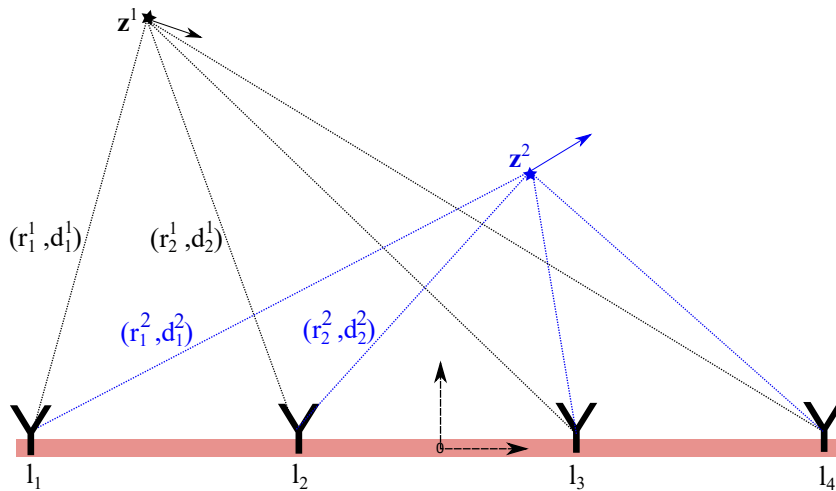
Figure 1.2:   2D System model with linear array of radar sensors placed on x-coordinates, $[l_1, l_2, l_3, l_4]$. The kinematic states $\boldsymbol{z}_1, \boldsymbol{z}_2$ of two targets are to be estimated using the unordered range and doppler observations from sensors.

The specific problem we consider is that of localizing multiple targets in a 2D scene using a linear array of radar sensors. Figure 1.2 shows a scenario with two targets being observed with a linear array of four spatially separated sensors positioned along x-axis ($l_1 - l_2 \gg \lambda$, where λ is the carrier wavelength). Since precise carrier frequency/phase synchronization across sensors separated by 10s-100s of wavelengths is difficult, we assume that that the sensors are monostatic. That is, each sensor collects the relative range and Doppler observations for the targets in the scene. Since these observations are not ordered *a priori*, each range-Doppler measurement must first be associated with a target, and then the measurements associated with a given target from multiple sensors can be used

to estimate its position and velocity. Since the number of possible associations grows exponentially in the number of sensors, it is critical to develop efficient algorithms for spatial association. It is also important to build in robustness to missed detections, since millimeter waves can be easily occluded by objects in the scene.

Our goal is to develop robust, computationally efficient algorithms for single snapshot spatial data association. A key ingredient of our approach is to prune the set of feasible associations based on geometric relationships. Specifically, we observe and exploit linear relationships between functions of the range-Doppler observations for a target across the linear array of sensors. In addition, we are able to discard a significant number of possible associations by the use of the triangle inequality for the range observations at pairs of sensors.

1.3.1   Contributions

Our contributions are listed as follows:

1. We first describe the graphical framework used to solve the association problem. We examine the geometric relations between instantaneous range, Doppler, and sensor locations and show that the features obtained via those geometric relations simplify the association problem.

2. We provide a low-complexity solution for the association problem by introducing a new graph-search based algorithm which exploits geometric fitting error together with likelihood to deal with missed detection and false alarms while reducing the complexity. The initial feasible set of measurements is reduced by principled thresholding (based on CRB), and relaxed over further iterations.

3. The performance of this association algorithm is analyzed and compared against a brute force algorithm and the other algorithms in the literature. We perform

the evaluation in terms of localization accuracy, cardinality errors, robustness, and complexity. In addition, we analyze the advantage of using an enhanced accuracy algorithm (i.e., NOMP [9]) and compare the proposed approach with traditional algorithms.

Chapter 2

Large effective aperture design using array of subarray architecture

2.1   Introduction

In this chapter, we investigate synthesis of a large effective aperture using a sparse array of subarrays. We employ a multi-objective optimization framework for placement of subarrays within a prescribed area dictated by form factor constraints, trading off the smaller beam width obtained by spacing out the subarrays against the grating and side lobes created by sparse placement. We assess the performance of our designs for the fundamental problem of bearing estimation for one or more sources, comparing performance against estimation-theoretic bounds. Our tiled architecture is motivated by recent progress in low-cost hardware realizations of moderately sized antenna arrays (which play the role of subarrays) in the millimeter wave band, and our numerical examples are based on 16-element (4×4) subarrays in the 60 GHz unlicensed band.

Parts of this chapter are reprinted from our journal paper [10], ©2019 IEEE

2.1.1   Related Work

There is a rich body of work on sparsifying linear arrays, including minimum redundancy arrays [11], genetic optimization[12], joint Cramér Rao Bound and sidelobe level optimization [13], and simulated annealing [14]. Most popular design strategies try to find an element pattern which minimizes beamwidth, along with some notion of DoA ambiguities such as sidelobe level or probability of DoA outlier. Recent approaches like Nested 2D arrays [15] and H-arrays [16] utilize the idea of "difference co-array" to reduce the number of redundant spacings and maximize the randomness of element positions, so that the number of spatial frequencies being sampled by the array is maximized.

A closely related sparse array design methodology is the *sensor selection* problem, wherein a smaller subset of individual antenna positions is to be chosen from a predefined grid. By employing certain surrogate measures, near-optimal arrays can be obtained in polynomial time using standard convex relaxation methods[17],[18]. Array thinning methods such as these are well known to avoid complicated nonlinear optimizations for linear case [19].

Most existing techniques, however, assume that antenna elements can be placed freely. Hence, they do not apply in our setting, where element placement within subarrays is constrained. The prior work most similar to our is [20], which investigates design of linear arrays with two and three subarrays. However, the focus there is on performance criteria for comparing a number of sensible designs in a far smaller design space, rather than searching over a large space of possibilities as we do here.

Our performance evaluation requires implementation of DoA estimation algorithms. Classical subspace-based algorithms such as MUSIC [21] and ESPRIT [22], as well as their extensions to arrays of subarrays such as [23, 24, 25, 26], rely on regular array geometries for efficient computation. Recently developed super-resolution algorithms such as Basis

Pursuit Denoising (BPDN) [27] and Newtonized Orthogonal Matching Pursuit (NOMP) [9] are both more general and have better performance. It is worth noting that [28] shows that, for large arrays, BPDN and other sparse estimation techniques with compressive measurements outperform subspace-based methods. We employ NOMP in our numerical experiments, since we have found it to provide better performance than BPDN at lower complexity. We also show that the performance trends are unchanged under compressive measurements, consistent with recent general theory [29].

Map of this chapter: We first describe the beam attributes to be optimized while designing the sparse arrays and discuss constraints for the optimization in Section 2.2. The geometric heuristics and design approach are described in detail in Section 2.3. We then provide a brief review of estimation bounds for 2D bearing estimation and discuss their utility for analyzing the sparse arrays in Section 2.4. Numerical results are provided in Section 2.5. These include exploration of the Pareto front, and comparison of example designs against benchmarks in terms of both beam characteristics and DoA estimation. We show in Section 2.6 that the performance trends hold for compressive DoA estimation as well.

2.2   Sparse Subarray Design

We formulate the array design problem in terms of jointly optimizing multiple beam parameters that are expected to affect DoA estimation performance.

2.2.1   Beam Pattern Basics

We use the directional cosines

$$u = \sin(\theta)\cos(\phi), v = \sin(\theta)\sin(\phi) \tag{2.1}$$
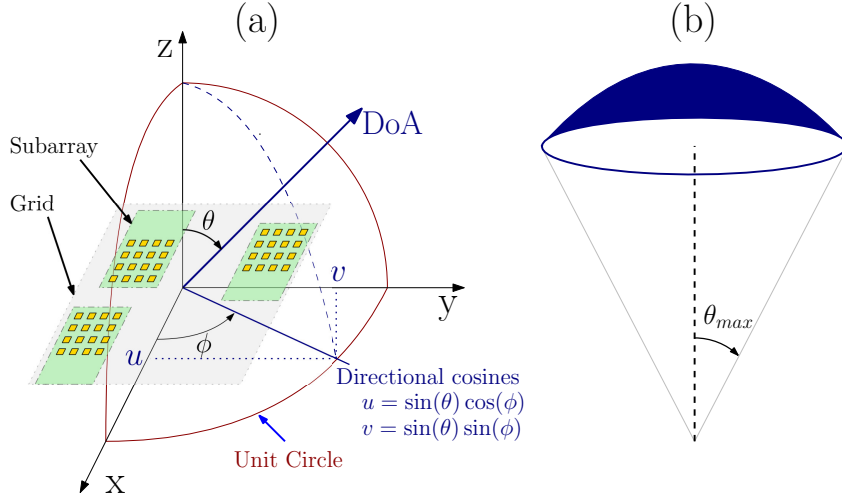
Figure 2.1: (a) 2D Array Geometry and Spherical coordinate system. (b) ROI: Uniform distribution of 2D-DoA $\boldsymbol{u}$ in spherical cap with half angle θ_{max}

to represent the DoA of target. The elevation θ and azimuth ϕ angles are measured from the broadside direction (perpendicular to the baseline array plane). The 2D beampattern $R(u,v)$ in direction (u,v) when the beam is steered towards the broadside is given by

$$R(u,v) = \frac{1}{N^2} \left| \sum_{i=1}^{N} e^{jk\left(ud_i^x + vd_i^y\right)} \right|^2 \tag{2.2}$$

where N is the number of array elements; $[d_i^x, d_i^y]^T \triangleq \boldsymbol{d}_i$ are the 2D co-ordinates of arrays elements and $k = \frac{2\pi}{\lambda}$ is the wavenumber. We assume isotropic antenna elements with ideal steering weights and far-field sources with normalized response. The term "subarray" refers to the subset of elements with uniform half-wavelength spacing, while "super-array" refers to the placement of these subarrays, which is described by the subarray centers. Since the elements in a subarray are fixed, the array element locations, $\boldsymbol{D}$ can be expressed in terms of the subarray centers, $\boldsymbol{C}$, as $\boldsymbol{D} = \boldsymbol{C} \otimes \mathbb{1}_{N_e} + \boldsymbol{D}_e \otimes \mathbb{1}_{N_s}$, where $\boldsymbol{D}_e$ is the fixed $2 \times N_e$ matrix containing the subarray element coordinates with respect to its center, N_s is the number of subarrays, N_e is number of elements in individual subarrays, $\mathbb{1}_n$ is an $n \times 1$ column vector of ones, and $\otimes$ denotes the Kronecker product.

15

When beamforming in a general direction (u_0, v_0) (broadside corresponds to $(u_0, v_0) = (0, 0)$), the beam pattern is given by

$$R_{(u_0, v_0)}(u, v) = R(u - u_0, v - v_0) \tag{2.3}$$

For Direction of Arrival (DoA) estimation, the ideal beam should have small beamwidth with minimal sidelobes and high directivity. We consider the following beam attributes, some of which depend on the steering direction (u_0, v_0), as key performance metrics to be optimized:

- *2D beamwidth* (`BW`): Although the main beam of non-uniform array has non-trivial shape in 2D, we approximate it as an ellipse to define beamwidth. We evaluate the 2D beamwidth in terms of the 3-dB beamwidths along the major and minor axes of this ellipse, denoted by $\mathrm{BW}_{\mathrm{max}}$ and $\mathrm{BW}_{\mathrm{min}}$, respectively. The mean squared error of DoA estimation depends on the sum of these beamwidths (see Appendix A.1), hence we define beamwidth as $\mathrm{BW}^{\mathrm{DoA}} = \sqrt{\mathrm{BW}_{\mathrm{max}}^2 + \mathrm{BW}_{\mathrm{min}}^2}$.

- *Maximum sidelobe level* (`MSLL`): is the relative level of the strongest sidelobe in the beampattern with respect to the main lobe, $\mathtt{MSLL} = 10 \log{(\mathrm{R}_{\mathrm{max}}/\mathrm{R}_{\mathrm{msl}})}$. Thus, R_{max} and R_{msl} are the largest and second largest magnitude local maximas of beampattern $R(u, v)$ given by

$$R_{\mathrm{max}}(u_0, v_0) = \max_{u,v} R_{u_0, v_0}(u, v) = R_{u_0, v_0}(u_0, v_0) = R(0, 0)$$

$$R_{\mathrm{msl}} = \max_{u^*, v^*} \quad R_{u_0, v_0}(u^*, v^*)$$

$$\text{such that} \quad (u^*, v^*) \neq (u_0, v_0),$$

$$R_{u_0, v_0}(u^*, v^*) \geq R_{u_0, v_0}(D_\epsilon(u^*, v^*))$$
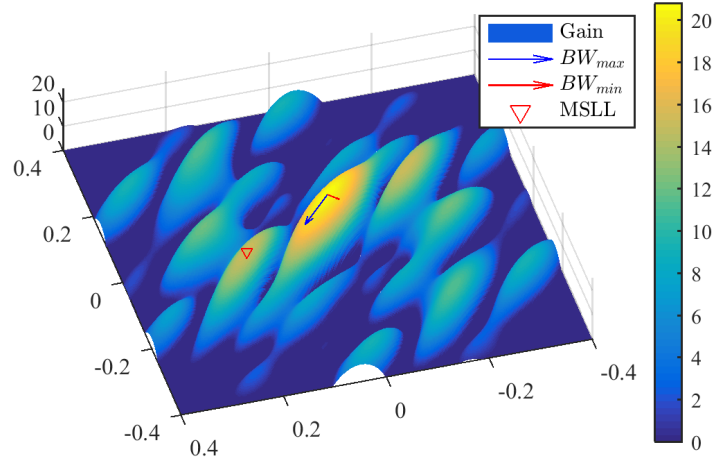
Figure 2.2: Beam Attributes from array Beampattern.

where $D_\epsilon(u^*, v^*) = \{(u, v) : |u - u^*| < \epsilon, |v - v^*| < \epsilon\}$ denotes ϵ-neighborhood. Note that R_{max} does not depend on steering direction (u_0, v_0), but R_{msl} might.

- *Directivity* ($\mathsf{G_D}$): The directivity is the ratio of main lobe power to average power, $\mathsf{G_D} = 10 \log \left(\frac{R_{\mathrm{max}}}{R_{\mathrm{avg}}} \right)$ The average power does not have a closed form expression for general planar arrays, and is evaluated in (u, v) domain by the integral [30]:

$$R_{avg} = \frac{2}{4\pi} \int_{-1}^{1} \int_{-\sqrt{1-v^2}}^{\sqrt{1-v^2}} \frac{R_{u_0,v_0}(u, v)}{\sqrt{1 - u^2 - v^2}} du dv$$

- *Eccentricity* (ecc): is a measure of the asymmetry of the main beam. We add this additional parameter to suppress the trivial linear placement solution, ecc $= \sqrt{1 - (\mathrm{BW_{min}}/\mathrm{BW_{max}})^2}$

For non-uniform planar arrays, none of these beam parameters have a closed form expression [31], hence they must be computed numerically. In our simulations, we compute these beam attributes using a beampattern over a 512×512 grid in UV space as shown in Figure 2.2.

17

2.2.2   Problem Formulation

In order to develop geometric heuristics for optimization, we first analyze the effect of increasing aperture width, keeping the number of antenna elements fixed, for linear and planar arrays, with uniform and subarray-based architectures as shown in the rightmost section of Figure 2.3. In the plots of beam attributes in Figure 2.3, the dashed line represents the aperture width for half-wavelength inter-element spacing, when the uniform and subarray-based configurations match.
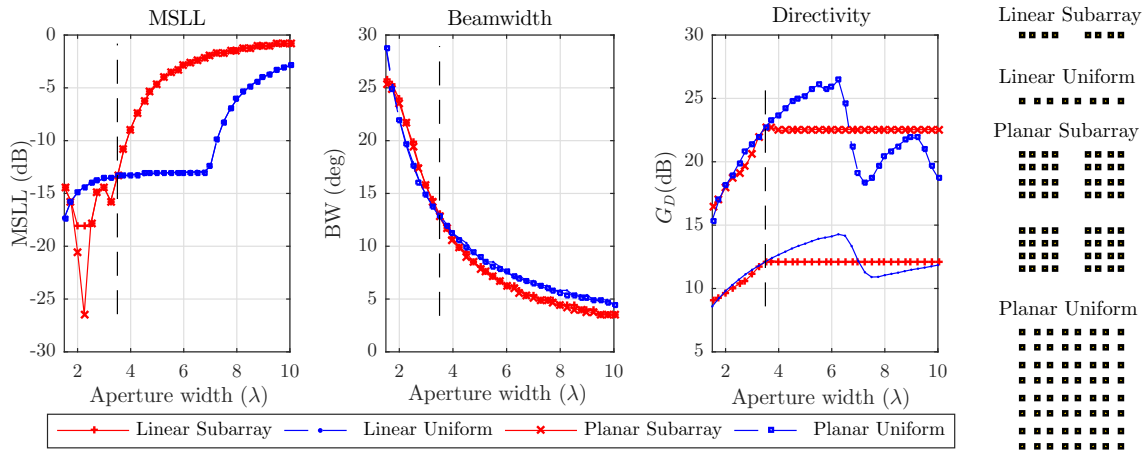
Figure 2.3: Comparison of beam attributes of subarrayed and uniform architecture with increasing aperture width.

- The MSLL for the array of subarrays increases much faster than for a uniform configuration due to a grating lobe appearing close to main beam. This attribute is sensitive to the element distribution and behaves unpredictably for non-uniform arrays.

- The 3dB Beamwidth ($\texttt{BW}^{max}$ for planar array) for both array types reduces congruently, confirming that it is inversely proportional to aperture width independent of the distribution of elements.

- Directivity increases as we increase the inter-element spacing, but only up to a certain limit, and then becomes constant [32]. This generalizes well to planar arrays as shown in the Figure 2.3. As one can see the directivity for subarrayed configurations remains approximately constant with increasing aperture width beyond standard spacing. We therefore do not include this metric in our cost function.

The objectives that we wish to trade off against each other do not have the same units: for example, MSLL is measured in dB relative to the maximum for the main lobe, whereas BW is measured in deg. We therefore normalize each raw objective value, o^{raw} by its range as follows:

$$o(\boldsymbol{C}) = \frac{o^{\text{raw}}(\boldsymbol{C}) - \min\limits_{\forall \boldsymbol{C}'}\left\{o^{\text{raw}}(\boldsymbol{C}')\right\}}{\max\limits_{\forall \boldsymbol{C}'}\left\{o^{\text{raw}}(\boldsymbol{C}')\right\} - \min\limits_{\forall \boldsymbol{C}'}\left\{o^{\text{raw}}(\boldsymbol{C}')\right\}}$$

The range of each objective is computed numerically while constructing the dictionary of all configurations, $\boldsymbol{C} \in \mathcal{C}$, described later in 2.3.1.

The constrained multi-objective optimization can now be formulated as follows:

$$\boldsymbol{C}^*, \boldsymbol{w}^* = \arg\min\limits_{\forall \boldsymbol{C}, \boldsymbol{w}} \quad f(\boldsymbol{C}, \boldsymbol{w})$$
$$\text{subject to} \quad \text{AoS}(\boldsymbol{C})$$

(2.4)

where

$$f(\boldsymbol{C}, \boldsymbol{w}) = \alpha\text{BW}(\boldsymbol{C}, \boldsymbol{w}) + \beta\text{MSLL}(\boldsymbol{C}, \boldsymbol{w}) + \gamma\text{ecc}(\boldsymbol{C}, \boldsymbol{w}) \qquad (2.5)$$

is the weighted cost function in terms of the normalized objective functions and $[\alpha, \beta, \gamma]$ are weights that can be used to sweep through the optimal surface for this optimization. We show some example arrays obtained for different choices of weights in Table 2.1.

Since the cost function $f(\boldsymbol{C}, \boldsymbol{w})$ is evaluated numerically from its beampattern for specific values of $(\boldsymbol{C}, \boldsymbol{w})$, exploring the entire solution space is computationally infeasible.

19

This discrete-valued nature of the optimization variables leads to a combinatorial problem without closed form objectives and constraints. Furthermore, beam characteristics in general depend on the steering weights $\boldsymbol{w}$, which in turn depend on the direction (u_0, v_0) in which we are steering. We therefore employ two key simplifications:

- We remove the dependence of the cost function on beamforming direction, and hence on steering weights, by computing the objectives based on an expanded beam pattern, as discussed in Section 2.2.3.

- We employ geometric heuristics to cut down the solution space to a reasonable size, as described in Section 2.3.

2.2.3   Invariance to Beamforming Direction

The cost function in (2.5) is evaluated using the beampattern $R(u - u_0, v - v_0)$, which depends on the beamsteering direction (u_0, v_0). It would be prohibitively expensive to evaluate the beam attributes over all such beampatterns for finding the optimal $(\boldsymbol{C}, \boldsymbol{w})$. However, for arrays with isotropic elements, we can define an Expanded Beam pattern (EBP) which subsumes beampatterns of all steering direction in a Region of Interest (ROI) [33]. Suppose that our maximum steering angle in the ROI is θ_{max}. From (2.1), we see that (u_0, v_0) lies within a circle of radius $\sin\theta_{max}$. On the other hand, sidelobes can appear at any (u, v) within a circle of radius 1. It is easy to see, therefore, that $(u - u_0, v - v_0)$ is guaranteed to lie within a circle of radius $1 + \sin\theta_{max}$. We can therefore compute beam attributes using the following EBP:

$$R_\rho(\tilde{u}, \tilde{v}) = \frac{1}{N^2} \left| \sum_{i=1}^{N} e^{jk\rho\left(\tilde{u}d_i^x + \tilde{v}d_i^y\right)} \right|^2 \tag{2.6}$$

$$\rho = 1 + \sin(\theta_{max})$$

20

Figure 2.4 shows the EBP, $R_{1.5}(\tilde{u}, \tilde{v})$ for ROI with $\theta_{max} = 30°$, and the beampattern for the steering angle $((u_0, v_0) = (0.3, 0.4))$. The shape of the main beam is preserved under the transformation (2.6), hence beam width and eccentricity can be directly evaluated from (2.6). The MSLL evaluated from EBP is a worst-case value, corresponding to an argument $\rho(\tilde{u}, \tilde{v})$ which, in principle, might not correspond to a feasible value of $(u - u_0, v - v_0)$ in (2.3). However, the maximum sidelobe always lies within the main lobe of the subarray beam pattern, so that physically implausible values of $\rho(\tilde{u}, \tilde{v})$ do not correspond to large local maxima of the EBP.
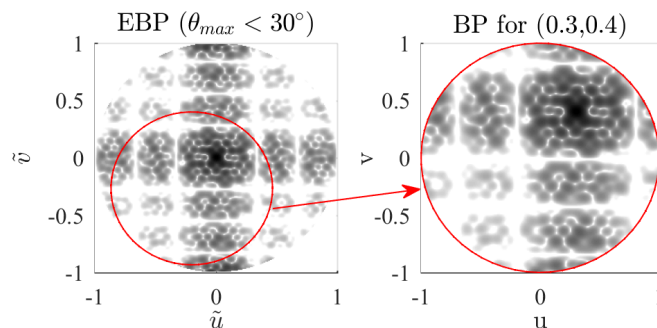
Figure 2.4: Expanded Beampattern for ROI $(\theta_{max} < 30°)$

With the introduction of the EBP, we can, without loss of generality, assume that the main beam is being steered towards broadside, setting $\boldsymbol{w} = \mathbb{1}_N$. Our problem now reduces to finding the optimal configuration $\boldsymbol{C}^*$ as follows,

$$\boldsymbol{C}^* = \arg \min_{\boldsymbol{C}} f(\boldsymbol{C}, \mathbb{1}_N) \quad \text{subject to} \quad AoS(\boldsymbol{C}) \tag{2.7}$$

2.3   Placement Optimization

In order to optimize the placement, we need to evaluate the cost function over all array configurations. The number of configurations depends on the allowed form factor, and the size of the subarray module, and an exhaustive search over all configurations is

computationally infeasible: for example, the number of configurations for a discrete grid of size 20×20 is of the order 10^{20}. We therefore propose a two-stage approach, first performing a combinatorial search on a reduced search space, and then obtaining the final solution by searching over perturbations around the solution from the first stage.

2.3.1 Combinatorial search

We reduce the solution space by removing geometrically "similar" arrays. We employ the covariance of the element positions, and pairwise element separations, as measures of similarity. The choice of covariance of element positions $\mathbf{\Sigma}(\boldsymbol{C})$ as similarity metric is motivated by its inverse proportionality to Cramér Rao Bound on accuracy of DoA estimation (see Section 2.4.1). However, array configurations with similar array covariance but diverse beam attributes also exist: Figure 2.5 shows an example of two array configurations with different shapes but the same covariance. The arrays have similar beamwidth but their MSLL levels are different. We observe that the variance of pairwise element distances $\psi(\boldsymbol{C})$ is different for these arrays, and use it as an indicator for these large scale deviations. This allows us to reduce the dimensionality of the solution space
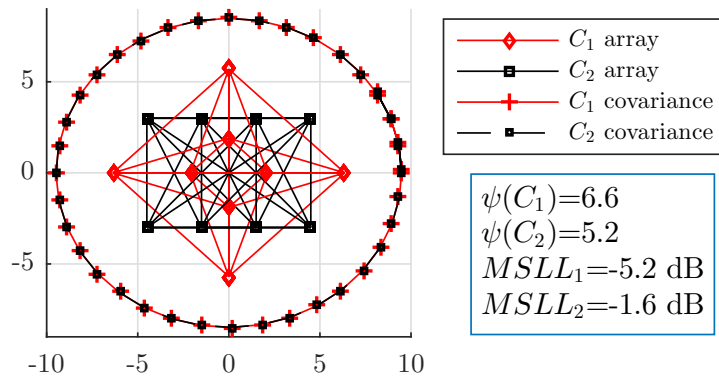
Figure 2.5: Super-arrays with equal covariance but different beam attributes.

from $2 \times N_s$ down to 3 array shape parameters: the eigenvalues (λ_1, λ_2) of $\mathbf{\Sigma}(\boldsymbol{C})$ and $\psi(\boldsymbol{C})$.

Subarray Placement Algorithm

We construct a prefix tree dictionary to find feasible solutions using a breadth first search based enumeration technique. The element position covariance for an array of subarray can be uniquely represented by the covariance of its subarray centers, $\boldsymbol{\Sigma_D} = \boldsymbol{\Sigma_C} + \boldsymbol{\Sigma_{D_e}}$. Hence the super-array center covariance can be used instead of that of the full array in the Dictionary search algorithm. Each node in the tree stores a subarray center position, and the path from root to a node at the nth layer of prefix tree represents a unique configuration of n subarrays. The subarray centers are constrained to lie on a fixed set of discrete grid points G. The algorithm is described in Algorithm 1. We briefly

---

Algorithm 1 Prefix Tree Dictionary Search

1: INITIALIZE: $\mathcal{C}^1 = \left\{ \boldsymbol{C}_i^{(n=1)} \right\}; i \in [1, N_{init}]; n = 1$
2: **while** $n < N_s$ **do**
3:    LIST all vacant Gridpoints $V_i = \mathcal{T}_G(\boldsymbol{C}_i^n); i \in [1, |\mathcal{C}^n|]$
4:    APPEND subarray at vacancies V_i,
   $\hat{\mathcal{C}}^{n+1} = \bigcup\limits_{i=1}^{|\mathcal{C}^n|} \boldsymbol{C}_i^n \times V_i$
5:    PRUNE: $\mathcal{C}^{n+1} \leftarrow$ Prune $\left(\hat{\mathcal{C}}^{n+1} \right)$
6:    $n = n + 1$
7: **end while**
8: Return $\mathcal{C}^{N_s}$

---

discuss the key steps below.

- INITIALIZE: In order to allow for sufficient exploration, we employ multiple random initializations $\boldsymbol{C}_i^1$ of the root node being placed on N_{init} different locations on the grid. (For example, circular configurations cannot be obtained if the root subarray is fixed at the center.)

- LIST: Define the operator $\mathcal{T}_G : G^{|\boldsymbol{C}_i^n|} \rightarrow G^{|V_i|}$ which maps the set of subarrays centers $\boldsymbol{C}_i^n \in \mathcal{C}^n$ to the set of $|V_i|$ vacant gridpoints in G available for placement of

next subarray which are not blocked by the subarrays already placed at $\boldsymbol{C}_i^n$. This operator also accounts for additional surface area occupied by the subarray module apart from the physical antenna elements (see Appendix A.3 for details).

- APPEND: The $(n+1)^{th}$ subarray configuration is constructed from the vacancies, $\boldsymbol{C}_i^n \times V_i$ where $\times$ denotes cartesian product of sets. A temporary dictionary $\hat{\mathcal{C}}^{n+1}$ is formed by inserting $|V_i| = \kappa$ child nodes for each node in the nth layer.

- PRUNE: Nodes corresponding to "similar" configurations are deleted based on the array shape parameters

  1. Find eigenvalues (λ_1, λ_2) of the subarray center covariance matrix, $\Sigma(\boldsymbol{C})$ and variance of array separations, $\psi(\boldsymbol{C}) = \mathbb{E}\left[(l_{ij} - \mathbb{E}[l_{ij}])^2\right]$, where, l_{ij} denotes the distances betweeen i^{th} and j^{th} elements.

  2. Enumerate unique configurations by binning the $(\lambda_1, \lambda_2, \psi)$ triplets over a 3-D grid with resolution τ and randomly picking one configuration from each bin (see Appendix A.4 for criteria to choose τ).

This procedure is repeated until the number of dictionary atoms reach the desired number of subarrays, $n = N_S$. All arrays in the dictionary $\mathcal{C}$ obtained from this algorithm satisfy the AoS$(\boldsymbol{C})$ constraint by construction. This simplifies the constrained multi-objective optimization in (2.4) to

$$\boldsymbol{C}^* = \operatorname*{argmin}_{\boldsymbol{C} \in \mathcal{C}} f(\boldsymbol{C}, \mathbb{1}_N) \tag{2.8}$$

2.3.2   Iterative Placement Refinement

In the second stage, we try to improve the cost function (2.8) by applying small local perturbations (within a bin of the grid G) to the subarray positions obtained from the combinatorial search in the first stage, as described in Algorithm 2.

Algorithm 2 Local Refinements

1: INITIALIZE: $C = C^{init}$; $B =$ oversampled bin.
2: **while** $n < N_{ref}$ **do**
3:    **for** $i = 1$ **to** N_s **do**
4:       LIST Find positions available for adjustment, $V_i = \mathcal{T}_B(C \setminus C_i)$
5:       CORRECT: Select position with least cost $C_i \leftarrow \min_{b \in V_i} f\left(\{(C \setminus C_i), b\}, \mathbb{1}\right)$
6:    **end for**
7:    $n = n + 1$
8: **end while**
9: Return C
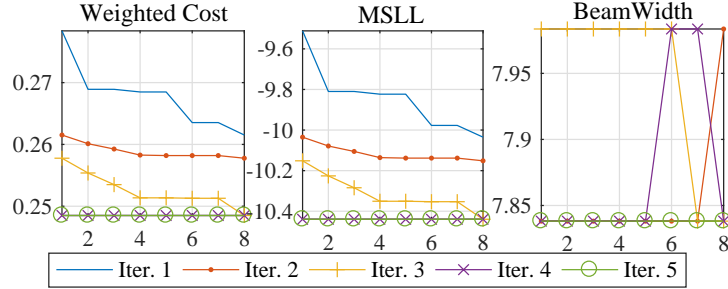
Figure 2.6: Objective costs variation over iterative refinements.

Figure 2.6 shows a sample of how costs are minimized using sequential refinement over $N_s = 8$ subarrays. After running few iterations, the final array has 0.8 dB lower MSLL, while keeping other beam attributes relatively unchanged.

2.3.3   Computational Complexity

The complexity of this approach is dominated by the construction of the prefix tree dictionary $\mathcal{C}$ in the first stage. Our algorithm progresses by growing leaf nodes of the tree in a breadth first fashion until a tree depth of N_s is reached. In each step, the key bottleneck lies in pruning the temporary dictionary $\hat{\mathcal{C}}^n$ which lists all possible vacancies for every leaf node of existing tree.

Algorithm Complexity

The number of operations at the nth iteration of Algorithm 1 is given by

$$T_n = |\hat{\mathcal{C}}^{n+1}| = \sum_{n=1}^{N_s-1} \sum_{i=1}^{|\mathcal{C}^n|} |V_i| \le |G||\mathcal{C}^n| \tag{2.9}$$

where $\mathcal{C}^n$ denotes the set of leaf nodes at the nth level of prefix tree, and $|V_i|$ is the number of vacancies for the ith leaf node. The vacancies are a subset of a grid with cardinality $|G| = (\frac{2R_{max}}{\Delta_g})^2$ where R_{max} is the radius of the aperture and Δ_g is the grid resolution.

The maximum number of array configurations (which correspond to leaves of the prefix tree) in any given iteration is bounded by the maximum number of unique triplets $(\lambda_1, \lambda_2, \psi)$, which can be expressed as follows:

$$|\mathcal{C}^n| \le |\mathcal{C}^n_{max}| = \frac{\lambda_1^{max}}{\tau_{min}} \frac{\lambda_2^{max}}{\tau_{min}} \frac{\psi^{max}}{\tau_{min}} \tag{2.10}$$

where $\lambda_1^{max}, \lambda_2^{max}, \psi^{max}$ represent the maximum value of each parameter and $\tau_{min} = \frac{2\Delta_g^2}{N_s}$ is the minimum bin resolution (using (A.6)). The eigenvalues of the array covariance are bounded by the maximum aperture radius $\lambda_1^{max} < R_{max}^2, \lambda_2^{max} < R_{max}^2$ and the array separation variance can be bounded as

$$\psi = \mathbb{E}\left[(l_{ij} - \mathbb{E}[l_{ij}])^2\right] \le R_{max}^2 \qquad (\because 0 \le l_{ij} \le 2R_{max})$$

Substituting these upper bounds in (2.10) and (2.9), we obtain

$$|\mathcal{C}^n_{max}| \le \left(\frac{R_{max}^2}{\tau_{min}}\right)^3 = N_s^3 \left(\frac{R_{max}^2}{2\Delta_g^2}\right)^3 = \frac{N_s^3 |G|^3}{2^9}$$

$$T_n \le |G||\mathcal{C}^n_{max}| \le \frac{N_s^3 |G|^4}{2^9}$$
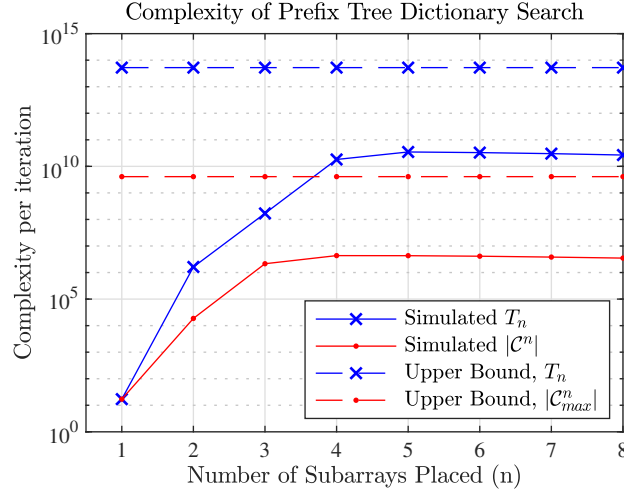
Figure 2.7: Complexity over 12 iterations of Prefix Tree Dictionary Search.

Note that the upper bound derived here is conservative, as can be readily verified through simulations. Figure 2.7 shows the time and space complexity bounds over $N_s = 8$ iterations for a sample run of the algorithm with $|G| = 1600$ grid points. We observe that in practice, computational complexity increases up to $N_s = 4$ but starts reducing afterwards. The latter is because of the reduction in the number of vacancies in the aperture as the space occupied by the existing subarray modules increases.

The total number of operations and space can be upper bounded as follows

$$T_{Algorithm1} = \sum_{n=1}^{N_s-1} |\hat{\mathcal{C}}^{n+1}| \leq \sum_{n=1}^{N_s-1} |G||\mathcal{C}^n_{max}| \sim O\left(|G|^4 N_s^4\right)$$

$$S_{Algorithm1} = \max_{n \in [1,N_s]} |\mathcal{C}^n| \leq |\mathcal{C}^n_{max}| \sim O\left(|G|^3 N_s^3\right)$$

The resulting dictionary is independent of cost function weights $[\alpha, \beta, \gamma]$, and represents a thinned version of the entire design space. Thus, optimized arrays for different weights can be evaluated by solving (2.8). The solution of (2.8) has $O(|\mathcal{C}|)$ time complexity, assuming that cost evaluation for each array configuration takes constant time. The second stage of the algorithm requires cost evaluation of fine perturbations over an over-

sampled bin of size $|B|$ around each subarray, repeated N_{ref} times. This stage requires $T_{Algorithm2} = |B|N_{ref}N_s$ operations using constant space, which is significantly lower compared to first stage. Hence, the overall algorithm complexity is $O(|G|^4 N_s^4)$ in time and $O(|G|^3 N_s^3)$ in space.

We note that the polynomial complexity of proposed algorithm is significantly better compared to exhaustive search, which exhibits exponential complexity $O(|G|^{N_s})$. For our running example, the proposed algorithm's complexity is $T_{Algorithm1} = (400 \times 8)^4 \approx 10^{14}$ compared to the complexity of exhaustive search, $T_{Exhaustive} = (400)^8 > 10^{20}$.

2.4   Estimation-Theoretic Benchmarks

We now seek to evaluate the efficacy of our sparse designs for the canonical application of 2D DoA estimation. We compare different array designs in terms of estimation-theoretic bounds as well as simulated performance using a super-resolution algorithm. For clarity in exposition, from here onwards we overload $\boldsymbol{u} \triangleq [u, v]$ to denote the DoA.

2.4.1   Signal Model

We model the received signal from K sources in the scene with distinct DoAs $\Theta = [\boldsymbol{u_1}, \boldsymbol{u_2}, \cdots, \boldsymbol{u_k}]$ as

$$\boldsymbol{x} = \sum_{j=1}^{K} \alpha_j \boldsymbol{s}(\boldsymbol{u}_j) + \boldsymbol{z} \tag{2.11}$$

where $\boldsymbol{s(u_j)} = \left[e^{jk\boldsymbol{u_j^T d_1}}, \ldots, e^{jk\boldsymbol{u_j^T d_N}} \right]^T$ is the array response, $\boldsymbol{z} = [z_1, \ldots, z_N]^T$ is complex white noise such that $\mathbb{E}(zz^H) = \sigma^2 I_N$, and $\{\alpha\}_{j=1}^{K}$ are complex gains which are unknown deterministic constants. The joint probability density of received signal conditioned on

$(\Theta, \{\alpha\}_{j=1}^{K})$ is given by,

$$p(\boldsymbol{x}|\Theta, \boldsymbol{\alpha}) = \prod_{\boldsymbol{u}_j \in \Theta} \frac{1}{\pi^N \sigma^2} \exp\left(-\frac{\|\boldsymbol{x} - \alpha_j \boldsymbol{s}(\boldsymbol{u}_j)\|^2}{\sigma^2}\right) \tag{2.12}$$

For any DoA estimator $\hat{\Theta}$, the covariance of estimation error is defined as,

$$\boldsymbol{R}_\epsilon(\hat{\Theta}) = \mathbb{E}\left[\sum_{i=1}^{K}(\boldsymbol{u} - \hat{\boldsymbol{u}_i})(\boldsymbol{u} - \hat{\boldsymbol{u}_i})^T\right]$$

$\boldsymbol{R}_\epsilon$ can be geometrically interpreted by its trace $\sqrt{tr(R_\epsilon)}$ which represents the expected overall Root mean square error (RMSE) in DoA estimation (see Appendix A.1). We use this measure to compare the performance of array designs in Section 2.5. For single source case ($K = 1$), the joint maximum likelihood estimator of $\boldsymbol{u}$ and α yields a noncoherent estimator for $\boldsymbol{u}$ as follows:

$$\hat{\boldsymbol{u}}_{ML} = arg \max_{\boldsymbol{u}} \left|\boldsymbol{s}(\boldsymbol{u})^H \boldsymbol{x}\right|^2 \tag{2.13}$$

For this case, we derive the Cramer Rao (CRB) and Ziv-Zakai (ZZB) bounds on $\boldsymbol{R}_\epsilon$ to assess the best possible estimation accuracy of different designs. Although derived for single source case, we use these bounds for multiple source case as well to compare DoA estimation performance.

Cramér Rao Bound

The Bayesian Cramér Rao Bound for this signal model is given by [33]:

$$CRB(\boldsymbol{R}_\epsilon) = (\boldsymbol{J_F} + \boldsymbol{J_P})^{-1} \tag{2.14}$$

where $\boldsymbol{J_F}, \boldsymbol{J_P}$ denote the Fisher Information Matrix (FIM) contributions from the observation and the prior distribution of DoA respectively.

$$(\boldsymbol{J_F})_{ij} = -\mathbb{E}_{\boldsymbol{x},\boldsymbol{u}}\left[\frac{\partial^2 l(\boldsymbol{x}|\boldsymbol{u})}{\partial u_i \partial u_j}\right], (\boldsymbol{J_P})_{ij} = -\mathbb{E}_{\boldsymbol{u}}\left[\frac{\partial^2 l(\boldsymbol{u})}{\partial u_i \partial u_j}\right]$$

where $l(\boldsymbol{x}|\boldsymbol{u})$ and $l(\boldsymbol{u})$ are the conditional log likelihood and prior log likelihoods, respectively. In addition, the following regularity condition needs to be satisfied,

$$\mathbb{E}_{\boldsymbol{x},\boldsymbol{u}}\left[\frac{\partial l(\boldsymbol{x}|\boldsymbol{u})}{\partial \boldsymbol{u}}\right] = \boldsymbol{0}$$

$$\mathbb{E}_{\boldsymbol{x},\boldsymbol{u}}\left[jk\sum_{i=1}^{N}\boldsymbol{d}_i\left(x_i e^{jk\boldsymbol{u}^T\boldsymbol{d}_i} - x_i^* e^{-jk\boldsymbol{u}^T\boldsymbol{d}_i}\right)\right] = \boldsymbol{0}$$

$$jk\left(\alpha\sum_{i=1}^{N}\boldsymbol{d}_i - \alpha^*\sum_{i=1}^{N}\boldsymbol{d}_i\right) = jk(\alpha-\alpha^*)\sum_{i=1}^{N}\boldsymbol{d}_i = \boldsymbol{0}$$

In order to always satisfy this condition, we enforce the array element positions to be centered i.e., $\sum_{i=1}^{N}\boldsymbol{d}_i = \boldsymbol{0}$.

For a single source, the FIM is given by,

$$J_F = -\frac{1}{\sigma^2}\mathbb{E}\left[\frac{\partial \boldsymbol{s}(\boldsymbol{u})}{\partial \boldsymbol{u}}^H \frac{\partial \boldsymbol{s}(\boldsymbol{u})}{\partial \boldsymbol{u}}\right] \tag{2.15}$$

$$= 2k^2\gamma \boldsymbol{D}^T \boldsymbol{D} \tag{2.16}$$

which depends only on the element positions, $\boldsymbol{D}$ and Signal to Noise ratio (SNR) ($\gamma = |\alpha|^2/\sigma^2$). Assuming the DoA prior to be uniformly distributed in the ROI ($\theta \leq 30°$), the prior FIM simplifies to $\boldsymbol{J_P} = 1.343\boldsymbol{I}_2$.

Ziv-Zakai Bound

The CRB is a local bound, which accounts for estimation performance dependent on mainbeam, hence it is only useful at high SNR. In order to better characterize the estimation performance of Sparse arrays at low SNR, we calculate the Ziv-Zakai Bound (ZZB) which incorporates the effect of sidelobes and predicts the threshold behavior. For any directional vector $\boldsymbol{a} = [\cos\xi, \sin\xi]^T$, the ZZB is given by [34]

$$\boldsymbol{a}^T \boldsymbol{R}_\epsilon \boldsymbol{a} \geq \int_0^\infty \mathcal{V} \left\{ \max_{\boldsymbol{\delta}:\boldsymbol{a}^T\boldsymbol{\delta}=h} \int A(\boldsymbol{u}, \boldsymbol{\delta}) P_e(\boldsymbol{u}, \boldsymbol{\delta}) d\boldsymbol{u} \right\} h \, dh$$

where, $A(\boldsymbol{u}, \boldsymbol{\delta}) = \min\{p(\boldsymbol{u}), p(\boldsymbol{u}+\boldsymbol{\delta})\}$, $\mathcal{V}(.)$ is the valley filling function and $P_e(\boldsymbol{u}, \boldsymbol{\delta})$ is error probability of the following vector parameter binary detection problem,

$$H_0 : \hat{\boldsymbol{u}} = \boldsymbol{u}; \quad Pr(H_0) = \frac{1}{2}, \boldsymbol{x} \sim p(\boldsymbol{x}|\boldsymbol{u})$$

$$H_1 : \hat{\boldsymbol{u}} = \boldsymbol{u} + \boldsymbol{\delta}; \quad Pr(H_1) = \frac{1}{2}, \boldsymbol{x} \sim p(\boldsymbol{x}|\boldsymbol{u}+\boldsymbol{\delta})$$

This error probability can be lower bounded by the minimum probability of error of the following optimal non-coherent detector:

$$\text{Decide}(\boldsymbol{u}) = \begin{cases} \boldsymbol{u} & \text{if } \rho_1 > \rho_2 \\ \boldsymbol{u} + \boldsymbol{\delta} & \text{if } \rho_1 < \rho_2 \end{cases}$$

where $\rho_1 = |\boldsymbol{x}^H \boldsymbol{s}(\boldsymbol{u})|$ and $\rho_2 = |\boldsymbol{x}^H \boldsymbol{s}(\boldsymbol{u}+\boldsymbol{\delta})|$. Given $\boldsymbol{u} = \boldsymbol{u_0}$, ρ_1, ρ_2 are rician distributed with scale parameter $s = \sigma^2/M$ and non-centrality parameter $\nu = |\alpha|N, |\alpha R(\boldsymbol{\delta})|N$ respectively where $R(\boldsymbol{\delta}) = R(\delta_x, \delta_y)$ is the beampattern from (2.2). The error probability

is given by [35]

$$P_{nc}(\boldsymbol{u}, \boldsymbol{\delta}) = \frac{1}{2} \left(Pr\left(\rho_1 < \rho_2 | \boldsymbol{u}\right) + Pr\left(\rho_1 > \rho_2 | \boldsymbol{u} + \boldsymbol{\delta}\right) \right)$$

$$= Pr\left(\rho_1 < \rho_2 | \boldsymbol{u}\right)$$

$$= Q_1(a, b) - \frac{1}{2} e^{-\frac{a^2 + b^2}{2}} I_0(ab) \tag{2.17}$$

where,

$$a = \sqrt{\frac{\gamma N}{2} \left(1 - \sqrt{1 - |R(\boldsymbol{\delta})|^2} \right)}$$

$$b = \sqrt{\frac{\gamma N}{2} \left(1 + \sqrt{1 - |R(\boldsymbol{\delta})|^2} \right)}$$

which is not a function of $\boldsymbol{u}$. For ROI in our case, the maximum error $h^{(\max)} = \left(\boldsymbol{a}^T \boldsymbol{\delta} \right)^{(\max)} = 1$. Note that for a uniformly distributed DoA in spherical coordinates (θ, ϕ), the distribution of $\boldsymbol{u}$ is not uniform. However for simplicity of analysis, we make the assumption that $\boldsymbol{u}$ is uniformly distributed on a circular disc. Hence, the ZZB expression simplifies to

$$\boldsymbol{a}^T \boldsymbol{R}_\epsilon \boldsymbol{a} \geq \int_0^1 \mathcal{V} \left\{ \max_{\boldsymbol{\delta} : \boldsymbol{a}^T \boldsymbol{\delta} = h} \int A(\boldsymbol{u}) d\boldsymbol{u} P_{nc}(\boldsymbol{\delta}) \right\} h \, dh$$

$$ZZB(\boldsymbol{a}^T \boldsymbol{R}_\epsilon \boldsymbol{a}) = \int_0^1 \mathcal{V} \left\{ \max_{\boldsymbol{\delta} : \boldsymbol{a}^T \boldsymbol{\delta} = h} P_{nc}(\boldsymbol{\delta}) \right\} h \, dh \tag{2.18}$$

The maximum error probability over all directions $\boldsymbol{\delta}$ cannot be expressed as closed form expression. However, due to the monotonicity of Marcum's Q function, $Q_1(.)$ and Bessel function of 0th order, $I_0(.)$, the error probability in (2.17) is maximized only when $R(\boldsymbol{\delta})$ is maximized. Therefore, for each values of h, we compute the $\max_{\boldsymbol{\delta} : \boldsymbol{a}^T \boldsymbol{\delta} = h} |R(\boldsymbol{\delta})|$ numerically by searching over a discrete set of points on the line segment $\boldsymbol{a}^T \boldsymbol{\delta} = h$ and substitue in (2.18).

2.4.2   DoA estimation algorithm

Grid-based sparse estimation for a set of DoAs models the the received signal (2.11) as follows:

$$x = S(\Psi)b + z \tag{2.19}$$

where $S(\Psi) = \begin{bmatrix} s(u_1) \cdots s(u_{|\Psi|}) \end{bmatrix}$ contains the array response at discretized set of DoAs $u_i \in \Psi$ as columns. The nonzero entries in b point to presence of target in the corresponding DoA in Ψ. The DoA and gain pair $(\hat{u}_i, \hat{\alpha}_i)_{i=1}^{K}$ can be estimated by jointly minimizing the residual power,

$$T(\hat{u}, \hat{\alpha}) = \left\| x - \sum_{j=1}^{K} \hat{\alpha}_j s(\hat{u}_j) \right\|^2$$

The NOMP algorithm summarized below provides a two stage estimator:

1. *Detection*: Using precomputed $S(\Psi)$, coarse estimates of DoA and complex gain are obtained

$$\hat{u} = arg \max_{u \in \Psi} |s(u)^H x|^2$$

$$\hat{\alpha} = s(u)^H x / N$$

2. *Refinement*: The estimates are refined using the Newton method:

$$\hat{u}' = \hat{u} - \left(H_\nabla T(\hat{u}, \hat{\alpha}) \right)^{-1} \nabla T(\hat{u}, \hat{\alpha}) \tag{2.20}$$

$$\hat{\alpha}' = s(\hat{u}')^H x / N \tag{2.21}$$

where $H_\nabla T$ and ∇T denote the Hessian and gradient of $T(u, \alpha)$ with respect to u

at current estimate $(\hat{\boldsymbol{u}}, \hat{\alpha})$ (see [36] for details).

The algorithm is repeated with the residual signal, $\boldsymbol{r} = \boldsymbol{x} - \hat{\alpha}'\boldsymbol{s}(\hat{\boldsymbol{u}}')$ to estimate other DoAs. The *refinement* steps are repeated after each new detection for all DoAs in a cyclic manner for few rounds to improve accuracy.

The algorithm yields K_{est} DoA estimates, with estimation performance degrading when K_{est} does not match the true number of DoAs, K_{DoA}. Hence, in order to evaluate the arrays independent of such errors, we implement both algorithm where $K = K_{DoA}$ is known.

We also run extensive simulations with another state of the art algorithm, BPDN [27], with default parameters and 5 refinement stages. The computational complexity of BPDN is significantly higher than that of NOMP. The grid $\boldsymbol{\Psi}$ needs to be adapted at each iteration for BPDN, depending on the DoAs, whereas it remains fixed for NOMP $\boldsymbol{S}(\boldsymbol{\Psi})$, and can be precomputed, which makes it suitable for faster implementation in large arrays. Since the NOMP algorithm also yields somewhat better estimation accuracy than BPDN, we only present results obtained with NOMP here.

2.5   Numerical Results

2.5.1   Design of arrays

Using the combinatorial search algorithm, we create a search space of array configurations, $\boldsymbol{C} \in \mathcal{C}$ of size $|\mathcal{C}| = 657,000$ for $N_{sub} = 8$ subarrays. Figure 2.8a shows the values of two major objectives, `MSLL, BW` over this space. The beamwidth is improved by spreading out the subarrays, but this typically leads to a deterioration in the MSLL. Figure 2.8a clearly shows the Pareto front corresponding to the multiple solutions of (2.8), corresponding to different relative weights, trading off these opposing objectives.

(a) Beam attributes of array dictionary $\mathcal{C}$, Sample arrays on Pareto optimal front obtained from first stage dictionary search ($\diamond$) and second stage iterative placement refinement ($\square$).

(b) Weighted cost function $f(\boldsymbol{C}, \mathbb{1}_N)$, $\boldsymbol{C} \in \mathcal{C}$ for weights $(0.1, 0.5, 0.1)$ as a function of the eigenvalues of the array covariance matrix $\Sigma(C)$.

(c) Array configuration & beampattern for solution B.
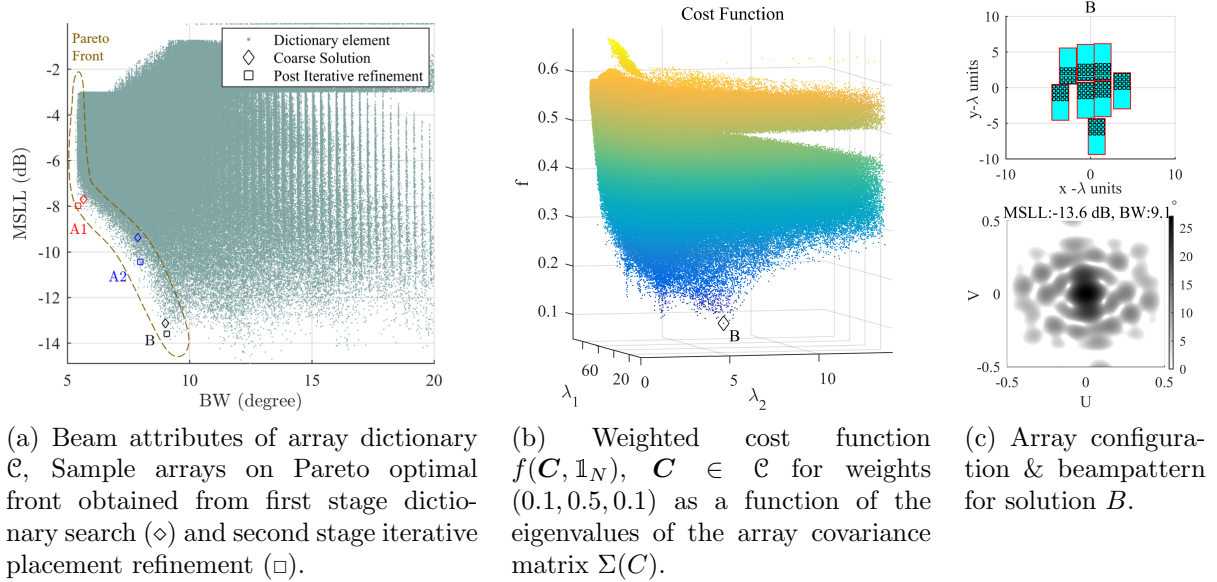
Figure 2.8: Pareto-front exploration and multi-objective optimization.

Figure 2.8b shows the weighted cost function obtained for an example set of weights ($\alpha = 0.1, \beta = 0.5, \gamma = 0.1$) as a function of the eigenvalues of the array covariance matrix. We observe that for a similar set of eigenvalues, many of the solutions we explore (shown in yellow) are substantially worse in terms of the weighted cost than the solutions shown in blue from which we choose our solutions, indicating the complexity of the optimization landscape. Choosing one more variable, the variance of the element locations $\psi(\boldsymbol{C})$, for binning is therefore crucial for exploring this landscape more thoroughly. Figure 2.8c shows the array B obtained using the proposed algorithm, and its beampattern. We mark the locations of B, and of two other Pareto optimal designs, $A1$ and $A2$ (to be discussed shortly) along the Pareto front in Figure 2.8a.

As we change the relative values of weights α, β and γ in exploring the Pareto front, we can make the following observations regarding the corresponding subarray placements:

- For a larger relative value of α (more importance given to beamwidth), the subarrays are widely distributed over the available aperture area.

35

- When we increase the relative value of β to suppress MSLL, the array becomes restricted to a smaller area.

- The relative weight of γ, which corresponds to the objective of reducing eccentricity, affects both the shape of the main lobe and the positions of the sidelobes. For positive γ, the solution is not expected to lie on the `BW-MSLL` Pareto front boundary. Indeed, Figure 2.8a shows that the solutions from first stage dictionary search lie slightly away from this boundary. However, the second stage iterative refinement reduces this gap.
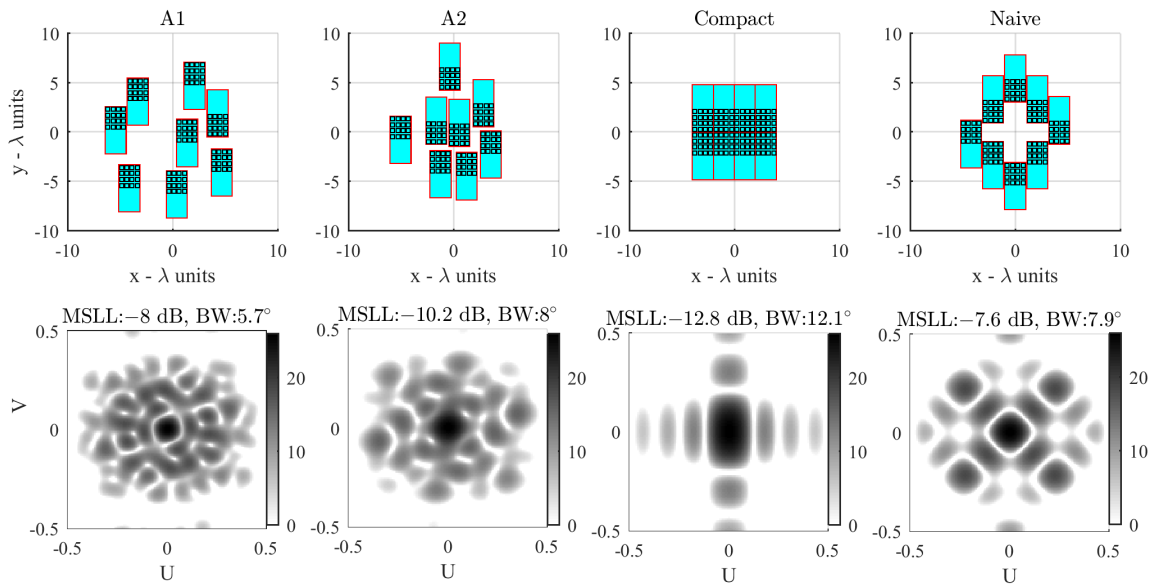
Figure 2.9: Beam patterns (Bottom row) for designed (Left half) & benchmarking (right half) arrays.

Based on these observations, we set the weights to obtain following sample array configurations:

1. *A1*: Primary emphasis is given towards minimizing beamwidth by setting $\alpha = 1$, $\beta, \gamma = 0.1$.

36

2. *A2*: In this case, we emphasize all beam attributes by setting all weights equal to 1.

Table 2.1: Sample Array Configurations

Shape	α	β	γ	MSLL	BW	ecc
A1	1	0.1	0.1	-8 dB	5.7°	0
A2	1	1	1	-10.2 dB	8°	0
Compact	-	-	-	-12.8 dB	12.1°	0.7
Naive	-	-	-	-7.6 dB	7.9°	0.0

We compare these array designs against two simple array configurations, 1) a "compact" array where subarrays are placed together such that overall element pattern becomes a uniform rectangular array, 2) a "naive" array where subarrays are spread along a diamond shape such that its resultant beamwidth is equal to that of *A2*. Table 2.1 lists the weights and resulting beam attributes of these arrays.

Figure 2.9 shows the array designs obtained using our optimization approach and their beam patterns. The *A2* array has a sharp beamwidth and only 2.6 dB worse MSLL compared to the compact array. On the other hand, a naive sparse array with circular arrangement of subarrays yields 2.6 dB higher MSLL compared to *A2* for similar beamwidth. Our designs *A1, A2* exhibit several small sidelobes (the highest sidelobe for *A2* is -10.2 dB), whereas the naive array exhibits fewer but more pronounced sidelobes. Since large sidelobes and grating lobes can cause large errors in DoA estimation, we expect our designs to yield better estimation performance, which is borne out by the results presented in the next section.

We note that the sidelobe levels and locations are primarily dependent on the super-array (i.e., the location of subarray centers $\boldsymbol{C}$), while the subarray pattern mainly affects the large-scale beampattern. Therefore, we obtain similar solutions, with similar beam

characteristics, using our optimization approach with small variations in the subarray element patterns (e.g, replacement of a rectangular pattern with a plus pattern).

2.5.2   Comparison of Estimation Performance

We evaluate the arrays based on their DoA estimation accuracy at different SNRs for both single and multiple source cases. We use the RMSE in estimating DoA for comparison which is given by $\bar{\epsilon} = \sqrt{\mathbb{E}[|\hat{\boldsymbol{u}} - \boldsymbol{u_0})|^2]} = \sqrt{tr(\boldsymbol{R_\epsilon})/2}$.
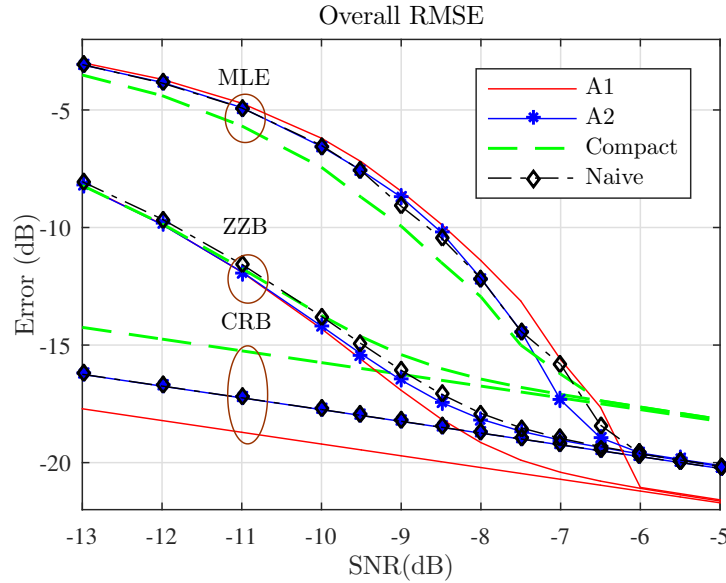
Figure 2.10: Comparison of estimation theoretic bounds for arrays.

Estimation bounds

The Cramér Rao Bound is evaluated using (2.14), $CRB(\bar{\epsilon}) = \sqrt{tr(CRB(\boldsymbol{R_\epsilon}))/2}$. The Ziv Zakai Bound is evaluated using (2.18),

$$ZZB(\bar{\epsilon}) = \sqrt{ZZB(\boldsymbol{a_1^T R_\epsilon a_1}) + ZZB(\boldsymbol{a_2^T R_\epsilon a_2})}$$

where a_1, a_2 denote the directions of maximum and minimum beamwidths of the array. We also computed the ML estimation (MLE) error by Monte Carlo simulation using (2.13) with an overcomplete dictionary of array responses. Figure 2.10 shows the CRB, ZZB and MLE curves for all the arrays. CRB is proportional to beamwidth (see Appendix A.2 for details). The ZZB bound converges to CRB at the so-called "ZZB threshold" SNR: when the SNR is below this threshold, far-ambiguities in DoA estimation caused by large sidelobes dominate the MSE. The tradeoff between beamwidth and MSLL is thus expected to translate to one between CRB (better with smaller beamwidth) and ZZB threshold (worse with larger MSLL). Thus, as expected, "*A1*" array achieves the lowest CRB, followed by "*naive*" and "*A2*" with equal CRB, while "*Compact*" array has the largest beamwidth and hence highest CRB. The trend in MSLL is weakly reflected in the ZZB thresholds (for a single target, sidelobes do limited damage): the degradation in ZZB threshold, relative to that of the compact array for the optimized arrays (*A1, A2*) is less than 1 dB, while the gain in CRB due to smaller beamwidth is 4 dB and 2 dB, respectively. The MLE error curve also agrees with the threshold behavior predicted by ZZB. We see in the next set of results, however, that the size of the sidelobes becomes much more important when we consider multiple targets.

Estimation algorithm performance

We obtain DoA estimates using the *NOMP* algorithm [9, 36] with a known number of sources to compare the best case performance of these arrays. (The NOMP algorithm also performs as well as the brute force MLE for a single target discussed earlier–results omitted here.) The RMSE is evaluated across $N = 1024$ DoAs uniformly sampled over the ROI (spherical cap of half angle 30°). For evaluating the estimation performance in presence of multiple targets, ($K = 5$) we compute the RMS error in the DoA estimate for a primary target fixed at broadside, while interfering targets are distributed uniformly in

ROI at separation of $\Delta \boldsymbol{u} \geq 0.16$ or $\Delta \theta \geq 9.2°$ away from primary target. This separation is imposed because the estimation problem is ill-posed for DoAs in close proximity. For uniform arrays, the minimum separation is typically defined with respect to the DFT bin size (e.g. $\Delta_{\text{DFT}} = 2\pi/L$ for an L-element linear array). Since this quantity cannot be defined for non-uniform planar arrays, we choose a minimum separation halfway between the RMS beamwidths of the "compact" and sparse arrays, to capture the effect of both local errors and far ambiguity errors due to sidelobes.

In addition to RMSE vs SNR curves, we also analyze the distribution of error magnitudes. The complementary cumulative distribution (CCDF) of the estimation errors is used to compare the "outage probability" corresponding to too large an error, which captures the impact of large sidelobes.

- With multiple sources, the estimation accuracy is degraded by interference from other sources, and RMSE does not converge to the single-target CRB. Figure 2.11 shows the estimation performance for strong and weak interference.

  1. Weak interference: When the interfering sources are 6 dB weaker than primary target, sparse arrays offer more than 5 dB SNR gain compared to compact arrays for $SNR > -5$ dB. Also, the difference between *A2, naive* array widens to about 1 dB in the threshold region indicating the benefit of suppressing sidelobes.

  2. Strong interference: When interfering sources have same magnitude, RMSE severely degrades for both arrays with high sidelobes (*A1, Naive*) as well as arrays with high beamwidth (*Compact*). On the other hand, *A2* has lowest RMSE at $SNR > -5$ dB because of the dual benefit of small beamwidth and lower sidelobes.
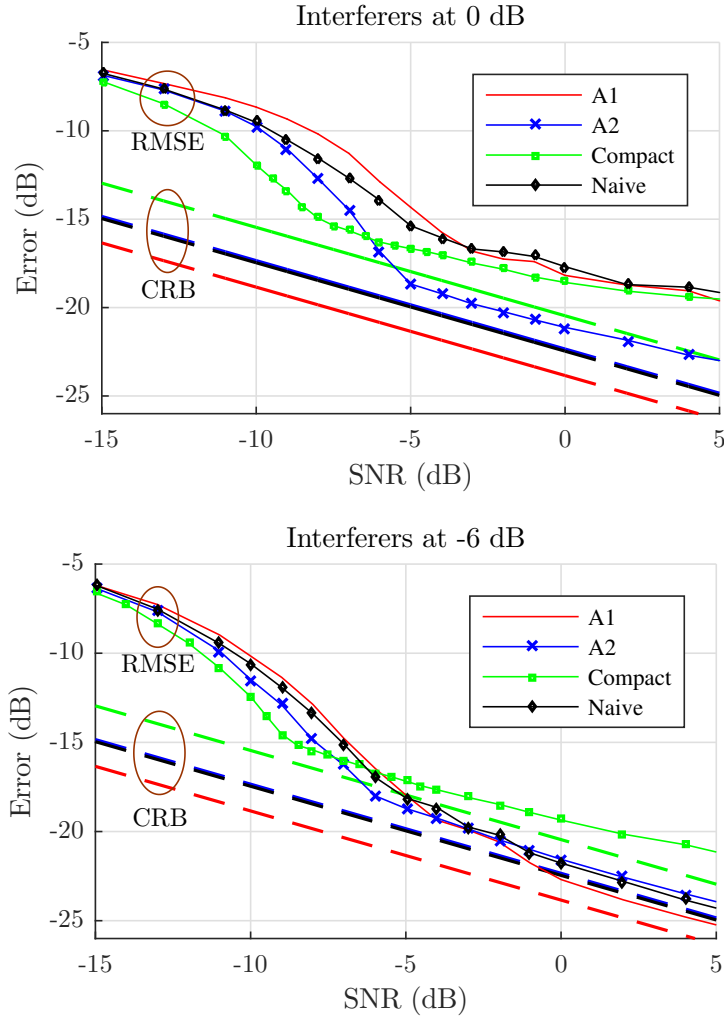
Figure 2.11: Estimation accuracy with multiple targets.

- The increase in estimation errors at high SNR is attributed to ambiguity errors from sidelobes, hence the overall sidelobe suppression for the arrays can be compared using the distribution of these error magnitudes. Figure 2.12 shows the CCDF curves of all arrays at SNR=−5 dB. The initial curvature of these curves (RMSE upto -22 dB) is expected to depend on local errors, hence the rate of change follows same order as CRB which is $A1 > A2 = naive > compact$. But the curvature reverses order at higher RMSE indicating the tradeoff with far-errors. We can see that $A2$ achieves lower outage probability in both scenarios (e.g. for RMSE
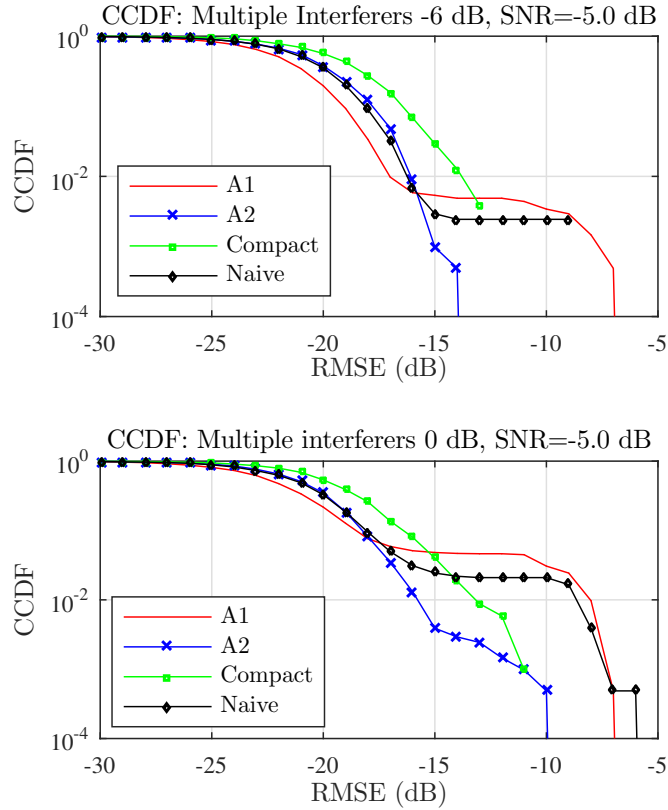
Figure 2.12: CCDF of estimation errors in multiple targets.

threshold set to -15 dB) as it strikes a balance between near and far errors. In contrast, both *A1* and *naive* exhibit high outage probability due to frequent far ambiguity errors caused by higher sidelobes.

Therefore, depending on the expected magnitude of interferers either one of the designed arrays with suitable sidelobe suppression can be selected. For a desired beamwidth reduction our design algorithm yields an array superior to a naively designed sparse array.

2.6   Compressive Estimation

We now evaluate the arrays for sparse estimation using compressive measurements at each subarray given by:

$$y = \Phi x$$

where x is the full measurement from (2.19) and $\Phi = \text{diag}(\Phi_1, \cdots, \Phi_{N_s})$ is the $M \times N$ measurement matrix consisting of the subarrays measurement matrices as its block diagonals. Each subarray takes M_i compressive measurements with an independent $\Phi_i \in \mathbb{C}^{M_i \times N_e}$ whoose elements are chosen uniformly and independently from QPSK samples $\frac{1}{\sqrt{M_i}} \{\pm 1, \pm j\}$. In addition, columns of Φ_i have unit norm to preserve signal norm on average ($\mathbb{E}\left[||\Phi S(u)||^2\right] = ||S(u)||^2$) while scaling noise variance by N/M. The underlying DoA, u can be extracted by minimizing the ML cost:

$$\left\| y - \Phi \sum_{j=1}^{K} \hat{\alpha}_j s(\hat{u}_j) \right\|^2$$

The efficacy of compressive parameter estimation in AWGN depends on preserving the geometric structure of the parameterized signals [29]. Specifically, if Φ satisfies the $2K$ isometry property for discretized basis $S(\Psi)$ [29],

$$C(1 - \epsilon) \leq \frac{|\Phi S(\Psi) b|^2}{|S(\Psi) b|^2} \leq C(1 + \epsilon) \tag{2.22}$$

where C is a constant for any arbitrarily chosen $2K$ sparse vector b, the performance of the compressive system follows that for the original system, except for an SNR penalty of M/N. Figure 2.13 shows the minimum and maximum values of this ratio over 10^6 random realization of 8 sparse b for sparse array. The ratio is within $[-5, 3]$ dB for
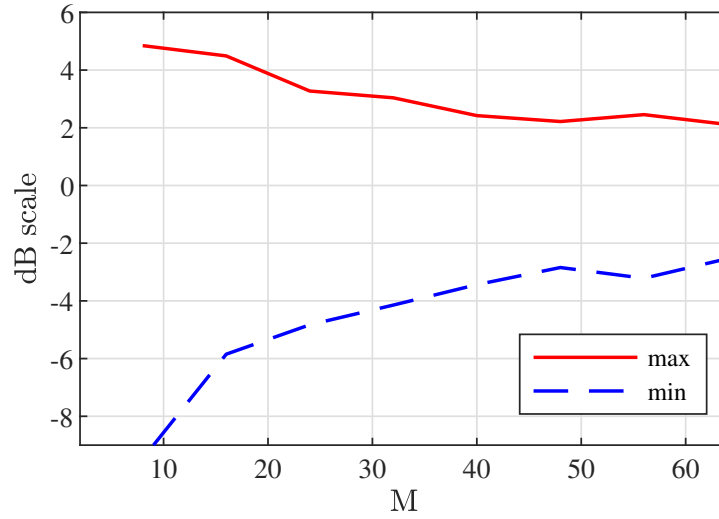
Figure 2.13: Maximum and minimum values of ratio in (2.22) for sparse array.

$M > 32$ signifying that 32 compressive measurements are sufficient to estimate $K = 4$ DoAs.
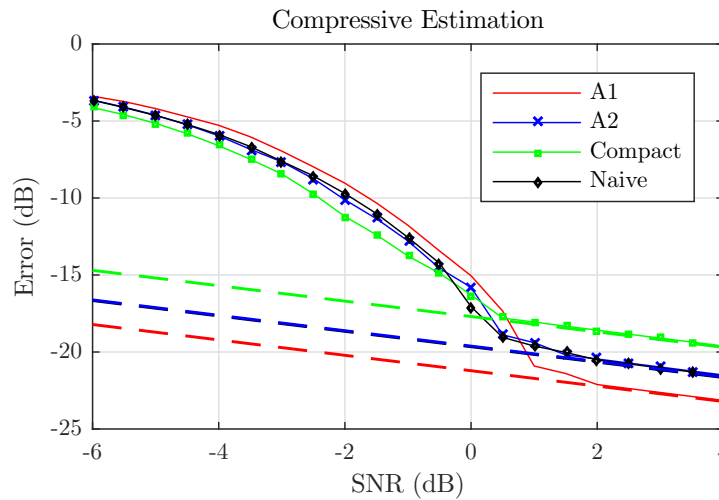
Figure 2.14: Estimation performance with Compressive measurements.

Figure 2.14 shows estimation performance with $M = 32$ compressive measurements collected across eight subarrays ($M_i = 4, i \in \{1..8\}$). Comparing with Figure 2.10, we observe that the estimation algorithms preserve the same characteristics as with full measurements with approximately 6 dB SNR penalty as expected ($N/M = 4$).

Chapter 3

Enhanced Estimation accuracy and Super-Resolution

3.1   Introduction

Recently developed super-resolution algorithms have demonstrated performance approaching fundamental estimation-theoretic bounds. These algorithms have significant potential for applications such as vehicular situational awareness using low-cost, short-range millimeter wave radar sensors. In this chapter, we show that such algorithms can approach single-sensor estimation-theoretic bounds for range and Doppler estimation. We also investigate, the limits of estimation performance of one shot estimation and investigate the feasibility of using low power sensors for short range applications.

The rest of the chapter is organized as follows. In Section 3.2, we model a single sensor and describe the FMCW range-doppler processing. In Section 3.3, we discuss how estimation algorithms, based on adaptation of recently developed super-resolution algorithms [37, 38, 36] can provide enhanced accuracy range, doppler estimates. In

---

Parts of this chapter are reprinted from our conference paper [46], ©2016 IEEE

Section 3.4, we show, via estimation-theoretic bounds, that a typical link budget for a low-cost sensor suffices to provide accurate range-Doppler estimates and provide numerical results illustrating the efficacy of the proposed estimation algorithms.

3.2   Per-Sensor Modeling and Design

3.2.1   Signal model

Each radar sensor transmits a Linear Frequency Modulated (LFM) chirp signal with frequency:

$$f(t) = f_0 + st_n$$

where $t_n = t - \left\lfloor \frac{t}{T_m} \right\rfloor$ is chirp time and $s = \frac{BW}{Tm}$ is slope of chirp (we ignore reset time between chirps). Each chirp sweeps bandwidth B over chirp ramp duration T_m and the FMCW frame containing N_{ch} such chirps. The transmitted signals across sensors are assumed to be orthogonal to others for any delay or Doppler shift, hence we can model the signals for each sensor separately [39].

The transmitted signal from any given sensor is a constant envelope signal with complex envelope $e^{j\phi(t)}$, ignoring scaling. The phase increment relative to the carrier is given by $\phi(t) = \int 2\pi f(t)dt$, where $f(t)$ denotes the instantaneous frequency. Thus, for the nth chirp, we have $f(t) = st_n$, writing $t = t_n + nT_m$ for the nth chirp, with t_n denoting "fast time" within the chirp, and n indexing "slow time" across chirps.

The downconverted received signal from K targets is given by

$$y_r(t) = \sum_{k=1}^{K} \alpha_k e^{j\phi(t-\tau_k)} e^{-2\pi f_c \tau_k} + w(t) \qquad \tau_k = \frac{2(r_k + d_k t)}{c}$$

where α_k is the complex amplitude of the reflected signal (depends on reflectivity and range [40]), r_k, d_k denote the instantaneous range and doppler of kth target, and $w(t)$ is white complex gaussian noise.

Deramping against the original chirp waveform, we obtain the beat signal

$$b^{obs}(t) = y_r(t)e^{-j\phi(t)} = \sum_{k=1}^{K} \alpha_k e^{j2\pi(-f_c\tau_k + st_n\tau_k - \frac{s\tau_k^2}{2})} + w(t) \tag{3.1}$$

Sampling at rate $1/T_s$, we obtain, after some simplifications and approximations, the discrete-time signal

$$b_{m,n} = \sum_{k=1}^{K} \alpha_k e^{j\left(\underbrace{mT_s\left(Qd_k + Pr_k\right)}_{\text{Fast time}} + \underbrace{Qd_k^k nT_m}_{\text{Slow time}}\right)} + w_{m,n} \tag{3.2}$$

where $P = \frac{4\pi s}{c}$, $Q = \frac{4\pi f_c}{c}$, $m \in \left[-\frac{N_i}{2}, \frac{N_i}{2} - 1\right]$ is fast time index, $N_i = \frac{T_m}{T_s}$, $n \in \left[-\frac{N_{ch}}{2}, \frac{N_{ch}}{2} - 1\right]$ is slow time index. (Constant phases are absorbed into the $\{\alpha_k\}$). Note that r_k, d_k correspond to range, doppler of kth target perceived at the frame center $(t = T_{frame}/2)$. We assumes an inertial trajectory within single frame which is reasonable for targeted applications and $T_f \sim 1ms$. This compensation is required to observe the enhanced accuracy of estimation algorithms while comparing against CRLB in 3.4.2.

We can now rewrite in a form that clearly brings out the roles of fast and slow time:

$$b_{m,n} = \sum_{k=1}^{K} \alpha_k e^{j\left(m\omega^f T_s + n\omega^s T_m\right)} + w_{m,n}$$

where $\omega^f = Qd_k + Pr_k$, $\omega^s = Qd_k$.

We can consolidate the samples into an observed signal matrix B:

$$B = A + W \tag{3.3}$$

$$A = \sum_{k=1}^{K} \alpha_k \begin{bmatrix} 1 & e^{j\omega_k^f T_s} & e^{j2\omega_k^f T_s} & \cdots \\ e^{j\omega_k^s T_m} & e^{j\left(\omega_k^f T_s + \omega_k^s T_m\right)} & \cdots & \vdots \\ e^{j2\omega_k^s T_m} & \vdots & \ddots & \vdots \\ \vdots & \cdots & \cdots & \ddots \end{bmatrix}$$

Standard range-Doppler estimation amounts to extracting the frequencies ω^f across rows (fast time) and ω^s across columns (slow time), typically using a 2D DFT. This is susceptible to "off-grid" effects and inter-target interference as we show in next section.

System Parameters

The FMCW system parameters used for simulation results are shown in Table 3.1.

Table 3.1: FMCW System Parameters

Carrier Frequency	$f_c = 60$ GHz
Sweep Bandwidth	$B = 0.5$ GHz
Frame Duration	$T_f = 5$ ms
IF Sampling Rate	$f_s = 0.82$ MHz

The "Rayleigh resolution" limits (which are easily surpassed by super-resolution algorithms) corresponding to these parameters are as follows [41]: range resolution $\Delta R = \frac{c}{2B} = 0.3$ m and doppler resolution $\Delta v_r = \frac{c}{2f_c T_f} = 0.5$ m/s. The maximum unambiguous range $r_{max} = N_i \Delta R = 19.2$ m and the maximum unambiguous radial velocity $d_{max} = \pm\frac{c}{4f_c T_m} = \pm 16$ m/s.

3.3   Estimation Algorithms

We first discuss algorithms for range-Doppler extraction at each sensor, and then discuss fusion across multiple sensors.

3.3.1   Per-Sensor Super-Resolution

2D-FFT: The simplest and most widely used method for extracting frequencies of the rows and columns is to perform 2-D Fourier transform on matrix B.

$$\hat{\omega}_k^s, \hat{\omega}_k^f = \mathcal{F}_{2D}(B)$$

Ideally, all targets should appear as distinct peaks with magnitude proportional to α_k on top of a constant noise floor in the 2-D spectrum. However, these estimates are constrained to the DFT grid (which can be oversampled) and therefore suffers from "off-grid" effects and inter-target interference.

Improved algorithms: Traditional frequency estimation methods such as **MUSIC** give superior performance at the cost of higher computations. A recent frequency estimation method, called Newtonized Orthogonal Matching Pursuit (NOMP), combines greedy pursuit with refinements using Newton's method [37], outperforms classical MUSIC. This algorithm has been generalized to 2D for spatial frequency estimation for 2D arrays [36]. We consider this generalization, as well as a simplification thereof, for range-Doppler estimation with multiple targets. We show that these super-resolution algorithms are far superior to the FFT, and approach estimation-theoretic bounds.

2D NOMP: The 2D-NOMP algorithm in [36] can be applied to extract frequencies (ω^f, ω^s) such that,

$$\omega^f, \omega^s = arg \min_{\omega^f, \omega^s} \left\| \mathbf{b}\text{-}\mathbf{a}(\omega^f, \omega^s) \right\|^2$$

where $\mathbf{b} = \mathbf{a} + \mathbf{w}$ is the vectorized form of Eq. 3.3. An initial coarse estimate is obtained using Interpolated 2D FFT followed by Newton refinement steps to get the final estimate.

NOMP2: The cost function to be minimized in each greedy step of 2D-NOMP can be expressed as

$$S_{2D}(g, \omega^f, \omega^s) = \left\| B_{res} - g\mathbf{u}(\omega^f)\mathbf{v}^T(\omega^s) \right\|_F^2$$

$$g, \omega^f, \omega^s = arg \max_{g, \omega^f, \omega^s} Re(g^H \mathbf{u}^H(\omega^f) B_{res} \mathbf{v}^*(\omega^s)) - \frac{1}{2} \left\| g\mathbf{u}(\omega^f)\mathbf{v}^T(\omega^s) \right\|$$

where,

$$\boldsymbol{u}(\omega) = \begin{bmatrix} 1 & e^{j\omega T_m} & \cdots & e^{j\omega(N_{ch}-1)T_m} \end{bmatrix}^T$$

$$\boldsymbol{v}(\omega) = \begin{bmatrix} 1 & e^{j\omega T_s} & \cdots & e^{j\omega(N_i-1)T_s} \end{bmatrix}^T$$

Instead of using a 2D-FFT to get an initial estimate for (ω^f, ω^s) as in 2D-NOMP, we reduce complexity in NOMP2 by employing a rank 1 SVD followed by two 1-D FFTs. The refinement Newton step remains the same (see [36] for details).

3.3.2   Range-Doppler Estimation Accuracy

Figure 3.1 shows a simulated scene containing 3 targets moving at randomly chosen range and doppler with amplitude adjusted to have equal SNR.
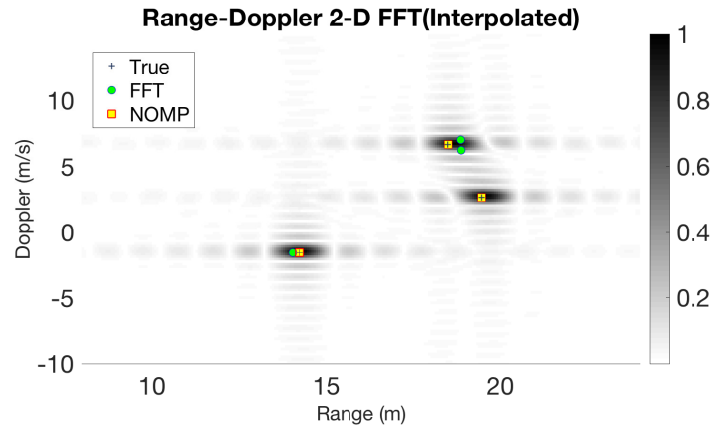
Figure 3.1: Range-Doppler response of 3 targets.

Estimation performance of both 2D NOMP and the simplified NOMP2 are similar (and are therefore not plotted separately), and are significantly better than conventional methods. The computational cost is compared in Figure 3.2: we see that NOMP2 is substantially less complex thatn 2D NOMP, while still incurring a higher cost than the standard FFT-based technique.

NOMP based super-resolution algorithms achieves higher accuracy and approaches the CRB in the operating SNR region around -10dB.
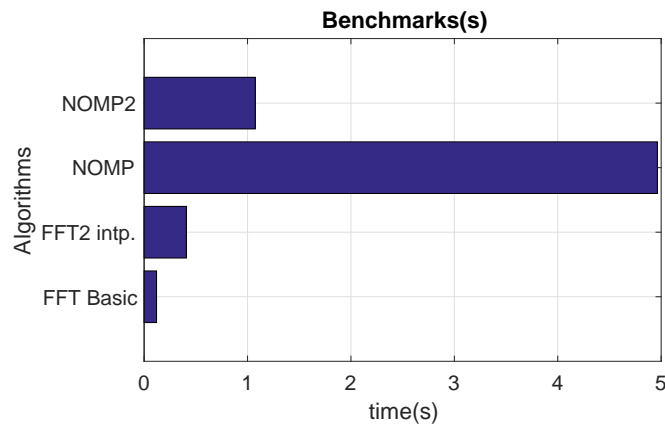
Figure 3.2: Comparison of computational cost.

3.4   Limits on Range-Doppler Estimation Accuracy

We now establish limits on the achievable performance via link budgets and estimation theoretic bounds.

3.4.1   Link budget

Our link budget calculations use studies on Radar Cross section of human targets [42], and typical low-cost 60 GHz CMOS transceiver specifications. The signal to noise ratio (SNR) for FMCW radar is calculated by [41]:

$$SNR = \frac{P_{CW}G_tG_r\lambda^2\sigma_{RCS}}{(4\pi)^3 R^4 LkTF_RB_{IF}}$$

where P_{CW} is the average transmitted power, kTF_RB_{IF} is the receiver noise power, G_t, G_r are antenna gains, R is target range, L is system loss, σ_{RCS} is the radar cross-section (RCS), and B_{IF} is the IF Bandwidth.

Considering 0 dBm transmitted power per sensor (which is easily generated at 60 GHz, for example, by CMOS power amplifiers), $B_{IF} = 1$ MHz and short ranges ($R \sim 10$ m), the operating signal to noise ratio (SNR) is above -10 dB. We now use estimation-theoretic bounds to establish that we can indeed hope to obtain satisfactory performance in this regime.

3.4.2   Estimation Theoretic lower bounds

In order to understand the best achievable localization accuracy with FMCW radar sensors, we evaluate lower bounds on the sample covariance of range-Doppler estimates. The CRB describes the error behavior at medium to high SNR when the estimate is relatively close to true value. However at low SNR, large errors occur which are not

effectively captured by CRB. This SNR threshold can be found by computing the Ziv-Zakai Bound (ZZB) [43].

Cramer-Rao Bound (CRB): The Cramér Rao Bound provides the lower bound, $Cov(\boldsymbol{\theta}_s) \geq I(\boldsymbol{\theta}_s)^{-1}$ where $I(\boldsymbol{\theta}_s)$ is Fisher Information Matrix (FIM) given by,

$$I(\boldsymbol{\theta}_s) = \mathbb{E}\left[\left(\nabla_{\boldsymbol{\theta}_s}\mathcal{L}(m_s^{obs}|\boldsymbol{\theta}_s)\right)\left(\nabla_{\boldsymbol{\theta}_s}\mathcal{L}(m_s^{obs}|\boldsymbol{\theta}_s)\right)^H\right]$$

$$I(\boldsymbol{\theta}_s) = \sum_{m,n}\frac{8\pi^2|\alpha_s^2|}{\sigma^2}\begin{bmatrix} \frac{m^2}{(N_i\delta_r)^2} & \frac{mn}{N_iN_{ch}\delta_r\delta_d} \\ \frac{mn}{N_iN_{ch}\delta_r\delta_d} & \frac{n^2}{(N_{ch}\delta_d)^2} \end{bmatrix} \tag{3.4}$$

$$= \frac{2\pi^2N_iN_{ch}|\alpha_s^2|}{3\sigma^2}\begin{bmatrix} 1/\delta_r^2 & 0 \\ 0 & 1/\delta_d^2 \end{bmatrix} \tag{3.5}$$

where $\mathcal{L}(m_s^{obs}|\boldsymbol{\theta}_s)$ is the log likelihood of the beat signal for given target range-Doppler $\boldsymbol{\theta}_s$ and reflection coefficient α_s at s^{th}sensor; m, n are fast, slow time indices such that $t = mT_s + nT_m$; $\delta_r = \frac{c}{2B}, \delta_d = \frac{c}{2f_cN_{ch}T_m}$ are the Rayleigh resolution of FMCW radar.

The result is analogous to the well known result for range-Doppler FIM in, for example ([44], §10.2).

Ziv-Zakai Bound (ZZB): CRB describes behavior of likelihood function around the true value of parameter being estimated. However, at low SNR, it is possible to make large errors in parameter estimation which are not captured by the CRB. The ZZB captures the effect of large errors at low SNR via a hypothesis testing framework, while behaving like the CRB at high SNRs. Since the quantity to be estimated is periodic in nature, we use the vector periodic bound (VPB) result from [45]. The ith diagonal

element of sample covariance matrix $\boldsymbol{C} \triangleq Cov(r, v_r)$ is bounded as,

$$C_{ii} \geq \frac{1}{2} \int_0^\pi \max_{\boldsymbol{\delta}:\delta_i=h} \{Q(\boldsymbol{\delta})\} \, hdh, \tag{3.6}$$

$$Q(\boldsymbol{\delta}) \triangleq \int_{\boldsymbol{\psi}\in\boldsymbol{\Psi}} (p_\theta(\boldsymbol{\psi}) + p_\theta(\boldsymbol{\psi} + \boldsymbol{\delta})) \, P_e(\boldsymbol{\psi}, \boldsymbol{\psi} + \boldsymbol{\delta}) d\boldsymbol{\psi} \tag{3.7}$$

where, $p_\theta(\boldsymbol{\psi})$ is the prior probability density, $P_e(\boldsymbol{\psi}, \boldsymbol{\psi} + \boldsymbol{\delta})$ is the optimal probability of error for a binary hypothesis testing problem with $H_0 = \boldsymbol{\psi}$ and $H_1 = \boldsymbol{\psi} + \boldsymbol{\delta}$. Assuming uniform prior distribution of ω^f, ω^s. The optimal error probability is computed as,

$$P_e(\boldsymbol{\psi}, \boldsymbol{\psi} + \boldsymbol{\delta}) = Q\left(\frac{\left\| A(\omega^f, \omega^s) - A(\omega^f + \delta_1, \omega^s + \delta_2) \right\|_F}{\sqrt{2}\sigma} \right)$$

where $\|.\|_F$ is Frobenius norm and $\boldsymbol{\delta} = [\delta_1, \delta_2]^T$. Plugging in A from Section 3.3 and after some manipulations,

$$P_e(\boldsymbol{\psi}, \boldsymbol{\psi} + \boldsymbol{\delta}) = Q\left(\frac{|\alpha|}{\sigma} \sqrt{ N_i N_{ch} - \left| \frac{\sin(\frac{N_i \delta_1}{2})}{\sin(\frac{\delta_1}{2})} \frac{\sin(\frac{N_{ch} \delta_2}{2})}{\sin(\frac{\delta_2}{2})} \right| } \right)$$

which is invariant to $\boldsymbol{\psi}$ and only depends on $\boldsymbol{\delta}$. So,

$$Q(\boldsymbol{\delta}) = P_e(\boldsymbol{\delta}) \int_{\boldsymbol{\psi}\in\boldsymbol{\Psi}} 2p_\theta(\boldsymbol{\psi})d\boldsymbol{\psi} = 2P_e(\boldsymbol{\delta})$$

Consider $i = 1$ case i.e. for calculating ZZB bound on ω^f

$$C_{11} \geq \frac{1}{2} \int_0^\pi \max_{\boldsymbol{\delta}:\delta_1=h} 2P_e(\boldsymbol{\delta})$$

We readily see that for fixed $\delta_1 = h$, $P_e(\boldsymbol{\delta})$ is maximum for $\delta_2 = 0$,

$$C_{11} \geq \int_0^\pi hQ \left(\frac{|\alpha|}{\sigma} \sqrt{N_i N_{ch} \left[1 - \left| \frac{\sin\left(\frac{N_i h}{2}\right)}{N_i \sin\left(\frac{h}{2}\right)} \right| \right]} \right) dh \tag{3.8}$$

Similarly with $i = 2$, we obtain ZZB bound on ω^s

$$C_{22} \geq \int_0^\pi hQ \left(\frac{|\alpha|}{\sigma} \sqrt{N_i N_{ch} \left[1 - \left| \frac{\sin\left(\frac{N_{ch} h}{2}\right)}{N_{ch} \sin\left(\frac{h}{2}\right)} \right| \right]} \right) dh \tag{3.9}$$

Estimation Accuracy

The ZZB and CRB for range estimation are computed numerically and plotted in Figure 3.3 along with NOMP estimation error. The NOMP estimation accuracy for both range and doppler achieve CRB for medium to high SNR. The ZZB threshold, defined as the SNR at which point ZZB converges to CRB indicates the low SNR region where *far* errors are present. The required transmitted signal power for location estimation can be evaluated by checking each sensor operates comfortably beyond the ZZB threshold at the maximum range of interest. The example link budget in Section 3.4.1 showed that for a human target at range $r = 10$m, a received SNR=-10 dB can be obtained using transmitted power of 0 dBm and typical hardware specifications [46]. This lies comfortably above the ZZB threshold which is around -22 dB for this case.

By using grid-less estimation algorithms such as NOMP [9], higher accuracy frequency estimate can be achieved. An additional benefit of improved frequency estimate is observed while subtracting the individual target components from beat to obtain the residual. The enhanced amplitude estimate helps to effectively cancel out individual components so that all targets are detected. We benefit from this improvement in not just localization accuracy but also in association as well as we how in next chapter. See
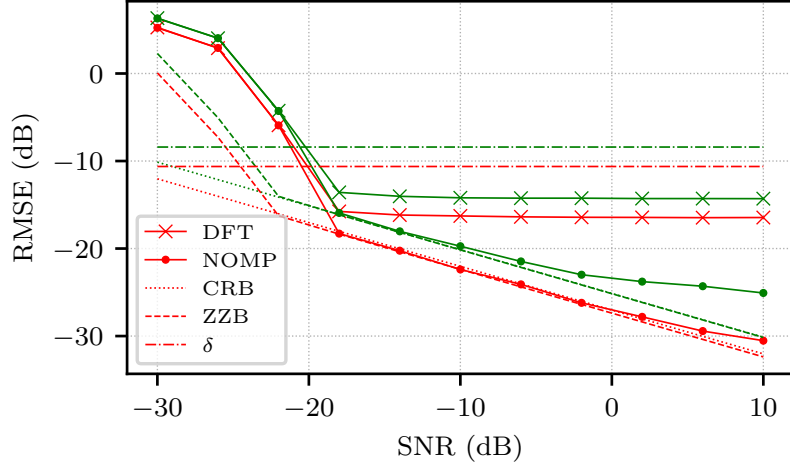
Figure 3.3: Per-Sensor range(red) & doppler(green) estimation accuracy.

Section 4.4.3 for details.

Estimation resolution analysis

Note that some targets fail to achieve CRB at high SNR, this happens specifically for targets which are very close in both range and doppler simultaneously. Since, range, doppler are extracted using 2D frequencies estimated from the beat signal, whenever two targets are closer in both dimensions they cannot be resolved. In order to understand the resolvability of multiple targets we analyze the CRB of target in presence of another target. The FIM for joint state $\boldsymbol{\theta}_s^{12} = [\boldsymbol{\theta}_s^1, \boldsymbol{\theta}_s^2]$ is given by

$$I(\boldsymbol{\theta}_s^{12}) = \mathbb{E}\left[\left(\nabla_{\boldsymbol{\theta}_s^{12}}\mathcal{L}(M_s|\boldsymbol{\theta}_s^{12})\right)\left(\nabla_{\boldsymbol{\theta}_s^{12}}\mathcal{L}(M_s|\boldsymbol{\theta}_s^{12})\right)^H\right]$$

$$= \begin{bmatrix} I_{11} & I_{12} \\ I_{21} & I_{22} \end{bmatrix}$$

Assuming reflection coefficients for both targets are equal i.e. $|\alpha_s^1| = |\alpha_s^2|$, the FIM blocks can be expressed using (3.4),

$$I_{11} = I_{22} = \frac{8\pi^2 |\alpha_s^2|}{\sigma^2} \sum_{m,n} Q_{mn} = I[\boldsymbol{\theta}_s^1]$$

$$I_{12} = I_{21} = \frac{8\pi^2 |\alpha_s^2|}{\sigma^2} \sum_{m,n} Q_{mn} e^{j2\pi \left(\frac{m\Delta r}{N_i \delta_r} + \frac{n\Delta d}{N_{ch} \delta_d} \right)} \tag{3.10}$$

where,

$$Q_{mn} = \begin{bmatrix} \frac{m^2}{(N_i \delta_r)^2} & \frac{mn}{N_i N_{ch} \delta_r \delta_d} \\ \frac{mn}{N_i N_{ch} \delta_r \delta_d} & \frac{n^2}{(N_{ch} \delta_d)^2} \end{bmatrix}$$

and $\Delta r = r_{1,s} - r_{2,s}, \Delta d = d_{1,s} - d_{2,s}$ are the separation in range and doppler perceived at sensor between the two targets. The joint CRB is the inverse of this FIM matrix,

$$Cov(\boldsymbol{\theta}_s^{12}) \geq I([\boldsymbol{\theta}_s^{12}])^{-1}$$

$$\geq I_{11}^{-1} + I_{11}^{-1} I_{12} \left(I_{22} - I_{21} I_{11}^{-1} I_{12} \right)^{-1} I_{21} I_{11}^{-1}$$

We see that in presence of target $\boldsymbol{\theta}_s^2$, an extra term gets added to the CRB corresponding to interference. Notice that as separations $\Delta r, \Delta d \to 0$, the phase shift, $\left(\frac{m\Delta r}{N_i \delta_r} + \frac{n\Delta d}{N_{ch} \delta_d} \right)$ in (3.10) vanishes and $I_{12} \to I_{11}$ resulting in larger CRB.

We first analyze the resolution of range and doppler independently assuming no separation is present in the other dimension. Fig. 3.4 shows the CRB and estimation performance as these separations are increased. The CRB increases as range/doppler separation reduces and estimation error of NOMP algorithms also follows a similar trend. However, we observe the NOMP algorithm error reduces below CRB at low separation, this is because at very low frequency separation, both target reflections merge together resulting in
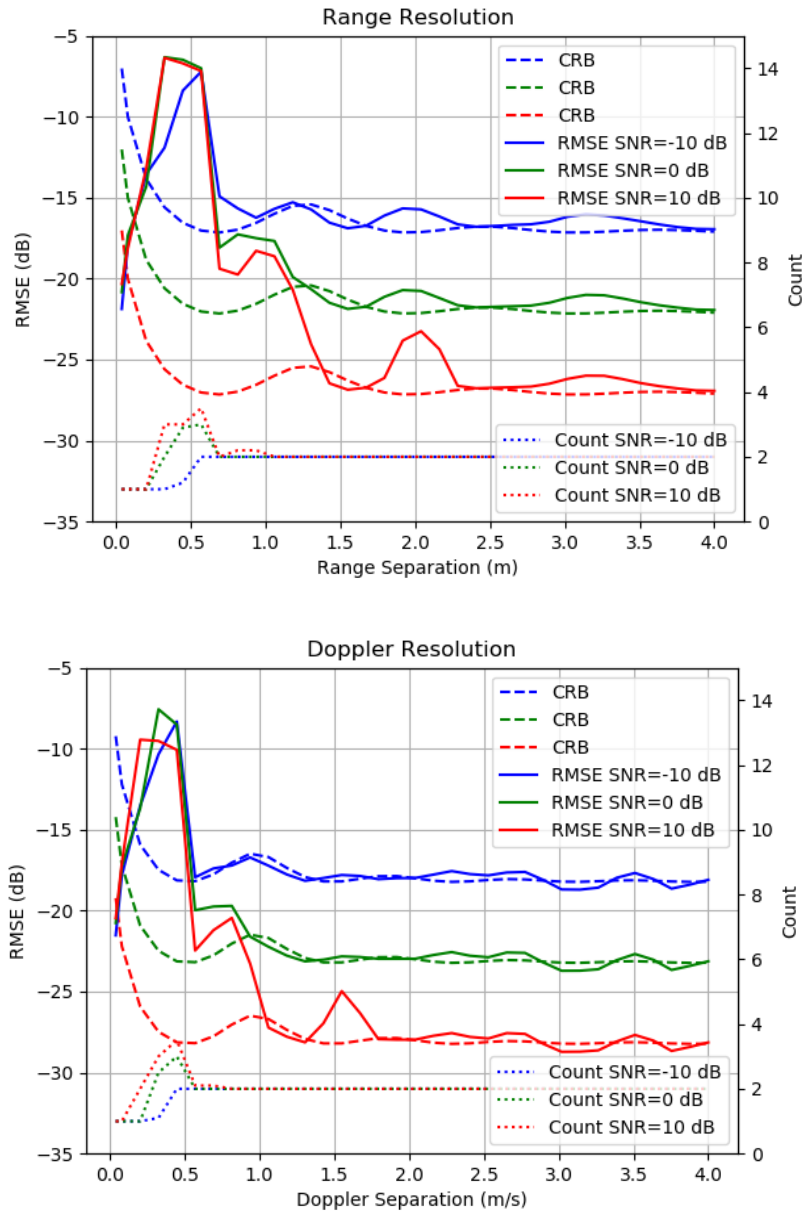
Figure 3.4: Range, Doppler resolution v/s target separation analysis with two targets.

a single target detection. The estimation error is dominated by ambiguity errors caused by this interference until it converges to CRB. The point of convergence increases with the SNR, which indicates the increasing difficulty in super-resolving closely-spaced targets due to the proximity with other targets. The estimated number of targets (dotted line) reaches correct value ($N_T = 2$) at the same point where RMSE diminishes significantly to -15 dB.
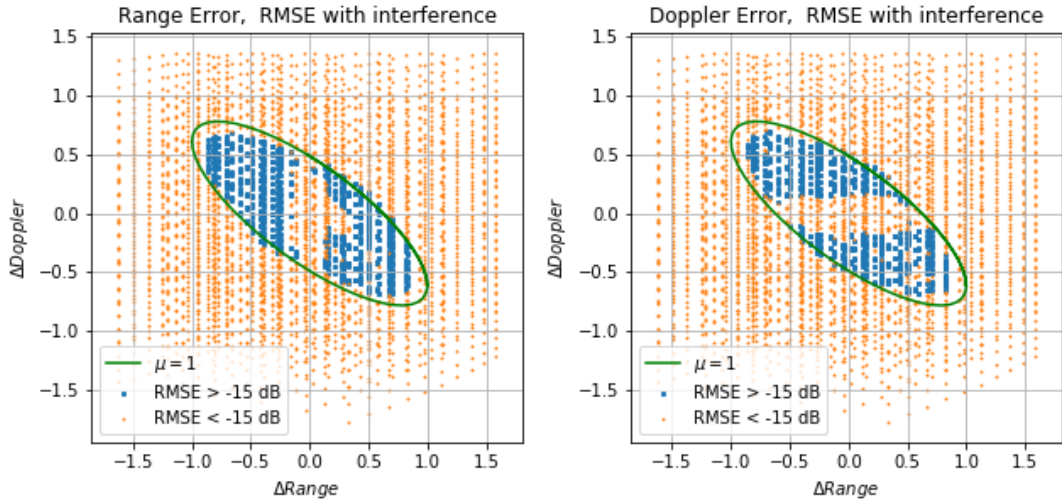
Figure 3.5: Range, Doppler resolution v/s 2D Range-Doppler separation.

When both range and doppler separation are jointly considered, a separation in either one is sufficient to resolve two targets. Fig. 3.5 shows the simulated estimation error for NOMP algorithm across various range-doppler separations at reference location $\boldsymbol{z} = [-4, 6, 1, -4]$. We observe that the estimation error exceeds the -15 dB threshold when the separation lies within an elliptical region in $\Delta r - \Delta d$ plane.

Hence, we define a minimum separation condition between the range, doppler separation of targets as follows,

$$r - r' > \delta_r \text{ OR } d - d' > \delta_d$$

We use this condition in the next chapter to distinguish scenes which suffer from such estimation errors due to range-doppler proximity

Chapter 4

Spatial Association

4.1 Introduction

In this chapter, we investigate the problem of localizing multiple targets using a single set of measurements from a network of radar sensors. Such "single snapshot imaging" provides timely situational awareness, but can utilize neither platform motion, as in synthetic aperture radar, nor track targets across time, as in Kalman filtering and its variants. This first requires correctly associating the observations collected across sensors with a unique object. Associating measurements with targets becomes a fundamental bottleneck in the single snapshot setting.

We present a computationally efficient method to extract 2D position and velocity of multiple targets using a linear array of FMCW radar sensors by identifying and exploiting inherent geometric features to drastically reduce the complexity of spatial association. The proposed framework is robust to detection anomalies, and achieves order of magnitude lower complexity compared to conventional methods. While our approach is compatible with conventional FFT-based range-Doppler processing, we show that more sophisticated techniques for range-Doppler estimation lead to reduced data association

complexity as well as higher accuracy estimates of target positions and velocities.

4.1.1   Related Work

The majority of prior work addresses temporal data association problem for tracking, relying on the temporal continuity of target state to assist in associating observations across multiple frames. While the problem of spatial association studied here has received relatively less attention, we provide a brief overview of conventional approaches in the literature that can be extended for the spatial problem.

The association problem between a pair of sensors can be optimally solved using the well-known Hungarian algorithm [47]. However, a naive approach to extend this to multiple sensor case by factorizing into pairwise (2D) association over consecutive sensors does not work well in the presence of detection anomalies such as miss, false alarm, clutter, and close-target interactions [48].

The multi-sensor association problem can be formulated as the Maximum A-Posteriori (MAP) estimation of most likely chain of observations across sensors. In order to solve this problem, a graphical model is defined, where a node represents sensor detection and an edge represents pairwise association likelihoods [49]. The association between the sensors is obtained by solving the Minimum Cost Maximum Flow (MCF) problem over this graph. A variety of methods such as Linear Programming [50], Dynamic Programming [51, 52], and push-relabel maximum flow [49] has been proposed to efficiently solve the MCF problem.

Although those methods solve the optimization in polynomial time, they require specialized mechanisms such as expansion of observation set over successive iterations to resolve detection anomalies. Moreover, the complexity of the MCF problem grows quickly as $O(N^3 \log N)$, where N is the number of sensors [49]. In comparison with

prior work, our approach reduces complexity by leveraging the high accuracy of sensor observations and their geometric properties.

Probabilistic approaches such as gated Nearest Neighbor (NN) [53] method sequentially associate sensor observations across the sensors. At each sensor, each observation is associated with its closest match to the state predicted by the chain of observations from the past sensors. However, using only single most likely observation to form association is prone to clutter and anomalies in noisy scenarios. Also, a single association error can cause significant contamination in final state estimate. This problem is well known in the literature on Simultaneous Localization and Mapping (SLAM), and various improvements such as Multiple Hypothesis Testing [54], K-best assignment [55], and JPDAF [53] have been proposed. In contrast, we propose an alternative search approach based on geometric fitting criteria which does not depend on such probabilistic models and avoids the contamination of state.

Bottom up approaches based on grid search over a set of candidate target states have been suggested in the literature [56]. In [57], an approach based on enumerating all possible candidates followed by pruning and merging shows promising results. Randomized adaptive search procedures such as random consensus sampling (RANSAC) [58], Interpretation Tree [59], Joint Compatibility Branch and Bound [60] have been shown to address the detection anomalies. The methods extract possible association chain by using branch and bound type search strategies where a heuristic technique is employed to reduce the search complexity. Our graphical approach also uses similar pruning techniques to perform the graph search, but with the additional use of geometric constraints and a geometric fitting error metric for guiding the search.

Map of this chapter

The rest of this chapter is organized as follows. In Section 4.2, we introduce the association problem in the single snapshot localization setting. Our graph association algorithm is presented in Section 4.3. Finally, we evaluated the proposed algorithm over different system parameters and provide comparisons with conventional approaches such as MCF and NN in Section 4.4.

Notation

$a, \boldsymbol{a}, A, \mathcal{A}$ represent scalar, vector, matrix and set respectively. We use [.] to construct vector, matrix and {.} to construct set. $\times, \cup, \cap$ denote the cartesian product, union and, intersection of two sets and $\varnothing$ denotes a *NULL* value. $n(\mathcal{A})$ represents the number of non-empty elements in set $\mathcal{A}$. $\circ$ denotes element-wise multiplication between vectors. A^T denotes transpose of matrix A and $\wedge$ denotes logical "and" operator.

4.2 Problem Description

4.2.1 System Model

Consider a scenario in which a linear array of N_S radar sensors locates N_T targets in a two-dimensional (2D) scene as in Figure 4.1. Without loss of generality, we assume that the sensor array located along x-axis and centered at origin is static and uses its own odometer information to obtain the absolute kinematic state of the targets.

The kinematic state (i.e., instantaneous position and velocity information of all targets) of the scene is given by

$$\mathcal{Z} = \{\boldsymbol{z}^k\}_{k=1}^{N_T}$$
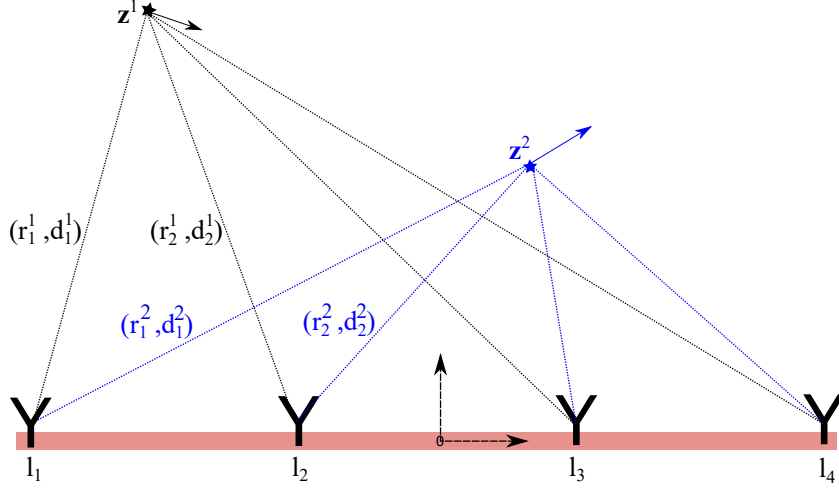
Figure 4.1: 2D System model with linear sensor array.

where $\boldsymbol{z}^k = (x^k, y^k, v_x^k, v_y^k)$ is the kinematic state of target k with an instantaneous velocity of (v_x^k, v_y^k) at position (x^k, y^k).

Due to the positioning of the sensor array, all sensors in the array perceive the same kinematic states except x-coordinate information which is given by $x - l_i$ for sensor i, where l_i is the x-coordinate of sensor i. Also, the desired kinematic state of target k, $\boldsymbol{z}^k \in \mathcal{Z}$ can be uniquely mapped to a Range-Doppler pair $\mathcal{T}_i(\boldsymbol{z}^k) = (r_i^k, d_i^k)$ by using perceived information at sensor i through the following non-linear relations,

$$r_i^k = \sqrt{(x^k - l_i)^2 + (y^k)^2}, \quad d_i^k = \frac{(x^k - l_i)v_x^k + y^k v_y^k}{r_i^k} . \tag{4.1}$$

4.2.2   Single Snapshot Localization

In order to extract range and doppler information of target k, each sensor i uses the signal (i.e., $m_i^{obs}(t)$) reflected back from the scene in monostatic mode. In this study, we focus on localization of the scene using a single snapshot. For that reason, the kinematic state of the scene is assumed to be constant for a certain time interval and the scene

65

localization is performed based on the range and doppler information gathered during that time interval. Based on those, the Maximum Likelihood Estimator (MLE) for the scene including all N_S sensors can be expressed as,

$$\hat{\mathcal{Z}}_{ML} = arg \max_{\mathcal{Z}} \prod_{i=1}^{Ns} \mathcal{L}\left(m_i^{obs} | \mathcal{T}_i(\mathcal{Z})\right) \tag{4.2}$$

where m_i^{obs} corresponds to the observed signal in a single snapshot and $\mathcal{L}\left(m_i^{obs} | \mathcal{T}_i(\mathcal{Z})\right)$ is the conditional log likelihood of the observed signal for scene $\mathcal{Z}$.

The optimization problem in (4.2) is difficult in general since the number of targets (i.e., N_T) is not known and a brute force search for $\mathcal{Z}$ incurs exponential complexity in the number of targets; that is, $n(\mathcal{D}(\boldsymbol{z}))^{N_T}$ for a grid $\mathcal{D}(\boldsymbol{z})$. In addition, the observations contain a variety of anomalies such as clutter, missed detections, and false alarms, which further complicates the solution.

In order to facilitate the solution of the problem in (4.2), the problem is divided into two stages as follows:

Estimation

The Range-Doppler pairs of $M_i < N_T$ non-occluded targets are estimated from received signal m_i^{obs} at sensor i using efficient algorithms proposed in the literature [46]. The estimate at sensor i for k^{th} target can be modeled as follows,

$$(r_i^k) = (r_i^k)^{true} + w_i^R + \tilde{b}_i^k, \tag{4.3a}$$

$$(d_i^k) = (d_i^k)^{true} + w_i^D + \bar{b}_i^k \tag{4.3b}$$

where $w_i^R \sim \mathcal{N}(0, \sigma_{r_i}^2)$ and $w_i^D \sim \mathcal{N}(0, \sigma_{d_i}^2)$ denote independent Gaussian distributed noises with zero mean and $\tilde{b}_i^k$ and $\bar{b}_i^k$ denote the bias errors introduced due to proximity

with any other $M_i - 1$ targets in the scene. The noise variance depends on estimation accuracy at the given SNR which, in turn, depends on target radar cross section (RCS), path loss, and antenna directivity. For simplicity, we assume equal received signal power across all targets in the scene.

We denote the set of estimated range-doppler pairs at sensor i by $\Theta_i = \{\bigcup_{k=1}^{M_i} \boldsymbol{\theta}_i^k\}$ where $\boldsymbol{\theta}_i^k = \left[(r_i^j), (d_i^j)\right]^T$. It is important to note that the superscript of estimated range-doppler pairs $\boldsymbol{\theta}_i^k$ is different from the true target index since we do not know the true target index that the observation at the sensor belongs to.

Association problem

The estimation of kinematic state $\mathcal{Z}$ requires the association of those un-ordered range doppler pairs, Θ_i, collected across all sensors. An association chain is defined as the ordered set of range doppler observations, $\mathcal{A} : \{\{\boldsymbol{\theta}_i\}_{i=1}^{N_S} | \boldsymbol{\theta}_i \in \tilde{\Theta}_i\}$ which is constructed from the *NULL* augmented sets; that is, $\tilde{\Theta}_i = \Theta_i \cup \varnothing$. $\boldsymbol{\theta}_i = \varnothing$ corresponds to the *NULL* state and represents the occurrence of missed detection at sensor i.

The spatial association problem can be formulated as the following maximum a posteriori (MAP) estimation problem,

$$\boldsymbol{\mathcal{A}}^* = \underset{\boldsymbol{\mathcal{A}} \subset \tilde{\Theta}_1 \times \cdots \times \tilde{\Theta}_{N_S}}{\operatorname{argmax}} \log P(\boldsymbol{\mathcal{A}})P(\Theta|\boldsymbol{\mathcal{A}}) \tag{4.4}$$

$$\text{such that} \quad \mathcal{A}^i \cap \mathcal{A}^j = \varnothing \quad \forall i \neq j, \quad n(\mathcal{A}^k) \geq 2$$

where $\Theta = \bigcup_{i=1}^{N_S} \Theta_i$ denotes the set of all range-doppler observations, $\boldsymbol{\mathcal{A}} = \{\mathcal{A}^1, \mathcal{A}^2, \cdots\}$ denotes a subset of association chains chosen from the set of all possible potential chains, $\tilde{\Theta}_1 \times \tilde{\Theta}_2 \times \cdots \tilde{\Theta}_{N_S}$. The optimal solution $\boldsymbol{\mathcal{A}}^*$ consists of the set of chains which jointly maximizes overall log likelihood while the constraints ensure that no two chains share a

common observation and each chain contains at least two observations.

When the targets are well-separated, the bias terms in (4.3a) and (4.3b) vanish and the likelihood for the individual targets becomes independent across multiple targets. In this case, the log likelihood in (4.4) simplifies to,

$$\log P(\boldsymbol{\mathcal{A}})P(\Theta|\boldsymbol{\mathcal{A}}) = \sum_{\mathcal{A}\in\boldsymbol{\mathcal{A}}} \log P(\mathcal{A}) + \log P(\Theta|\mathcal{A})$$

where $P(\Theta|\mathcal{A}) = \prod_{i=1}^{N_S} P(\Theta_i|\mathcal{A})$ is the probability of detecting the range-doppler pairs which can be modeled by a Bernoulli distribution,

$$P(\Theta_i|\mathcal{A}) = \begin{cases} \alpha & \text{, if target missed at sensor } i\,, \mathcal{A}_i = \varnothing \\ 1 - \alpha & \text{, else} \end{cases}$$

where α denotes the probability of detection errors in (4.5) and is set to nominal value $\alpha = 0.05$ [49]. This model accounts for the occurrence of both miss and false alarms across the sensors in the likelihood, which is given by,

$$P(\Theta|\mathcal{A}) = \alpha^{N_S-n(\mathcal{A})}(1-\alpha)^{n(\mathcal{A})}$$

Also, $P(\mathcal{A})$ is the likelihood of chain modeled using the perceived range-doppler pairs, $(\hat{r}_i, \hat{d}_i) = \mathcal{T}_i(\hat{\boldsymbol{z}})$ for a target state $\hat{\boldsymbol{z}}_k$ predicted by the chain (see Section 4.3.2). By ignoring the constant terms which preserve the MAP solution, we define the normalized negative

log likelihood as follows,

$$\mathcal{L}(\mathcal{A}) = \sum_{\boldsymbol{\theta}_i \in \mathcal{A}} \left(\frac{(\hat{r}_i - r_i)^2}{\sigma_r^2} + \frac{(\hat{d}_i - d_i)^2}{\sigma_d^2} \right)$$
$$+ \, n(\mathcal{A}) \log \frac{\alpha}{1 - \alpha} \tag{4.5}$$

where $\boldsymbol{\theta}_i = [r_i, d_i]^T$ is the observation from i^{th} sensor in the association chain $\mathcal{A}$ and σ_r^2 and σ_d^2 are the nominal variance terms for range and doppler, respectively. These values are set based on the value of CRB at nominal $SNR = -20$ dB; that is, $\sigma_{r_i}^2 = \delta_r^2/(\kappa SNR)$ and $\sigma_{d_i}^2 = \delta_d^2/(\kappa SNR)$ (see Section 3.4.2 for details). The first term in (4.5) denotes the squared error between the estimated and observed range-doppler pairs in the chain while the second term penalizes the selection of smaller chains which prevents formation of duplicate chains for the same target. Hence, the association problem is reduced to the following constrained minimization problem,

$$\boldsymbol{\mathcal{A}}^* = \operatorname*{argmin}_{\boldsymbol{\mathcal{A}} \subset \tilde{\Theta}_1 \times \cdots \times \tilde{\Theta}_{N_S}} \sum_{\mathcal{A} \in \boldsymbol{\mathcal{A}}} \mathcal{L}(\mathcal{A}) \tag{4.6}$$
$$\text{such that} \quad \mathcal{A}^i \cap \mathcal{A}^j = \varnothing \; \forall i \neq j, \quad n(\mathcal{A}) \geq 2$$

The joint minimization problem over all potential association chains in (4.6) is difficult in general. For that reason, we use an iterative approach where the most likely chains of observations are identified and removed from observation set Θ sequentially,

$$\operatorname*{argmin}_{\mathcal{A} \in \tilde{\Theta}_1 \times \cdots \times \tilde{\Theta}_{N_S}} \mathcal{L}(\mathcal{A}) \quad \text{such that} \quad n(\mathcal{A}) \geq 2 \,. \tag{4.7}$$

Without any prior knowledge of association between the nodes, the number of potential chains $\Theta_1 \times \Theta_2 \times \cdots \Theta_{N_S}$ still grows exponentially. However, the formulation in (4.7)

69

enables the utilization of various network optimization methods to identify the most likely chain. Once the associated chains of range-doppler observations are found across sensors, the kinematic state of the scene can be easily obtained by solving the inverse kinematic problem $[\hat{x}, \hat{y}, \hat{v}_x, \hat{v}_y] = \mathcal{T}^{-1}(\mathcal{A})$ using Gauss-Newton algorithm [46].

4.3 Graphical Association

In order to solve the association problem in (4.7), we formulate the spatial association problem using graphical models and present our low-complexity graphical search method to obtain association chains efficiently via geometric relations.

4.3.1 Graph Generation
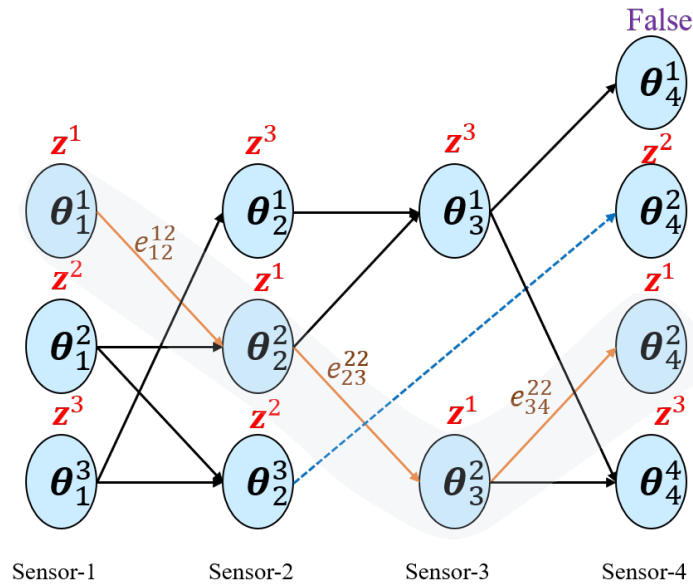
Figure 4.2: Target-based observation graph for a scene with 3 targets and 4 sensors. Sensors $1, 2$ observe all 3 targets in different orders. Sensor 3 misses the observation of target state z^2 while sensor 4 contains a false observation. Desired association chain, $\mathcal{A}$ is shown by the shaded set of nodes.

70

To begin with, we define a target-based graph to perform data association with following elements:

- Node $\boldsymbol{\theta}_i^k$ represents the kth range-doppler pair at sensor i. Nodes for a given sensor are arranged along a single column of the graph as shown in Figure 4.2.

- Edge $e_{ij}^{kl} = [\boldsymbol{\theta}_i^k, \boldsymbol{\theta}_j^l]$ denotes the linkage between pairs of observation across sensor i and sensor j, which can correspond to a feasible target $\boldsymbol{z}_{ij}^{kl}$ referred to as "*Phantom*".

- Chain $\mathcal{A}^j$ is represented by the sequence of two or more nodes spanning distinct sensors, which is associated to a single target, $\hat{\boldsymbol{z}}^j$.

Geometric Constraints A significant portion of the edges can be easily discarded in the graph generation phase by using the following geometric constraint on target's range (for noiseless case),

$$C_{\mathrm{G}}(e_{ij}): \quad (r_i - r_j < l_{ij}) \wedge (r_i + r_j > l_{ij}) \tag{4.8}$$

where $l_{ij} = |l_i - l_j|$ represents the separation between sensor i and sensor j.

The graph $\mathcal{G} = (\mathcal{V}, \mathcal{E})$ is initialized with vertices for all Range-doppler pairs $\mathcal{V} = \{\Theta_i\}_{i=1}^{N_S}$ and edges $\mathcal{E}$ between any two consecutive nodes that satisfy condition $C_{\mathrm{G}}(e_{i-1,i}^{k,l}), \forall k \in [1, M_{i-1}], \forall l \in [1, M_i]$ for all $i \in \{2, \ldots, N_S\}$ given in (4.8).

4.3.2 Spatial Association using Geometric Features

In this subsection, we describe the solution of association problem presented in (4.7) using the graph $\mathcal{G}$ by exploiting geometric relations between range, Doppler, and sensor geometry. For clarity of exposition, we focus on the association procedure of a single target $\boldsymbol{z} = [x, y, v_x, v_y]$ and, therefore, drop the superscript k for the sake of simplicity.

Geometric Relations

The range of target observed at i^{th} sensor is given by

$$r_i = \sqrt{(x - l_i)^2 + (y)^2} \tag{4.9}$$

The Doppler component is the rate of change of range and it is given by,

$$d_i = \dot{r}_i = \frac{(x - l_i)v_x + yv_y}{r_i}$$

$$r_i d_i = (x - l_i)(v_x) + yv_y \tag{4.10}$$

For a linear array of sensors, the range and doppler measurements for a target satisfy the following relations based on (4.9) and (4.10):

$$r_i^2 = r_j^2 - 2x(l_i - l_j) + (l_i^2 - l_j^2) \tag{4.11a}$$

$$r_i d_i = r_j d_j - (v_x)(l_i - l_j) \tag{4.11b}$$

where r_i (r_j) and d_i (d_j) are the range and doppler estimated at the ith (j^{th}) sensor, respectively. l_i (l_j) is the x-coordinate of ith (j^{th}) sensor. (4.9) and (4.10) indicate that for the noiseless setting, the range-doppler products and range squared are linear with respect to target's velocity and position at x-coordinate, respectively. Therefore, the correct associations can be identified by fitting the observations to those geometric relations.

State Prediction and Fitting Error

The presence of noise in (r_i, d_i) causes high error in these geometric relations due to the quadratic dependence. An estimate of target state parameters $\hat{x}, \hat{v}_x$ can be obtained by

72

minimizing that error between observed and predicted range and doppler values. Let $\boldsymbol{q}_1 = [r_i d_i | (r_i, d_i) \in \mathcal{A}]$ and $\boldsymbol{l} = [l_i | \boldsymbol{\theta}_i \in \mathcal{A}]$ denote the vector of range-doppler products using observations in chain $\mathcal{A}$ and the vector of corresponding sensor x-coordinates respectively. Predicted fit $\hat{\boldsymbol{q}}_1$ can be expressed using the geometric relation in (4.11b) as follows:

$$\hat{\boldsymbol{q}}_1 = -v_x \boldsymbol{l} + \kappa_1 \mathbb{1} = H \boldsymbol{s}_1$$

where $H = [\boldsymbol{l}, \mathbb{1}]$, $\boldsymbol{s}_1 = [-v_x \ \kappa_1]^T$, and κ_1 is a constant. Then, the least squares estimate for $\hat{\boldsymbol{s}}_1$ is obtained as

$$
\begin{aligned}
\hat{\boldsymbol{s}}_1 &= arg \min_{\boldsymbol{s}_1} \quad \|\boldsymbol{q}_1 - H\boldsymbol{s}_1\|^2 \\
&= (H^T H)^{-1} H^T \boldsymbol{q}_1 \, .
\end{aligned}
\tag{4.12}
$$

Therefore, the least square estimate is obtained as $\hat{v}_x = \boldsymbol{u}^T \boldsymbol{q}_1$ where $\boldsymbol{u} = -H(H^T H)^{-1} \boldsymbol{e}_1$ and $\boldsymbol{e}_1 = [1, 0]^T$.

Similarly, let $\boldsymbol{q}_2 = [r_i^2 | (r_i, d_i) \in \mathcal{A}]$ denote the vector of range squared observations in chain $\mathcal{A}$, predicted fit $\hat{\boldsymbol{q}}_2$ can be expressed using the geometric relation in (4.11a) as follows:

$$\hat{\boldsymbol{q}}_2 - \boldsymbol{l} \circ \boldsymbol{l} = -2x \boldsymbol{l} + \kappa_2 \mathbb{1} = H \boldsymbol{s}_2$$

where $\boldsymbol{s}_2 = [-2x \ \kappa_2]^T$ and κ_2 is a constant. The least squares estimate of $\hat{x}$ is obtained as

$$
\begin{aligned}
\hat{\boldsymbol{s}}_2 &= arg \min_{\boldsymbol{s}_2} \quad \|\boldsymbol{q}_2 - \boldsymbol{l} \circ \boldsymbol{l} - H\boldsymbol{s}_2\|^2 \\
&= (H^T H)^{-1} H^T (\boldsymbol{q}_2 - \boldsymbol{l} \circ \boldsymbol{l}) \, .
\end{aligned}
\tag{4.13}
$$

Hence, we obtain $\hat{x} = \boldsymbol{u}^T(\boldsymbol{q}_2 - \boldsymbol{l} \circ \boldsymbol{l})/2$.

The remaining state parameters (i.e., y and v_y) are obtained using the geometric relations in (4.9) and (4.10) as

$$\hat{y} = \sqrt{\frac{1}{n(\mathcal{A})} \sum_{\boldsymbol{\theta}_i \in \mathcal{A}} \left(r_i^2 - (\hat{x} - l_i)^2\right)},$$

$$\hat{v}_y = \frac{1}{n(\mathcal{A})} \sum_{\boldsymbol{\theta}_i \in \mathcal{A}} \frac{r_i d_i - (\hat{x} - l_i)\hat{v}_x}{\hat{y}}.$$

The normalized geometric fitting error of a chain $\mathcal{A}$ can be computed using these estimates as follows:

$$F(\mathcal{A}) = \frac{\left\|\boldsymbol{q}_1 - \hat{\boldsymbol{q}}_1\right\|^2}{\eta_1} + \frac{\left\|\boldsymbol{q}_2 - \hat{\boldsymbol{q}}_2\right\|^2}{\eta_2} \tag{4.14}$$

$$= \frac{\left\|\left(I - H(H^T H)^{-1} H^T\right)\boldsymbol{q}_1\right\|^2}{\eta_1} \tag{4.15}$$

$$+ \frac{\left\|\left(I - H^T(H^T H)^{-1} H\right)(\boldsymbol{q}_2 - \boldsymbol{l} \circ \boldsymbol{l})\right\|^2}{\eta_2}$$

where η_1 and η_2 are normalization constants that are set based on CRB (see Appendix B.1 for details) and (4.15) is obtained by substituting the predicted fits into (4.14). It is important to note that the error in (4.15) is additive over the observations in chain $\mathcal{A}$. Therefore, the extension of the chain cannot reduce the fitting error. In other words, $F(\mathcal{A})$ is monotonically non-decreasing over the length of chain $\mathcal{A}$. For that reason, the fitting error provides a simple measure of the geometric consistency of a chain, which can be used to traverse the graph and extract the chains efficiently.

Geometric Association

We now present a graph search procedure which obtains the associated chains by minimizing geometric fitting error $F(\mathcal{A})$ in (4.15) and negative log likelihood $\mathcal{L}(\mathcal{A})$ in

(4.5). We apply the geometric relations by adding constraints on the desired chain, $\mathcal{A}$ to the optimization problem in (4.7) as follows,

$$\min_{\mathcal{A} \in \tilde{\Theta}_1 \times \cdots \times \tilde{\Theta}_{N_s}} \mathcal{L}(\mathcal{A})$$

$$\text{such that} \quad n(\mathcal{A}) \geq \gamma, \tag{4.16a}$$

$$F(\mathcal{A}) < \tau_f^{n(\mathcal{A})} \tag{4.16b}$$

The constraint in (4.16a) restricts the number of missed observations to be less than $N_s - \gamma$ and the constraint in (4.16b) only allows chains with good geometric fit to be selected. In order to provide a solution for the optimization problem in (4.16), we perform Depth First Search (DFS) over the graph generated in Section 4.3.1 to extract the chains, where those additional constraints help in reducing the search complexity. Our complete Spatial Association using Geometry Algorithm (SAGA) is outlined in Algorithm 3. Here is a brief description:

1. We start the graph search by setting $\gamma = N_s$ so that only chains that include observations from all sensors are extracted. For that reason, we consider a graph having edges between consecutive sensors only. This helps to reduce the chains encountered during initial DFS procedure (see Appendix B.2 for details).

2. The DFS is guided by geometric fitting error $F(\mathcal{A})$. After each node is visited, the fitting error of candidate chain is calculated and the chain is ignored if it has a fitting error higher than predefined threshold $\tau_f^{N_s}$. Since the fitting error is non-decreasing over the length of the chain, most of the candidate chains are eliminated before reaching at the end of the graph, which reduces the complexity further. Details of DFS are shown in Appendix B.3. At the termination of the DFS, the corresponding chain of nodes is added to solution $\mathcal{A}^{\dagger}$ if it satisfies all

the constraints in (4.16) and the negative log-likelihood of the association chain is below a predefined threshold (i.e., $\mathcal{L}(\mathcal{A}) < \tau_l^{n(\mathcal{A})}$). The nodes belonging to the selected chains are removed from the graph together with their corresponding edges to keep subsequent chains disjoint.

3. In order to deal with missed detection cases at sensors, the minimum chain length constraint (i.e., γ) is relaxed in steps upto robustness level ρ. Due to that relaxation, the graph includes not only the edges between consecutive sensors but also the edges among the nodes that skip over h consecutive sensors. Those edges are called *Skip-h* edges where $h = N_S - \gamma$. Then, the DFS procedure is repeated for different minimum chain length constraints. Consequently, in this procedure, *NULL* states are taken into account and the generated chain does not include any observation from a sensor that misses the corresponding target by skipping over the observations of sensor via *Skip-h* edges. In addition, the DFS procedure implicitly accounts for *NULL* state in the beginning and end of a chain by starting searching from different nodes in consideration of minimum chain length constraint.

4. The thresholds (i.e., τ_f and τ_l) for the geometric fitting error and the likelihood depend on length of the chain $n(\mathcal{A})$ and their initial value is set based on CFAR criteria (see Appendix B.1 for details). Using a tight initial threshold τ_f for $F(\mathcal{A})$ restricts the number of branches to be explored at each node to a smaller set. This reduces the initial complexity of DFS while allowing only a subset of association chains $\mathcal{A}^\dagger \subset \mathcal{A}^*$ to be found. The thresholds are later relaxed by a factor of $\beta > 1$ to allow the observations contaminated with noise to be selected. The relaxation is stopped when no further chains with length $n(\mathcal{A}) \geq N_s - \rho$ exist in the graph.

Robustness: During the chain length relaxation, a *Skip* edge is added between the observations across sensor i and sensor q if

---

Algorithm 3 Spatial Association using Geometric Assistance

1: **Input:** Graph $\mathcal{G}$, Robustness level ρ
2: Initialize Chains $\boldsymbol{\mathcal{A}}^{\dagger} = \emptyset, \boldsymbol{\tau} = [\tau_f, \tau_l]_{init}$
3: **Repeat**
4: Remove all Skip edges
5: **for** $h = 0$ to ρ **do**
6:    Set minimum chain length: $\gamma = N_s - h$
7:    Add Skip-h edges to graph $\mathcal{G}$
8:    **for** $v \in \mathcal{V}$ **do**
9:      DFS from node v: $\mathcal{A} \leftarrow$ *GA-DFS*$(v, \gamma, \boldsymbol{\tau})$
10:      **if** Valid Chain, $\mathcal{A}$ is found **then**
11:        $\boldsymbol{\mathcal{A}}^{\dagger} \leftarrow \mathcal{A}$
12:        Remove chain from graph $\mathcal{V} = \mathcal{V} - \{\mathcal{A}\}$
13:      **end if**
14:    **end for**
15: **end for**
16: Relax thresholds: $\boldsymbol{\tau} \leftarrow \beta\tau$
17: **Until** Chains with length $n(\mathcal{A}) \geq N_s - \rho$ exists in $\mathcal{G}$
18: **Output:** Selected chains $\boldsymbol{\mathcal{A}}^{\dagger}$

---

1. Observations $\boldsymbol{\theta}_i$ and $\boldsymbol{\theta}_q$ satisfy the geometric constraint $C_\text{G}(e_{iq})$ in (B.2), and,

2. The target state predicted by $\boldsymbol{\theta}_i$ and $\boldsymbol{\theta}_q$ differs by a predefined threshold τ_z from the ones predicted by using all observations on the paths that connect $\boldsymbol{\theta}_i$ and $\boldsymbol{\theta}_q$.

$$C_\text{S}(e_{iq}): \quad \left\| \hat{\boldsymbol{z}}_{\mathcal{A}_p} - \hat{\boldsymbol{z}}_{iq} \right\| > \tau_z, \forall \mathcal{A}_p : \{\boldsymbol{\theta}_i, \boldsymbol{\theta}_q\} \in \mathcal{A}_p \tag{4.17}$$

where $\mathcal{A}_p$ is in the form of $\mathcal{A}_p = \{\boldsymbol{\theta}_i, \boldsymbol{\theta}_j, \cdots, \boldsymbol{\theta}_q\}$ with $\boldsymbol{\theta}_i$ and $\boldsymbol{\theta}_q$ at the edges of the path, $\hat{\boldsymbol{z}}_{iq}$ indicates the predicted target state based on $\boldsymbol{\theta}_i$ and $\boldsymbol{\theta}_q$, and $\hat{\boldsymbol{z}}_{\mathcal{A}_p}$ shows the predicted target state using the observations in $\mathcal{A}_p$.

Enforcing the condition in (4.17) avoids the formation of multiple chains corresponding to the same target and avoids unnecessary increase in the number of edges. The amount of skip connections introduced in the graph is controlled by the robustness level; that is, $0 \leq \rho \leq (N_s - 2)$, which sets the maximum number of missed detections that can be

tolerated across the sensor array. In this way, addition of such edges provides a flexible mechanism to provide robustness against missed detection in the sensors while keeping search space in control.

Complexity: The non-decreasing property of $F(\mathcal{A})$ is used to discard unlikely chains in the early stages of DFS. This allows for rapid extraction of associations from graph without requiring search over all possible chains in the graph. The minimum track length threshold, γ is reset to maximum value after each relaxation. Therefore, the skip edges in the graph can be removed at the end of inner loop to reduce search complexity further. Therefore, our approach exploits the geometric structure of observations across multiple sensors to reduce search complexity. However, in the absence of such structure (e.g., a scenario including only low-accuracy range-doppler observations), our algorithm visits all edges in graph. For that reason, it is difficult to calculate the complexity of the proposed algorithm since we discard branches at the nodes based on the geometric relationships between the observations. We, therefore, evaluate the relative complexity of our approach against other methods via simulations in Section 4.4.2.

4.3.3   Brute force Association

Before evaluating the performance of our main algorithm, we describe an iterative Brute force search method, which relies on the fact that an approximate kinematic state estimate can be derived by using two connected observations in a graph. In other words, a state estimate can be obtained for each edge in a graph, which is a part of the association chain $\mathcal{A}$. Therefore, the search space for the association problem in (4.7) can be reduced to the set of edges.

The likelihood of a phantom $\boldsymbol{z}_e$ corresponding to an edge $e \in \mathcal{E}$ can be computed as,

$$\mathcal{L}(\boldsymbol{z}_e) = \sum_{i=1}^{N_s} \left[\min_{\boldsymbol{\theta} \in \Theta_i} \left(\frac{(r_i' - r_i)^2}{\sigma_r^2} + \frac{(d_i' - d_i)^2}{\sigma_d^2} \right) \right] \tag{4.18}$$

where $[r_i', d_i'] = \mathcal{T}_i(\boldsymbol{z}_e)$ is the perceived range and doppler at sensor i for target state $\boldsymbol{z}_e$. Then, the most likely phantom can be selected by evaluating (4.18) over all edges and choosing the one that achieves the minimum negative log likelihood; that is, $\boldsymbol{z}^* = \boldsymbol{z}_{e^*}$ for $e^* = arg \min_{e \in \mathcal{E}} \mathcal{L}(\boldsymbol{z}_e)$. Then, the observations associated with $\boldsymbol{z}^*$ can be identified via the following neighborhood constraint:

$$\mathcal{N}(\boldsymbol{z}^*) = \bigcup_{i=1}^{N_s} \{(r_i, d_i) | (r_i - r_i^*) \le \delta_r \wedge (d_i - d_i^*) \le \delta_d\}$$

where $[r_i^*, d_i^*] = \mathcal{T}_i(\boldsymbol{z}^*)$ are the perceived range-doppler at sensor i and δ_r and δ_d are the range and doppler resolution parameters defined in Section 3.4.2. The algorithm carrying out this procedure is presented in Algorithm 4.

Algorithm 4 Brute force Spatial Association

1: INITIALIZE GRAPH WITH OBSERVATIONS Θ: $\mathcal{G} = (\mathcal{V}, \mathcal{E})$
2: AUGMENT GRAPH with skip edges
3: **for** $h = 0$ to ρ **do**
4:    ADD SKIP-h EDGES TO GRAPH $\mathcal{G}$
5: **end for**
6: INITIALIZE $\mathcal{Z} = \emptyset$
7: **while** $\mathcal{E} \neq \emptyset$ **do**
8:    FIND MOST LIKELY PHANTOM, $\mathcal{Z} \leftarrow \boldsymbol{z}^*$ from edge $\boldsymbol{z}^* = arg \min_{e \in \mathcal{E}} \mathcal{L}(\boldsymbol{z}_e)$
9:    REMOVE ALL VERTICES EXPLAINED BY $\boldsymbol{z}^*$, $\mathcal{V} \leftarrow \mathcal{V} - \mathcal{N}(\boldsymbol{z}^*)$
10:    UPDATE EDGES $\mathcal{E}$
11: **end while**
12: RETURN Selected phantoms $\mathcal{Z}$

Since all edges in the graph are checked while selecting the phantoms, this approach exhibits higher complexity than our proposed algorithm. Moreover, evaluation of state

likelihood $\mathcal{L}(\boldsymbol{z}_e)$ in (4.18) is more expensive than evaluation of chain likelihood $\mathcal{L}(\mathcal{A})$ in (4.5) as it involves a minimization over all other observations. We use this algorithm as a benchmark against our proposed algorithm in Section 4.4.

4.4   Simulation Results

In this section, we evaluate the performance of the proposed spatial association algorithm, $SAGA$ against the brute force search algorithm through various performance metrics. We consider a linear array of N_S FMCW radar sensors each of which collects range and doppler observations from the scene. The FMCW radar system parameters are set based on the ones that are used in typical low cost automotive systems at mm-Wave frequencies [61] where range and doppler resolutions are $\delta_r = 0.3\,\mathrm{m}$ and $\delta_d = 0.5\,\mathrm{m/s}$ respectively. In the simulations, a single snapshot of the scene is considered with multiple targets having equal received SNR at all sensors. The kinematic states of targets are randomly selected based on uniform distributions $x \sim \mathcal{U}(-8m, 8m), y \sim \mathcal{U}(2m, 12m), v_x \sim \mathcal{U}(-10m/s, 10m/s), v_y \sim \mathcal{U}(-10m/s, 10m/s)$.

It is important to note that when range and doppler separation between two targets gets small, the estimation algorithm either provides a merged estimate or results in detection anomalies such as miss and false alarm. In order to differentiate the scenes with such estimation errors due to range-doppler proximity, we consider two different scenarios with two different scenes. The *well-separated* scene is generated by enforcing a minimum separation between the range and doppler of the targets at all sensors. The *adverse* scene does not have such constraints and contains additional missed detection anomalies by randomly removing measurements from the sensors with probability P_{miss}. Unless stated otherwise, the nominal values of system parameters are presented in Table 4.1.

Table 4.1: Simulation Parameters

Number of targets	$N_T = 20$
Number of radar sensors	$N_s = 6$
SNR	-10 dB
Sensor Array Width	$L_w = 4$ m
Max range, doppler	19.2 m, ± 16 m/s
Simulated misses	$P_{miss} = 0.05$
Robustness Level	$\rho = 4$

4.4.1 Localization Accuracy

In this subsection, we analyze the localization accuracy of kinematic state estimates obtained using associated sensor observations. This depends on the accuracy of underlying range-doppler estimates. The position and velocity estimation errors for state estimates $\hat{\boldsymbol{\mathcal{Z}}}$ are computed as follows:

$$D_p(\hat{\boldsymbol{\mathcal{Z}}}) = \frac{1}{n(\hat{\boldsymbol{\mathcal{Z}}})} \sum_{\hat{\boldsymbol{z}} \in \hat{\boldsymbol{\mathcal{Z}}}} \min_{\boldsymbol{z} \in \boldsymbol{\mathcal{Z}}^{\text{true}}} d_p(\boldsymbol{z}, \hat{\boldsymbol{z}})^2$$

$$D_v(\hat{\boldsymbol{\mathcal{Z}}}) = \frac{1}{n(\hat{\boldsymbol{\mathcal{Z}}})} \sum_{\hat{\boldsymbol{z}} \in \hat{\boldsymbol{\mathcal{Z}}}} \min_{\boldsymbol{z} \in \boldsymbol{\mathcal{Z}}^{\text{true}}} d_v(\boldsymbol{z}, \hat{\boldsymbol{z}})^2$$

where $d_p(\boldsymbol{z}, \boldsymbol{z}') = \sqrt{(x - x')^2 + (y - y')^2}$ and $d_v(\boldsymbol{z}, \boldsymbol{z}') = \sqrt{(v_x - v_x')^2 + (v_y - v_y')^2}$ are the errors in position and velocity, respectively. Figure 4.3 shows the Root Mean Square Error (RMSE) in range-doppler estimated at sensor level for different number of targets in a *well-separated* case. The RMSE converges to the CRB bound as SNR increases and the SNR at which this convergence occurs is called as SNR threshold. The SNR threshold provides an indicator for the localization performance when multiple targets, $N_T > 1$ are present. We observe that range, doppler RMSE at individual sensors achieves CRB at a SNR= -15 dB threshold. The RMSE for position, velocity estimates obtained from sensor observations also achieve their CRB at the same SNR threshold. This shows that

association using $SAGA$ does not introduce any additional errors to the localization process when SNR is above this threshold. However, the RMSE increases sharply below the SNR threshold due to the difficulty in associating noisy range-doppler pairs. Therefore, we use nominal $SNR = -10$ dB in our simulations to perform further analysis.
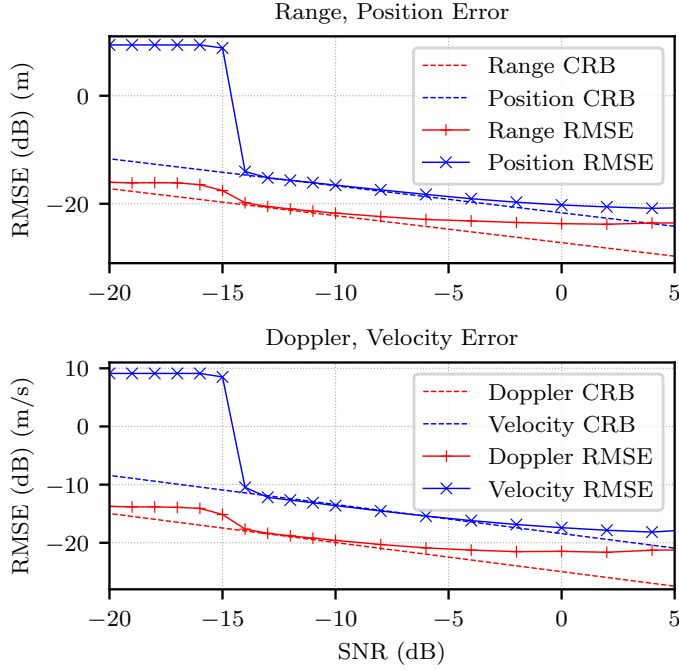
Figure 4.3: Range-Dopper estimation accuracy and Position-Velocity estimation accuracy versus SNR.

Cardinality Error and OSPA: In the case of multiple targets, the number of *valid* targets identified by the system is also an important performance metric. An estimated target $\hat{z}$ is classified to be *valid* only if it lies within a region "close" to the true targets, $\min_{z \in \mathcal{Z}^{\text{true}}} \|\hat{z} - z\| < \bar{d}$ where $\bar{d}$ sets the maximum error threshold. The cardinality error is defined as the difference between actual number of targets and the number of estimated target; that is, $N_T - N_e = |\mathcal{Z}^{\text{true}}| - |\hat{\mathcal{Z}}|$. That error is caused due to the detection anomalies in the estimation algorithm at sensor level as well as during the association stage. In such cases, the localization accuracy by itself does not capture the

true performance of the system. Therefore, we use the OSPA metric [62], which combines the localization and cardinality error into a single performance metric and is given by,

$$\texttt{OSPA}(\hat{\boldsymbol{\mathcal{Z}}}) = \sqrt{\frac{1}{n(\hat{\boldsymbol{\mathcal{Z}}})}\left(\sum_{i=1}^{m}\min\left(d_c(\hat{\boldsymbol{z}}_i),\bar{d}\right)^2 + |N_e - N_T|\bar{d}^2\right)} \tag{4.19}$$

where m is the number of *valid* targets, $N_e - N_T$ is the cardinality error and $d_c(\hat{\boldsymbol{z}}_i)$ is the localization error computed relative to *closest* true target given as

$$d_c(\hat{\boldsymbol{z}}_i) = \min_{\boldsymbol{z}\in\boldsymbol{\mathcal{Z}}^{\text{true}}} d_p(\boldsymbol{z},\hat{\boldsymbol{z}}_i)^2 + d_v(\boldsymbol{z},\hat{\boldsymbol{z}}_i)^2 \,.$$

Figure 4.4 shows the OSPA error along with the localization and cardinality errors with increasing scene density in the *well-separated* case. Both localization error and cardinality error start to increase as the scene gets denser until a breaking point where the cardinality error increases significantly. At SNR=-15 dB, this breaking point occurs near $N_T = 17$ for *SAGA* whereas $N_T = 21$ for Brute force algorithm. Notice that the localization error is misleading beyond this point since it only considers the errors in the reduced set of *valid* targets. Hence, the OSPA metric effectively combines both quantities so that it represents localization error only when scene is sparse and cardinality errors when the scene is dense. We observe that *SAGA* has slightly worse overall performance compared to the Brute force search as the number of targets increases. However, the performance difference reduces as we increase SNR. Moreover, *SAGA* obtains the association with significantly lower complexity than Brute force as we show in the next section.

4.4.2   Complexity Reduction

In this section, we analyze the computational savings achieved by the proposed *SAGA* algorithm and provide comparison against traditional approaches. In order to effectively
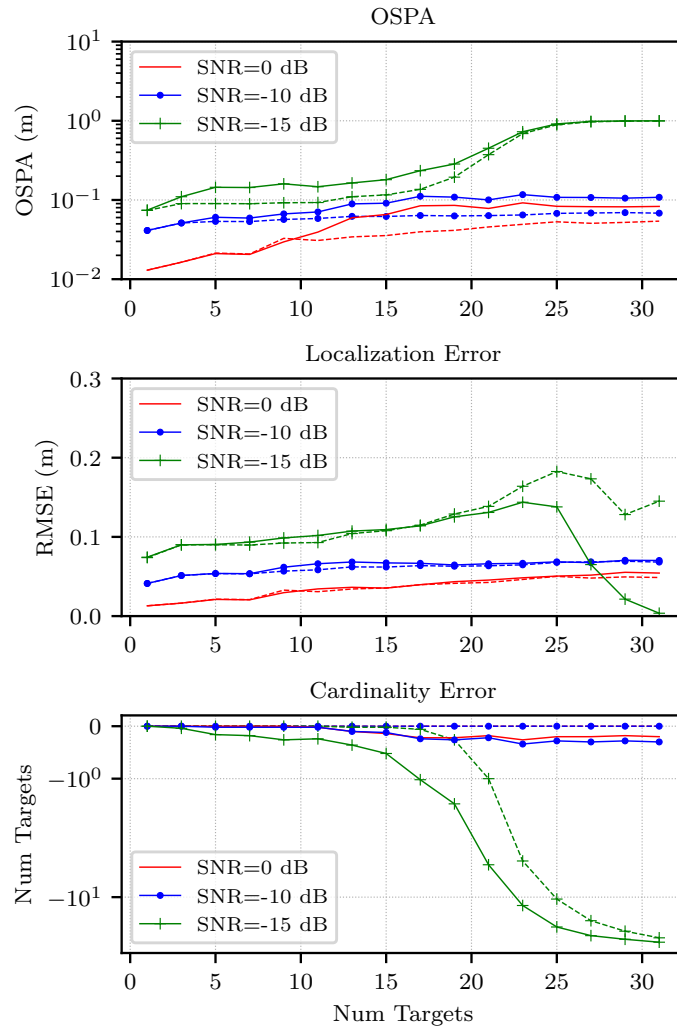
Figure 4.4: Overall localization accuracy versus number of targets at $SNR = -15, -10$ dB. The solid and dotted lines represent the performances of $SAGA$ and Brute force association algorithms, respectively.

compare the performance, we now consider adverse scenes in which the sensor obser-
vations contain detection anomalies. Figure 4.5 shows the graph truncation over the
iterations of the graph search with different miss probabilities for $SAGA$ and Brute force
search. When miss probability is low, $SAGA$ rapidly extracts all chains. As the missed
detections increase, the robust scheme automatically increases the number of iterations
by allowing the relaxation of constraints in DFS graph search. On the other hand, brute
force search always requires large number of iterations.
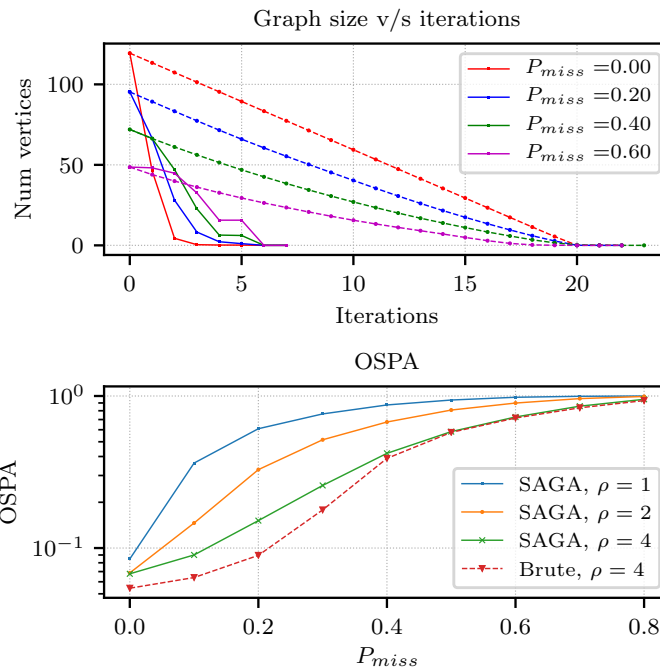
Figure 4.5: (Top) Graph size at end of each iteration of association algorithm for
different P_{miss}. $SAGA$ is denoted by solid line while Brute force is denoted by dotted
line. (Bottom) OSPA versus P_{miss} with different robustness levels ρ.

$SAGA$ provides robustness to the missed detections by selectively adding skip edges to
the graph. This mechanism reduces the OSPA error in adverse scenarios at the expense
of more computational complexity. The level of robustness can be tuned using parameter
ρ based on the adversity of the scene. Figure 4.5 also shows the estimation performance

for different robustness levels with increasing scene adversity (i.e., increasing miss detections). OSPA error reduces with higher robustness levels. However, low robustness level (e.g., $\rho = 1$) is sufficient to obtain good performance at typical miss detection probability $P_{miss} < 0.05$. Similarly, the higher robustness level helps to reduce the cardinality errors when the scene contains higher number of targets. The highest robustness level is $\rho = 4$, which corresponds to the minimum chain length constraint in (4.16a) with $n(\mathcal{A}) \geq 2$.

Runtime Comparison: We now compare the computational complexity of our approach against Brute force. Computing the number of operations that occur during the association process is difficult since the number of chains visited depends on a variety of factors such as the fitting error thresholds and minimum chain length. However, given the same sensor estimates for the simulated scenes, we compare the relative complexities of $SAGA$ against other methods in Figure 4.6 in terms of total number of operations of Floating Point operations (FLOPS) conducted during association and the total runtime. We observe that $SAGA$ exhibits an order of magnitude lower complexity reduction compared to the brute force search algorithm. Moreover, this improvement increases as the number of targets increases, which highlights the advantage of our approach. In addition, the increase in the robustness level of the proposed algorithm (e.g., from $\rho = 0$ to $\rho = 4$) causes a slight increase in complexity compared to brute force approach.

We also compare the complexity against traditional methods such as gated Nearest neighbor filter (NN) and Minimum cost flow (MCF). The NN association scheme [53] builds the association chain by starting with a local kinematic state estimate from a pair of sensor observations and sequentially adding the nearest measurement from other sensors to update this state. The MCF association scheme [49] identifies the most likely set of chain by solving the minimum cost maximum flows over the graph. The cost of each edge is set based on its relative likelihood similar to our brute force method. We use an optimized implementation [63] of MCF for the comparison purposes.
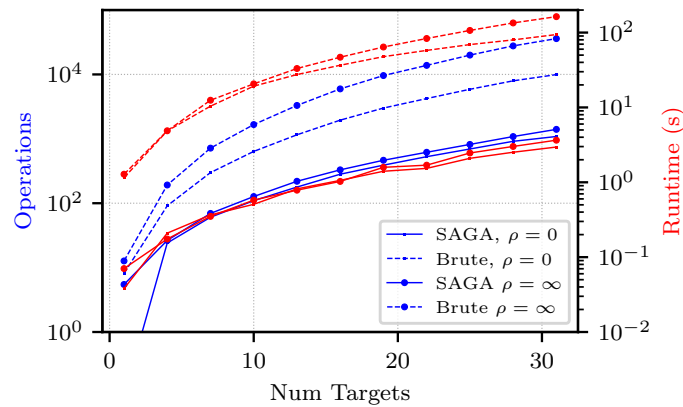
Figure 4.6: Association complexity versus the number of targets averaged over 100 trials using nominal parameters with robustness levels $\rho = 0$ and $\rho = 4$. Total number of FLOPS is denoted by blue line while the runtime is in red.

In order to compare the complexity of those algorithms, we count the number of times the primary objective function (i.e., the likelihood cost in (4.7)) is computed during the graph search procedure. Figure 4.7 provides that comparison with increasing number of targets. *SAGA* has the lowest complexity across all scene densities while *NN* and *MCF* lie between *SAGA* and *Brute* force search. Since the *NN* method is not able to predict the correct chain due to the greedy criteria and requires repeated search over the graph, the total complexity of it approaches to the complexity of the Brute Force search as the scene becomes dense. On the other hand, *MCF* algorithm predicts the chains relatively well and its complexity lies between our approach and *NN*.

Figure 4.8 shows the overall runtime of algorithms for an increasingly denser scene. We observe that *SAGA* is faster than the other methods by an order of magnitude. Since, the FLOPS count is not available from those implementations, we only compare the overall runtime which follows similar trends as FLOPS count and provides a reasonable estimate of algorithmic complexity.
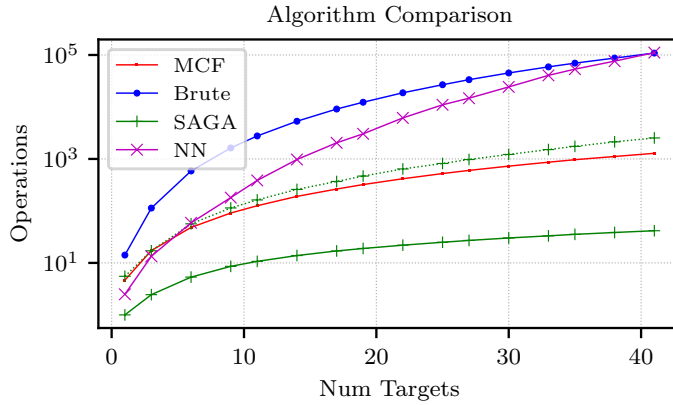
Figure 4.7: Number of evaluations of Likelihood, $\mathcal{L}(\mathcal{A})$ (solid) and Geometric fitting error $F(\mathcal{A})$(dotted) with increasing number of targets.
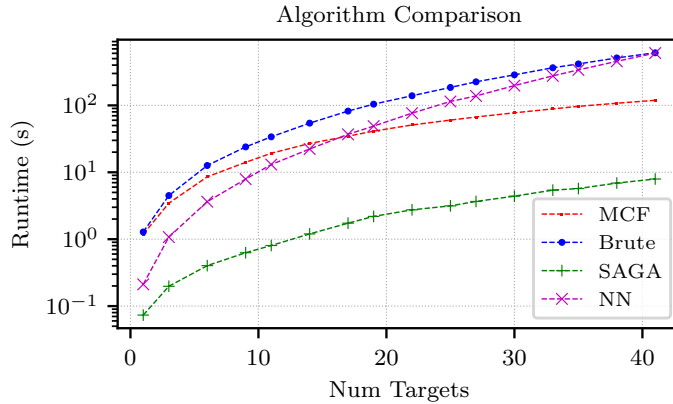
Figure 4.8: Runtime comparison with traditional algorithms.

4.4.3 Benefit of Super-Resolution

Our algorithm extracts the geometric relationships between range-doppler measurements based on the sensor array geometry and builds the association chains by adding likely observations at new sensors to the existing chains. In this section, we investigate the role of enhanced accuracy of range and doppler estimates obtained using NOMP [9] super-resolution algorithm in spatial association by providing comparison against coarse

estimates obtained using DFT. Figure 4.9 shows the localization and cardinality error for both cases. From the figure, it is obtained that the localization accuracy using NOMP estimates achieves the CRB when number of targets are moderate, whereas DFT has higher RMSE as expected. However, the RMSE of NOMP deviates away from CRB as the number of targets increases and approaches to the DFT accuracy for dense scenes. It is important to note that our association algorithm works even with the coarse estimates even though NOMP provides accuracy boost for our algorithm which identifies more targets resulting in lower cardinality errors compared to DFT in the presence of multiple targets.
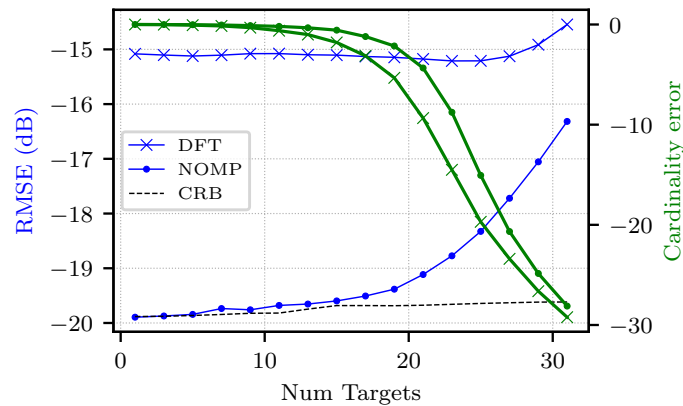
Figure 4.9: Estimation accuracy (thin) and cardinality error (thick) versus number of targets at SNR = -15 dB.

Since NOMP estimates are more accurate, their geometric fitting errors are better than DFT. This allows the reduction in association time at the expanse of some computation overhead over DFT during estimation. Figure 4.10 compares the runtime of the estimation and association stages with different number of sensors for $N_T = 20$ targets. We observe that the association time with NOMP estimates is more than 10 times lower than the one with DFT estimates while the estimation overhead is about $2 - 3$ times. This complexity reduction is due to the lower geometric fitting error of association chains

formed using higher accuracy NOMP estimates. Figure 4.10 also shows that the complexity of association stage becomes more significant than the one of estimation stage for the overall complexity as the number of targets and the number of sensors increases. Therefore, the overall complexity reduction achieved via enhanced accuracy estimates becomes more pronounced with a denser scene and larger number of sensors.
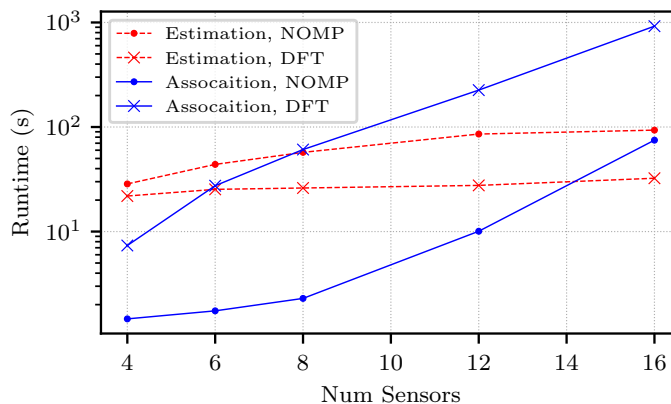
Figure 4.10: Runtime comparison of association (solid) & estimation (dotted) stages versus number of sensors.

4.4.4   Array Geometry

In this subsection we analyze the localization performance of linear sensor arrays from the perspective of data association. We consider the adverse scene with $P_{miss} = 0.2$ to emphasize our findings. The array width and the number of sensors affect both localization accuracy and association complexity.

Increasing the array width generates more spatial diversity in range-doppler measurements across sensors. This helps to reduce the OSPA error for a given number of sensors. On the other hand, larger distance among the sensors weakens the pruning criteria for the graph edges used in (4.8) resulting in a denser graph with a higher number of potential associations between sensors. Therefore, the overall localization performance improves

with wider arrays at the expense of slightly more association complexity. The available sensor width is an important design constraint in practical applications (e.g., length of side profile of a vehicle). For that reason, we analyze the effect of number of sensors in the presence of fixed array width $L_W = 4$ m.
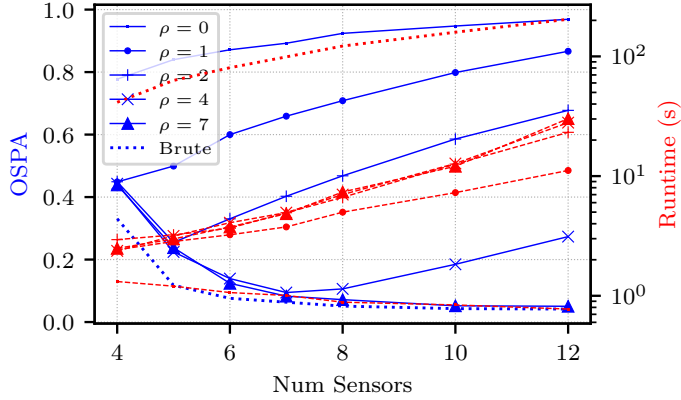
Figure 4.11: Association versus number of sensors for Brute force (thick dotted), SAGA (thin solid) with different robustness levels.

We find that increasing the number of sensors also improves association performance as well as association complexity. Figure 4.11 shows OSPA versus number of sensors for Brute force and *SAGA*. While the OSPA for Brute force association reduces with more sensors, we observe that the OSPA for *SAGA* with robustness level ρ achieves minimum OSPA with $N_s = \rho + 3$ sensors, and increases for $N_s > \rho + 3$. This is caused due to the missed observations, which prevent formation of chains with minimum length constraint $N_s - \rho$. For an array with N_s sensors and a robustness level of ρ, the expected number of missed targets can be expressed as,

$$\mathbb{E}[\text{miss}] = \sum_{k=1}^{\min{(N_s-2,\rho+1)}} \binom{N_s}{k} P_{miss}^k (1 - P_{miss})^{N_s-k}$$

Figure 4.12 shows that missed targets observed using our approach closely match this

expected value for various values of ρ, N_s.
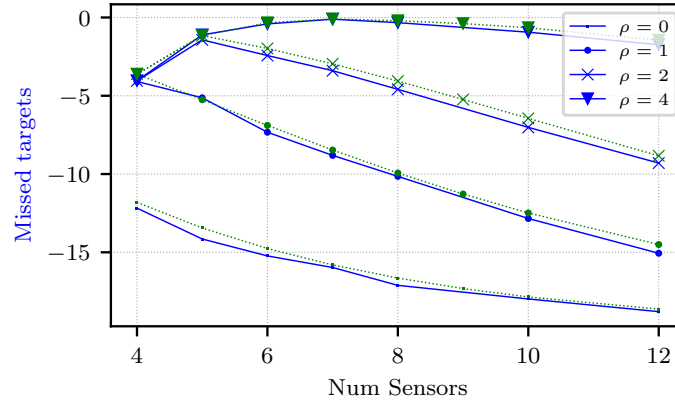
Figure 4.12: Comparison of simulated (solid) and theoretical (dotted) cardinality error.

As a result, we obtain that the robustness level needs to be increased to avoid higher cardinality errors even though localization error reduces with more sensors. That causes increase in the complexity of our algorithm; however, it still achieves lower complexity compared to Brute force algorithm. A more sophisticated method can be devised to select a subset of sensors only during the association stage to . However, this remains an open issue beyond our current scope.

Chapter 5

Conclusions and Future Work

In this dissertation, we have provided two examples where inherent geometric relations within an optimization problem were exploited to drastically reduce the computational complexity. We conclude by discussing some open problems and summarizing the main contribution,

5.1 Large effective aperture design using array of subarray architecture

We have shown that a large effective aperture can be designed by an optimized sparse placement of subarray which produces smaller beam width than a compact placement. This is achieved by a multi-objective optimization framework that exploits geometric heuristics to reduce computational complexity. Our results demonstrate that trading off beam width versus side lobes when synthesizing a large effective aperture does indeed produce performance gains in bearing estimation. Compared to a naive sparse placement, the control of side lobes via our optimized placement produces the most significant gains when estimating the bearing for multiple sources.

Exploring the application of our framework for communications, where transmit and receive beamforming gains are fixed by the number of elements, but control of beam width and sidelobes affects interference, is an interesting direction. In the context of sensing, our work may be viewed as design of an individual sensor which can be placed within a more comprehensive architecture, such as a network of sensors for localization and tracking.

In our tiled architecture, the locations of antenna elements in a subarray are fixed once we specify the location of the subarray center. This constraint makes it difficult to adapt the extensive literature on sparse array optimization, which typically considers elements that can be freely placed, for our present purpose. The difficulty is compounded by the lack of closed form expressions for beam attributes of interest. However, since the objectives are only mildly dependent on the configuration of elements *within* a subarray, it might be possible to simplify the optimization problem, and possibly adapt ideas from the literature on sparse array optimization. This is an interesting direction for future research, especially given the importance of tiled architectures in realizing a large aperture leveraging low-cost hardware for subarrays with a moderate number of elements.

5.2   Enhanced Estimation accuracy and resolution

The estimation-theoretic bounds computed here indicate the potential of low cost mmWave sensors to get adequate resolution in short to medium range localization applications. Super-resolution algorithms for per-sensor range-Doppler estimation yield performance close to the estimation-theoretic bounds. Combining these measurements over multiple sensors yields accurate position and velocity estimates, as long as the array geometry is suitably designed. While we have considered a simple point target model here, more sophisticated extended target models become important at short ranges [64, 65],

and is an interesting area our future work.

5.3   Low Complexity Spatial Association

We have shown that simple constraints relating range-Doppler observations to sensor geometry can be exploited to significantly reduce the complexity of spatial association. Our system-level simulations demonstrate that our framework for spatial association based on these geometric constraints is robust to noisy observations and detection anomalies, and that it scales well with the number of sensors and targets. Our approach is compatible with standard FFT-based range-Doppler processing, but enhanced accuracy estimation at each sensor (i.e., super-resolution of range and Doppler) significantly improves both localization accuracy and association complexity. Important topics for future investigation include extending these concepts to more complex target models (e.g., for extended targets, and targets causing both specular and diffuse reflection), and combining them with complementary strategies utilizing platform and/or target motion across multiple snapshots.

Appendix A

Sparse Array

A.1 Mean square error in 2D DoA estimation

For 2D DoA estimation, the error along any given angle ξ is given by $\boldsymbol{a}^T \boldsymbol{R}_{\epsilon} \boldsymbol{a}$, where $\boldsymbol{a} = [\cos\xi, \sin\xi]^T$ is the directional cosine and $\boldsymbol{R}_{\epsilon}$ is the error covariance matrix. Assuming that $\{\nu_i, \boldsymbol{q_i}, i = 1, 2\}$, denote the eigenvalues and eigenvectors of $\boldsymbol{R}_{\epsilon}$, the MSE averaged over $\boldsymbol{a}$ (assume ξ uniform over $[0, 2\pi]$) is given by

$$
\begin{aligned}
\mathrm{MSE} = \mathbb{E}_{\boldsymbol{a}}\left[\boldsymbol{a}^T \boldsymbol{R}_{\epsilon} \boldsymbol{a}\right] &= \nu_1 \mathbb{E}_{\boldsymbol{a}}\left[\left|\boldsymbol{a}^T \boldsymbol{q_1}\right|^2\right] + \nu_2 \mathbb{E}_{\boldsymbol{a}}\left[\left|\boldsymbol{a}^T \boldsymbol{q_2}\right|^2\right] \\
&= \nu_1 \frac{||\boldsymbol{q_1}||^2}{2} + \nu_2 \frac{||\boldsymbol{q_2}||^2}{2} = (\nu_1 + \nu_2)/2 = \frac{1}{2}tr(\boldsymbol{R}_{\epsilon})
\end{aligned}
$$

where we have used $\mathbb{E}[\cos^2\xi] = \mathbb{E}[\sin^2\xi] = \frac{1}{2}$.

A.2 2D Beamwidth & CRB

We define 2D beamwidth using the Taylor series expansion of beampattern $R_{\boldsymbol{u}_o}(\boldsymbol{u})$ around mainlobe $R_{\boldsymbol{u}_o}(\boldsymbol{0})$. Since the beampattern around the main lobe. and hence the

beamwidth, is invariant to beamforming direction (see 2.2.3), we assume $\boldsymbol{u_o} = \boldsymbol{0}$ without loss of generality, and drop the subscript: $R_{\boldsymbol{0}}(\boldsymbol{u}) \triangleq R(\boldsymbol{u})$. By taking the derivatives of (2.2), theTaylor series expanision up to second order is obtained as

$$R(\boldsymbol{u}) \approx R(\boldsymbol{0}) - \frac{k^2}{N}\boldsymbol{u}^T\boldsymbol{D}^T\boldsymbol{D}\boldsymbol{u} \tag{A.1}$$

We define Half Power Beam Contour ($HPBC$) as the closed contour around mainbeam with $\{\boldsymbol{u} : R(\boldsymbol{u}) = 0.5R(\boldsymbol{0})\}$, which is approximated as an ellipse using (A.1) as follows:

$$\boldsymbol{u}^T\boldsymbol{D}^T\boldsymbol{D}\boldsymbol{u} = \frac{N}{2k^2}R(\boldsymbol{0}) \tag{A.2}$$

Consider the eigendecomposition of $\boldsymbol{D}^T\boldsymbol{D}$ given by,

$$\boldsymbol{D}^T\boldsymbol{D} = \lambda_1\boldsymbol{p}_1\boldsymbol{p}_1^T + \lambda_2\boldsymbol{p}_2\boldsymbol{p}_2^T \tag{$\lambda_2 \geq \lambda_1$}$$

The eigenvectors $\boldsymbol{p}_2, \boldsymbol{p}_1$ correspond to major and minor axis of $HPBC$ ellipse respectively, and depend only on the element positions.
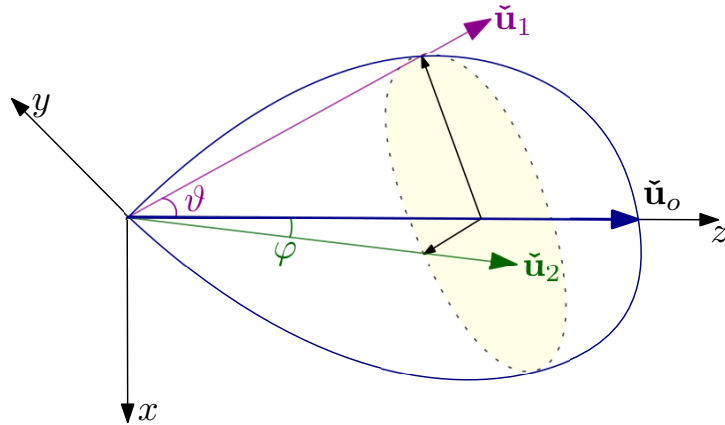

Figure A.1: 2D Beamwidth

Figure A.1 shows the mainlobe of a beam and the dotted shaded region represents

its *HPBC* ellipse. $\check{\boldsymbol{u}}_o, \check{\boldsymbol{u}}^1, \check{\boldsymbol{u}}^2$ correspond to unit vectors in the direction of main beam, vertex and co-vertex of the *HPBC* where, $\check{\boldsymbol{u}} = [u, v, \sqrt{1 - u^2 - v^2}]$ is the unit vector towards directional cosine $\boldsymbol{u} = [u, v]$. These can be expressed as,

$$\check{\boldsymbol{u}}_o = \begin{bmatrix} 0 \\ 0 \\ 1 \end{bmatrix}, \check{\boldsymbol{u}}_1 = \begin{bmatrix} \sin \vartheta \cos \phi_{\max} \\ \sin \vartheta \sin \phi_{\max} \\ \cos \vartheta \end{bmatrix}, \check{\boldsymbol{u}}_2 = \begin{bmatrix} \sin \varphi \cos \phi_{\min} \\ \sin \varphi \sin \phi_{\min} \\ \cos \varphi \end{bmatrix} \tag{A.3}$$

where $\phi_{\max}, \phi_{\min}$ are perpendicular azimuthal angles and ϑ, φ are the maximum and minimum beamwidth angles subtended from the major and minor axis of this ellipse to the mainbeam.

$$\mathrm{BW}_{\max} = \vartheta = \left(\frac{360}{\pi} \right) \cos^{-1} (\check{\boldsymbol{u}}_o \check{\boldsymbol{u}}_1) \tag{A.4}$$

$$\mathrm{BW}_{\min} = \varphi = \left(\frac{360}{\pi} \right) \cos^{-1} (\check{\boldsymbol{u}}_o . \check{\boldsymbol{u}}_2) \tag{A.5}$$

Substituting the major and minor axis from (A.3) in (A.2), we obtain

$$\lambda_1 \sin^2 \vartheta = \frac{N}{2k^2} R(\boldsymbol{0}) \implies \sin \vartheta \approx \mathrm{BW}_{\max} \propto 1/\sqrt{\lambda_1}$$

$$\lambda_2 \sin^2 \varphi = \frac{N}{2k^2} R(\boldsymbol{0}) \implies \sin \varphi \approx \mathrm{BW}_{\min} \propto 1/\sqrt{\lambda_2}$$

That is, the beamwidths along extremal directions are inversely proportional to the square roots of the eigenvalues of $\boldsymbol{D}^T \boldsymbol{D}$.

Relation to CRB

Using (2.15), the error covariance matrix is lower bounded by

$$\boldsymbol{R}_\epsilon \geq \text{CRB} = J_F^{-1} = \frac{N}{2k^2\gamma} \left(\boldsymbol{D}^T\boldsymbol{D}\right)^{-1}$$

$$= \frac{N}{2k^2\gamma} \left(\frac{1}{\lambda_1}\boldsymbol{p}_1\boldsymbol{p}_1^T + \frac{1}{\lambda_2}\boldsymbol{p}_2\boldsymbol{p}_2^T\right) \qquad \text{(using } (\lambda_2 \geq \lambda_1))$$

Using Appendix A.1, the MSE can be lowerbounded by

$$\text{MSE} \geq \overline{\text{CRB}} = \frac{1}{2}tr(J_F^{-1}) = \frac{N}{4k^2\gamma}\left(\frac{1}{\lambda_1} + \frac{1}{\lambda_2}\right)$$

$$= \frac{N}{4k^2\gamma}\left(\sin^2(\vartheta) + \sin^2(\varphi)\right)$$

$$\propto \frac{(\text{BW}^{\text{DoA}})^2}{\text{SNR}}$$

where $\text{BW}^{\text{DoA}} = \sqrt{\text{BW}_{\max}^2 + \text{BW}_{\min}^2} = \sqrt{\vartheta^2 + \varphi^2}$ is defined as MSE beamwidth ($\sin\theta \approx \theta$ for small angles θ).

A.3 Vacancy search operator

Our reference subarray module shown in Figure A.2 occupies space in addition to antenna elements. In order to keep element polarizations aligned, these modules can be placed in either *up* ($0°$) or *down* ($180°$) pose. We outline a procedure to list the vacant gridpoints $V_i = \mathcal{T}(\boldsymbol{C}_i^n)$ where the *new* subarray can be placed without overlapping with already placed *dormant* subarrays at $\boldsymbol{C}_i^n$. We define the subarray state as the center $\boldsymbol{c}$ of the element pattern and its *pose* ν, since vacancies depend on both parameters.

$$\tilde{\boldsymbol{c}} = \{\boldsymbol{c}, \nu\} \forall \boldsymbol{c} \in \boldsymbol{C}_i^n, V_i$$

The pose variable $\nu \in \{\nu^u, \nu^d, \nu^f\}$ denotes whether subarray can be placed in up only(ν^u), down only(ν^d) or free pose (ν^f, either up or down) at the location c. For a given set of *dormant* subarray states, $\tilde{\boldsymbol{C}}_i^n$ we identify all vacant states $\tilde{V}_i$ for placing the *new* subarray. Once a *new* subarray is placed, the states of all dormant subarrays are updated (e.g., a free pose may switch to an up pose if the down pose becomes infeasible).
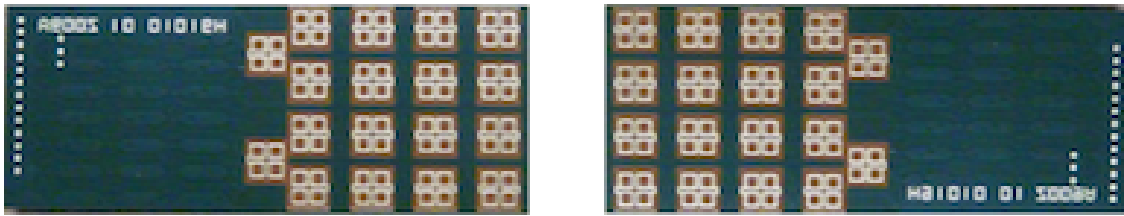
Figure A.2: The Subarray module and its two possible poses. Golden section are copper patch antennas on the green colored chip.

A.4   Perturbation of array

In order to design a bin size for pruning array configurations, we analyze the effect of perturbing the location of a single array element on the eigenvalues of the array covariance matrix. Consider a small perturbation $\boldsymbol{v} = [v_x, v_y]$ added to i^{th} array element position: $\bar{\boldsymbol{d}}_i = \boldsymbol{d}_i + \boldsymbol{v}$. The covariance for the perturbed array is

$$\boldsymbol{\Sigma}_{\bar{\boldsymbol{D}}} = \left(\boldsymbol{D}^T\boldsymbol{D} + \boldsymbol{v}^T\boldsymbol{v} + 2\boldsymbol{d}_i^T\boldsymbol{v}\right)/N = \boldsymbol{\Sigma}_{\boldsymbol{D}} + \boldsymbol{\mathcal{G}} + 2\boldsymbol{\mathcal{H}}$$

where

$$\boldsymbol{\mathcal{G}} = \frac{1}{N}\begin{bmatrix} v_x^2 & v_x v_y \\ v_x v_y & v_y^2 \end{bmatrix}, \quad \boldsymbol{\mathcal{H}} = \frac{1}{N}\begin{bmatrix} v_x d_{xi} & v_x d_{yi} \\ v_y d_{xi} & v_y d_{yi} \end{bmatrix}$$

Using Weyl's inequality [66] for real symmetric matrices, the eigenvalue perturbation

is bounded as

$$|\bar{\lambda}_i - \lambda_i| \leq \|\mathcal{G} + 2\mathcal{H}\|_2 \leq \|\mathcal{G}\|_2 + 2\|\mathcal{H}\|_2$$

$$\leq \|\mathcal{G}\|_F + 2\|\mathcal{H}\|_F$$

The frobenius norms of $\mathcal{G}, \mathcal{H}$ are

$$\|\mathcal{G}\|_F = \left(v_x^2 + v_y^2\right)/N$$

$$\|\mathcal{H}\|_F = R_i \sqrt{\left(v_x^2 + v_y^2\right)}/N$$

where $R_i = \sqrt{d_{xi}^2 + d_{yi}^2}$ is the distance of the ith element from the array center. Hence, the overall variation of eigenvalues with variation $\Delta_e = \sqrt{\left(v_{xi}^2 + v_{yi}^2\right)}$ of the ith element is

$$|\bar{\lambda}_i - \lambda_i| \leq \frac{(2R_i + \Delta_e)}{N}\Delta_e \tag{A.6}$$

Thus, the eigenvalues are more sensitive to perturbations in the locations of elements further from the center. For perturbations within one grid size used in our placement search algorithm, the eigenvalue of the subarray center covariance can vary at most by $\frac{(2R_i + \sqrt{2}\Delta_g)}{N_s}\sqrt{2}\Delta_g$, and we use this as a guideline for discretizing the eigenvalues for removing geometrically similar configurations.

Appendix B

Estimation and Association

B.1 Association Constraint Relaxation

The choice of initial stopping thresholds τ_f^n and τ_l^n and scaling factor β for subsequent relaxations in $SAGA$ algorithm governs the total complexity of association algorithm. In order to initialize the association algorithm, we set tight thresholds for $\mathcal{L}(\mathcal{A})$ and $\mathcal{F}(\mathcal{A})$. Assuming the range-doppler observations have small error (i.e., $w_i^R \ll r_i$, $w_i^D \ll d_i$ in (4.3)), the expected negative log likelihood in (4.5) can be approximated as

$$\mathcal{L}(\mathcal{A}) \approx \sum_{\boldsymbol{\theta}_i \in \mathcal{A}} \left(\frac{(w_i^r)^2}{\sigma_r^2} + \frac{(w_i^d)^2}{\sigma_d^2} \right) .$$

Since $w_i^R \sim \mathcal{N}(0, \sigma_r^2)$ and $w_i^D \sim \mathcal{N}(0, \sigma_d^2)$ are standard Normal distributed random variables, $\mathcal{L}(\mathcal{A}^k)$ has chi-squared distribution, $\chi_{2n(\mathcal{A})}^2$ with $2n(\mathcal{A})$ degrees of freedom.

Then, the expected fitting error in (4.14) can be approximated as

$$F(\mathcal{A}) = \sum_{\boldsymbol{\theta}_i \in \mathcal{A}} \frac{\left((\hat{r}_i \hat{d}_i) - (r_i d_i)\right)^2}{\eta_1} + \frac{\left((\hat{r}_i)^2 - (r_i)^2\right)^2}{\eta_2}$$

$$\approx \sum_{\boldsymbol{\theta}_i \in \mathcal{A}} \frac{\left(r_i w_i^D + d_i w_i^R\right)^2}{\eta_1} + \frac{\left(2 r_i w_i^R\right)^2}{\eta_2} \tag{B.1}$$

where ($\hat{r}_i$ and $\hat{d}_i$) denote the perceived range-doppler pair at sensor i for predicted state $\boldsymbol{z}$ and $\boldsymbol{\theta}_i = (r_i, d_i)$ denotes the observed range-doppler pair at sensor i. The normalization factors η_1, η_2 are set to the variance of numerator terms which is,

$$(\eta_1)_i = \mathrm{Var}[r_i w_i^d + d_i w_i^r] \approx \sigma_{r_i}^2 d_i^2 + r_i^2 \sigma_{d_i}^2 + \sigma_{r_i}^2 \sigma_{d_i}^2$$

$$(\eta_2)_i = \mathrm{Var}[2 r_i w_i^r] \approx 4 r_i^2 \sigma_{r_i}^2$$

Using those values to normalize (B.1) results in $\mathcal{F}(\mathcal{A}^k) \sim \chi_{2n(\mathcal{A})}^2$ being chi-squared distributed with $2n(\mathcal{A})$ degrees of freedom. Hence, the thresholds for the association algorithm are determined as follows,

$$\tau_f^{n(\mathcal{A})} : \mathrm{Pr}(F(\mathcal{A}) > \tau_f^{n(\mathcal{A})}) = P_{\mathrm{FA}}$$

$$\tau_l^{n(\mathcal{A})} : \mathrm{Pr}(\mathcal{L}(\mathcal{A}) > \tau_l^{n(\mathcal{A})}) = P_{\mathrm{FA}}$$

where P_{FA} is the nominal false alarm rate set to 0.01.

Note that while the normalization factors η_1, η_2 depend on r_i, d_i, we set this based on the maximum range, doppler values to get a conservative initial value. This does not cause a problem since the sucessive relaxation procedure loosens that threshold so that chains with high fitting error can be extracted.

The relaxation factor, β should be set appropriately. Choosing a high value causes faster convergence but might leads to false chains being identified. On the other hand, a low value delays the extraction of *loose* chains. In the simulations, we find that $\beta = 2$ performs well.

B.2   Minimum Ambiguity Association

Lemma 1 *In the ideal detection scenario (i.e., no miss or false alarms), the phantoms generated between a pair of sensors is minimum for consecutive sensors.*

Proof: Recall that phantom targets are generated when range perceived at a pair of sensors satisfy conditions (4.8). For a phantom, $\boldsymbol{z}_{ij}^{pq}$ generated by incorrectly associated observations, $\boldsymbol{\theta}_i^p, \boldsymbol{\theta}_j^q$, across consecutive sensors i, j, following relations hold,

$$r_i^p - r_j^q < l_{ij}, \quad r_i^p + r_j^q > l_{ij} \tag{B.2}$$

Now consider $\bar{q}^{th}$ observation at sensor k adjacent to sensor j which corresponds to same target as $\boldsymbol{\theta}_j^q$, the following relations hold,

$$r_j^q - r_k^{\bar{q}} < l_{jk} \qquad\qquad\qquad \text{(using (4.8))}$$

$$r_j^q + l_{jk} > r_k^{\bar{q}} \qquad\qquad\qquad (l_{jk} \geq 0, \text{ Triangle inequality})$$

Using these along with (B.2) we obtain,

$$r_i^p - r_k^{\bar{q}} < l_{ik}, \quad r_i^p + r_k^{\bar{q}} > l_{ik}$$

Hence any phantom produced between consecutive sensors i, j also generates a phantom

between sensors i, k by skipping over intermediate sensor j. Hence,

$$\sum_{p=1}^{n(\Theta_i)} \sum_{q=1}^{n(\Theta_{i+1})} n(\boldsymbol{z}_{i,i+1}^{pq}) \leq \sum_{p=1}^{n(\Theta_i)} \sum_{q=1}^{n(\Theta_k)} n(\boldsymbol{z}_{i,k}^{pq})$$

Therefore, phantoms generated between a pair of sensors is minimum for consecutive sensors. ∎

Association complexity is due to the presence of unwanted phantom targets which need to be discarded based on their likelihood. When a target is observed at all sensors, it is sufficient to associate observations along consecutive sensors. Lemma 1 states that the association of observations along consecutive sensors generates the lowest number of phantoms during graph search. Hence, the number of potential ambiguities are minimized when the graph search procedure is conducted across consecutive sensors first.

B.3   Depth First Search

A depth first search algorithm is outlined in Algorithm 5. At each node, the DFS procedure traverses through all branches which have geometric fitting error below the maximum error threshold $\tau_f^{N_s}$. On reaching the end of the graph, we select the chain if it satisfies the likelihood, fitting error and minimum chain length constraints. In addition, we check for possible chain termination at each node after going through all its branches. This step implicitly accounts for the NULL state at the end of a chain.

B.4   CRB for Position and Velocity

Using the range-doppler model in Section 4.3, we evaluate the single target CRB for kinematic parameters $\bar{\boldsymbol{z}}$ using the log likelihood of range-doppler observations $\mathcal{A} =$

Algorithm 5 Geometry Assisted Depth First Search

1: **Procedure**GA-DFS$v, \mathcal{A}, \gamma, \boldsymbol{\tau}$
2: Get list of children of v that *geometrically fit*, $\quad B(v) = \left\{ v_j : \mathcal{F}([\mathcal{A}, v_j]) < \tau_f^{N_s} \right\}$
3: **if** $B(v) \neq \emptyset$ **then**
4:     Sort $B(v)$ using geometric fitting error, $F([\mathcal{A}, v_j])$
5:     **for** $v_j \in B(v)$ **do**
6:         BRANCH out a new chain $\mathcal{A}^j : \mathcal{A} \leftarrow v_j$
7:         $\mathcal{A}^o \leftarrow$ CALL GA-DFS$(v_j, \mathcal{A}^j, \gamma, \boldsymbol{\tau})$
8:         Exit loop if valid chain $\mathcal{A}^o$ is found.
9:     **end for**
10: **end if**
11: CHECK IF CHAIN CAN BE TERMINATED AT v
12: **if** $n(\mathcal{A}) \geq \gamma, \mathcal{L}(\mathcal{A}) < \tau_l^{n(\mathcal{A})}, F(\mathcal{A}) < \tau_f^{n(\mathcal{A})}$ **then**
13:     SELECT $\mathcal{A}^o \leftarrow \mathcal{A}$,
14: **end if**
15: **Output:** $\mathcal{A}^o$
16: **EndProcedure**

$\{\boldsymbol{\theta}_i\}_{i=1}^{N_s}$ given kinematic state $\bar{\boldsymbol{z}}$, which is

$$\mathcal{L}\left(\{\boldsymbol{\theta}_i | \bar{\boldsymbol{z}}\}_{i=1}^{N_s}\right) = \sum_{i=1}^{N_s} \left(\frac{(\bar{r}_i - r_i)^2}{\sigma_{r_i}^2} + \frac{(\bar{d}_i - d_i)^2}{\sigma_{d_i}^2} \right)$$

where $\boldsymbol{\theta}_i = (r_i, d_i)$ are observed range-doppler pair for sensor i, $(\bar{r}_i, \bar{d}_i) = \mathcal{T}_i(\bar{\boldsymbol{z}})$ is true range-doppler pair for given target state $\bar{\boldsymbol{z}}$ and $\sigma_{r_i}^2$ and $\sigma_{d_i}^2$ are, respectively, the range and doppler CRBs obtained in (3.5). The FIM for $\bar{\boldsymbol{z}}$ can be evaluated as

$$I(\bar{\boldsymbol{z}}) = \mathbb{E}\left[\nabla_{\boldsymbol{z}} \mathcal{L}\left(\{\boldsymbol{\theta}_i | \bar{\boldsymbol{z}}\}_{i=1}^{N_s}\right) \right] .$$

The CRB obtained from inverse FIM is used to find position and velocity CRB as follows,

$$CRB_p = I(\bar{\boldsymbol{z}})_{(1,1)}^{-1} + I(\bar{\boldsymbol{z}})_{(2,2)}^{-1}$$

$$CRB_v = I(\bar{\boldsymbol{z}})_{(3,3)}^{-1} + I(\bar{\boldsymbol{z}})_{(4,4)}^{-1}$$

The CRB of velocity is a function of both range and doppler variances whereas the CRB of position only depends on the variance of range. We use the nominal range and doppler CRB values to set the minimum separation distance threshold, $\tau_z = 10\sqrt{CRB_p + CRB_v}$ between targets. This threshold is also used to check similarity between chains in the association algorithm.

B.5 Convergence of SAGA Algorithm

In this section, we show that the solution of proposed algorithm approaches true value as the chain length increases. Let $\boldsymbol{q}_1^*$ and $\boldsymbol{q}_2^*$ denote the true range-doppler product and range squared vectors for a chain $\mathcal{A}$, respectively. The resulting error in the estimate of kinematic parameters found in Section 4.3.2 can be expressed as

$$e(\mathcal{A}) = \boldsymbol{u}^T(\boldsymbol{q} - \boldsymbol{q}^*) = \boldsymbol{u}^T(\boldsymbol{\xi}).$$

Then, the resulting mean square error becomes

$$\begin{aligned}
\mathbb{E}[e^2(\mathcal{A})] &= \mathbb{E}[(\boldsymbol{u}^T\boldsymbol{\xi}\boldsymbol{\xi}^T\boldsymbol{u}] \\
&= \boldsymbol{u}^T\mathbb{E}[\boldsymbol{\xi}\boldsymbol{\xi}^T]\boldsymbol{u} \\
&\leq \lambda_{max}\|\boldsymbol{u}\| \qquad\qquad \text{(Courant-Fischer-Weyl)} \\
&\leq \frac{\lambda_{max}}{\boldsymbol{e}_1^T(H^TH)^{-1}\boldsymbol{e}_1} = \frac{\lambda_{max}}{Var(\boldsymbol{l})}
\end{aligned}$$

where λ_{max} is the maximum eigenvalue of $\mathbb{E}[\boldsymbol{\xi}\boldsymbol{\xi}^T]$ which approximately corresponds to the largest geometric fitting error over all sensors. The estimation error in x, v_x is inversely proportional to the variance of sensor's x-coordinate, which increases linearly with the number of sensors and quadratically with the array width.

Bibliography

[1] *5g spectrum recommendations*, tech. rep., 5G Americas, April, 2017.

[2] D. Barrett, D. Wang, A. Ahmad, and V. Mahimkar, *Using mmWave sensors to enhance drone safety and productivity*, tech. rep., Texas Instruments, 2017.

[3] D. Barrett and A. Alvarez, *mmWave radar sensors in robotics applications*, tech. rep., Texas Instruments, 2017.

[4] T. Bai and R. W. Heath, *Coverage and rate analysis for millimeter-wave cellular networks*, IEEE Transactions on Wireless Communications **14** (2014), no. 2 1100–1114.

[5] B. Demissie and C. R. Berger, *High-resolution range-doppler processing by coherent block-sparse estimation*, IEEE Transactions on Aerospace and Electronic Systems **50** (April, 2014) 843–857.

[6] R. Deming, J. Schindler, and L. Perlovsky, *Multi-target/multi-sensor tracking using only range and doppler measurements*, IEEE Transactions on Aerospace and Electronic Systems **45** (April, 2009) 593–611.

[7] Y. Chi, L. L. Scharf, A. Pezeshki, and A. R. Calderbank, *Sensitivity to basis mismatch in compressed sensing*, IEEE Transactions on Signal Processing **59** (2011), no. 5 2182–2195.

[8] P. Häcker and B. Yang, *Single snapshot doa estimation*, Advances in Radio Science **8** (2010) 251–256.

[9] B. Mamandipoor, D. Ramasamy, and U. Madhow, *Newtonized orthogonal matching pursuit: Frequency estimation over the continuum.*, IEEE Trans. Signal Processing **64** (2016), no. 19 5066–5081.

[10] A. Gupta, U. Madhow, A. Arbabian, and A. Sadri, *Design of large effective apertures for millimeter wave systems using a sparse array of subarrays*, IEEE Transactions on Signal Processing **67** (2019), no. 24 6483–6497.

[11] A. Moffet, *Minimum-redundancy linear arrays*, IEEE Transactions on antennas and propagation **16** (1968), no. 2 172–175.

[12] T. Birinci and Y. Tanık, *Optimization of nonuniform planar array geometry for direction of arrival estimation*, in *Signal Processing Conference, 2005 13th European*, pp. 1–4, IEEE, 2005.

[13] V. Roy, S. P. Chepuri, and G. Leus, *Sparsity-enforcing sensor selection for doa estimation*, in *Computational Advances in Multi-Sensor Adaptive Processing (CAMSAP), 2013 IEEE 5th International Workshop on*, pp. 340–343, IEEE, 2013.

[14] A. Trucco, *Thinning and weighting of large planar arrays by simulated annealing*, *IEEE transactions on ultrasonics, ferroelectrics, and frequency control* **46** (1999), no. 2 347–355.

[15] P. Pal and P. P. Vaidyanathan, *Nested arrays in two dimensions, part i: Geometrical considerations*, *IEEE Transactions on Signal Processing* **60** (Sept, 2012) 4694–4705.

[16] E. Keto, *Hierarchical configurations for cross-correlation interferometers with many elements*, *Journal of Astronomical Instrumentation* **1** (2012), no. 01 1250007.

[17] S. Joshi and S. Boyd, *Sensor selection via convex optimization*, *IEEE Transactions on Signal Processing* **57** (2008), no. 2 451–462.

[18] E. Tohidi, M. Coutino, S. P. Chepuri, H. Behroozi, M. M. Nayebi, and G. Leus, *Sparse antenna and pulse placement for colocated mimo radar*, *IEEE Transactions on Signal Processing* **67** (2018), no. 3 579–593.

[19] P. Jarske, T. Saramaki, S. K. Mitra, and Y. Neuvo, *On properties and design of nonuniformly spaced linear arrays (antennas)*, *IEEE Transactions on Acoustics, Speech, and Signal Processing* **36** (1988), no. 3 372–380.

[20] F. Athley, C. Engdahl, and P. Sunnergren, *On radar detection and direction finding using sparse arrays*, *IEEE Transactions on Aerospace and Electronic Systems* **43** (2007), no. 4.

[21] R. Schmidt, *Multiple emitter location and signal parameter estimation*, *IEEE transactions on antennas and propagation* **34** (1986), no. 3 276–280.

[22] R. Roy and T. Kailath, *Esprit-estimation of signal parameters via rotational invariance techniques*, *IEEE Transactions on acoustics, speech, and signal processing* **37** (1989), no. 7 984–995.

[23] K. T. Wong and M. D. Zoltowski, *Direction-finding with sparse rectangular dual-size spatial invariance array*, *IEEE Transactions on Aerospace and Electronic Systems* **34** (1998), no. 4 1320–1336.

[24] M. D. Zoltowski and K. T. Wong, *Closed-form eigenstructure-based direction finding using arbitrary but identical subarrays on a sparse uniform cartesian array grid*, IEEE Transactions on Signal Processing **48** (2000), no. 8 2205–2210.

[25] M. Haardt and J. A. Nossek, *Simultaneous schur decomposition of several nonsymmetric matrices to achieve automatic pairing in multidimensional harmonic retrieval problems*, IEEE Transactions on Signal Processing **46** (1998), no. 1 161–169.

[26] V. Vasylyshyn and O. Garkusha, *Direction finding using sparse array composed of multiple identical subarrays*, in *Antenna Theory and Techniques, 2005. 5th International Conference on*, pp. 273–276, IEEE, 2005.

[27] E. Van den Berg and M. P. Friedlander, *Sparse optimization with least-squares constraints*, SIAM Journal on Optimization **21** (2011), no. 4 1201–1229.

[28] C. Stoeckle, J. Munir, A. Mezghani, and J. A. Nossek, *Doa estimation performance and computational complexity of subspace-and compressed sensing-based methods*, in *Smart Antennas (WSA 2015); Proceedings of the 19th International ITG Workshop on*, pp. 1–6, VDE, 2015.

[29] D. Ramasamy, S. Venkateswaran, and U. Madhow, *Compressive parameter estimation in awgn.*, IEEE Trans. Signal Processing **62** (2014), no. 8 2012–2027.

[30] A. H. Nuttall and B. A. Cray, *Approximations to directivity for linear, planar, and volumetric apertures and arrays*, IEEE journal of oceanic engineering **26** (2001), no. 3 383–398.

[31] K. C. Kerby and J. T. Bernhard, *Sidelobe level and wideband behavior of arrays of random subarrays*, IEEE transactions on antennas and propagation **54** (2006), no. 8 2253–2262.

[32] M. J. Lee, L. Song, S. Yoon, and S. R. Park, *Evaluation of directivity for planar antenna arrays*, IEEE Antennas and Propagation Magazine **42** (2000), no. 3 64–67.

[33] O. Lange and B. Yang, *Antenna geometry optimization for 2d direction-of-arrival estimation for radar imaging*, in *Smart Antennas (WSA), 2011 International ITG Workshop on*, pp. 1–8, IEEE, 2011.

[34] K. L. Bell, Y. Ephraim, and H. L. Van Trees, *Explicit ziv-zakai lower bound for bearing estimation*, IEEE Transactions on Signal Processing **44** (1996), no. 11 2810–2824.

[35] J. Proakis and M. Salehi, *Digital Communications, 5th edition*. McGraw-Hill Higher Education, 2008.

[36] Z. Marzi, D. Ramasamy, and U. Madhow, *Compressive channel estimation and tracking for large arrays in mm-wave picocells*, IEEE Journal of Selected Topics in Signal Processing **10** (April, 2016) 514–527.

[37] B. Mamandipoor, D. Ramasamy, and U. Madhow, *Frequency estimation for a mixture of sinusoids: A near-optimal sequential approach*, in *2015 IEEE Global Conference on Signal and Information Processing (GlobalSIP)*, pp. 205–209, Dec, 2015.

[38] W.-D. Wirth, *Radar techniques using array antennas*, .

[39] M. Steinhauer, H.-O. Ruob, H. Irion, and W. Menzel, *Millimeter-wave-radar sensor based on a transceiver array for automotive applications*, IEEE transactions on microwave theory and techniques **56** (2008), no. 2 261–269.

[40] R. E. Blahut, *Theory of Remote Image Formation*. Cambridge University Press, New York, NY, USA, 2004.

[41] M. Jankiraman, N. Willis, and H. Griffiths, *Design of multi-frequency CW radars*. SciTech Pub., 2007.

[42] N. Yamada, Y. Tanaka, and K. Nishikawa, *Radar cross section for pedestrian in 76ghz band*, in *Microwave Conference, 2005 European*, vol. 2, pp. 4–pp, IEEE, 2005.

[43] S. Basu *et. al.*, *A global lower bound on parameter estimation error with periodic distortion functions*, .

[44] H. L. Van Trees, *Detection, estimation, and modulation theory part iii*, .

[45] S. Basu and Y. Bresler, *A global lower bound on parameter estimation error with periodic distortion functions*, IEEE Transactions on Information Theory **46** (2000), no. 3 1145–1150.

[46] A. Gupta, U. Madhow, and A. Arbabian, *Super-resolution in position and velocity estimation for short-range mm-wave radar.*, in *ACSSC*, pp. 1144–1148, 2016.

[47] H. W. Kuhn, *The Hungarian method for the assignment problem*, Naval research logistics quarterly **2** (1955), no. 1-2 83–97.

[48] B. Wu and R. Nevatia, *Tracking of multiple, partially occluded humans based on static body part detection*, in *2006 IEEE Computer Society Conference on Computer Vision and Pattern Recognition (CVPR'06)*, vol. 1, pp. 951–958, 2006.

[49] L. Zhang, Y. Li, and R. Nevatia, *Global data association for multi-object tracking using network flows*, in *2008 IEEE Conference on Computer Vision and Pattern Recognition*, pp. 1–8, June, 2008.

[50] H. Jiang, S. Fels, and J. J. Little, *A linear programming approach for multiple object tracking*, in *2007 IEEE Conference on Computer Vision and Pattern Recognition*, pp. 1–8, June, 2007.

[51] H. Pirsiavash, D. Ramanan, and C. C. Fowlkes, *Globally-optimal greedy algorithms for tracking a variable number of objects*, in *CVPR 2011*, pp. 1201–1208, June, 2011.

[52] J. Berclaz, F. Fleuret, E. Turetken, and P. Fua, *Multiple object tracking using k-shortest paths optimization*, *IEEE Transactions on Pattern Analysis and Machine Intelligence* **33** (Sep., 2011) 1806–1819.

[53] Y. Bar-Shalom and X.-R. Li, *Multitarget-multisensor tracking: principles and techniques*, vol. 19. YBS, Storrs, CT, 1995.

[54] D. Reid, *An algorithm for tracking multiple targets*, *IEEE Transactions on Automatic Control* **24** (Dec., 1979) 843–854.

[55] K. G. Murty, *Letter to the editor—An algorithm for ranking all the assignments in order of increasing cost*, *Operations Research* **16** (1968), no. 3 682–687.

[56] F. Folster and H. Rohling, *Data association and tracking for automotive radar networks*, *IEEE Transactions on Intelligent Transportation Systems* **6** (2005), no. 4 370–377.

[57] S. Venkateswaran and U. Madhow, *Localizing multiple events using times of arrival: A parallelized, hierarchical approach to the association problem*, *IEEE Transactions on Signal Processing* **60** (2012), no. 10 5464–5477.

[58] M. A. Fischler and R. C. Bolles, *Random sample consensus: A paradigm for model fitting with applications to image analysis and automated cartography*, *Communications of the ACM* **24** (1981), no. 6 381–395.

[59] W. E. L. Grimson and T. Lozano-Perez, *Localizing overlapping parts by searching the interpretation tree*, *IEEE Transactions on Pattern Analysis and Machine Intelligence* (1987), no. 4 469–482.

[60] J. Neira and J. D. Tardós, *Data association in stochastic mapping using the joint compatibility test*, *IEEE Transactions on Robotics and Automation* **17** (2001), no. 6 890–897.

[61] T. Wagner, R. Feger, and A. Stelzer, *Wide-band range-doppler processing for FMCW systems*, in *2013 European Radar Conference*, pp. 160–163, Oct., 2013.

[62] B. Ristic, B.-N. Vo, D. Clark, and B.-T. Vo, *A metric for performance evaluation of multi-target tracking algorithms*, *IEEE Transactions on Signal Processing* **59** (2011), no. 7 3452–3457.

[63] L. Perron and V. Furnon, "Or-tools."

[64] B. Mamandipoor, G. Malysa, A. Arbabian, U. Madhow, and K. Noujeim, *60 ghz synthetic aperture radar for short-range imaging: Theory and experiments*, in *2014 48th Asilomar Conference on Signals, Systems and Computers*, pp. 553–558, Nov, 2014.

[65] B. Mamandipoor, M. Fallahpour, G. Malysa, K. Noujeim, A. Arbabian, and U. Madhow, *Spatial-domain technique to overcome grating lobes in sparse monostatic mm-wave imaging systems*, in *2015 IEEE MTT-S International Microwave Symposium, San Francisco, CA*, May, 2016.

[66] R. A. Horn and C. R. Johnson, *Matrix analysis*. Cambridge university press, 1990.